Soot Emission Prediction in RQL Type Aero Engine Combustor

MSc. Thesis Report

T. Eker

Technische Universiteit Delft

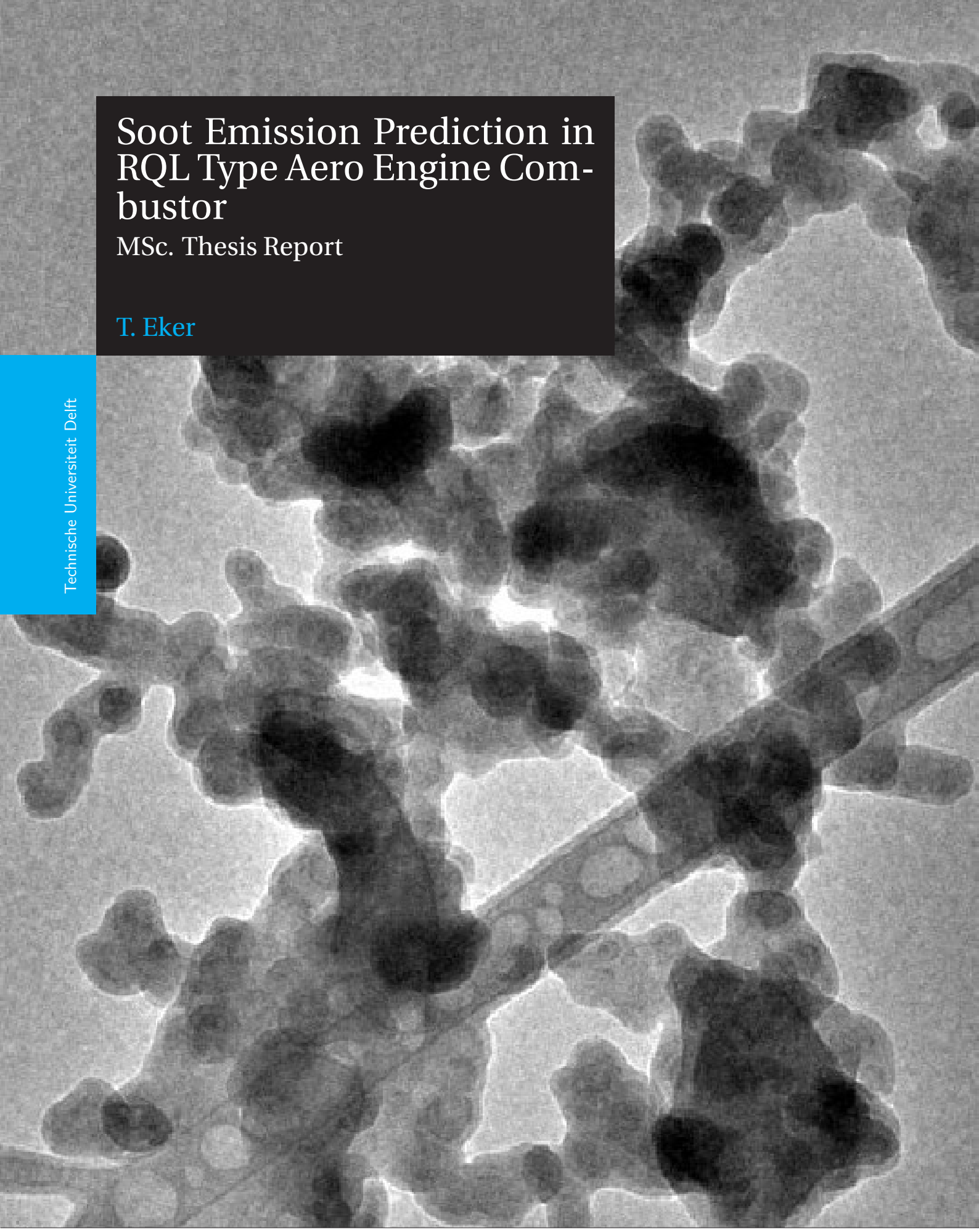

TU Delft Delft University of Technology

Challenge the future

SOOT EMISSION PREDICTION IN RQL TYPE AERO ENGINE COMBUSTOR

MSc. THESIS REPORT

by

T. Eker

in partial fulfillment of the requirements for the degree of

Master of Science
in Aerospace Engineering

at the Delft University of Technology,
to be defended publicly on Tuesday July 6, 2022 at 14:00.

Supervisor:	Prof. dr. A. G. Rao	
Thesis committee:	Dr. I. Langella,	TU Delft
	Dr. B. V. S. Jyoti,	TU Delft
	Dr. D. Lahaye,	TU Delft

This thesis is confidential and cannot be made public until July 6, 2025.

TU Delft Delft University of Technology

ACKNOWLEDGEMENT

The journey I have gone during this thesis was not what I expected, but it opened my eyes on things that I would have never thought I would experience. During this journey, there were few people that helped me to successfully complete this journey. I would like to show my gratitude towards them while I can here. Firstly I would like to thank to Dr. Arvind Gangoli Rao for his supervision on this thesis. Without his supervision and feedback on my work, it would have been impossible for me to complete this thesis. His guidance not only helped me to complete this work, it also expanded my vision and understanding of what it truly means to be an engineer.I would like to show my endless gratitude to my family. They always supported me on the journey that I was heading without any compromises. Their support, love and care made it possible for me to pursue this degree and completion of this thesis.

T. Eker
Delft, June 2022

ABSTRACT

The arising requirements for soot emissions from aircraft engines makes it pertinent to address the soot emissions in the earlier stages of the design process of the engine. One of the most effective and time efficient way to model emissions for an aero engine is to use chemical reactor networks which predict emissions. In the open literature, the examples of prediction of soot emissions for aircraft engines that use kerosene as fuel with chemical reactor networks are limited. To address this gap in the literature, this thesis will assess the modeling of soot emissions for an RQL combustion chamber by using chemical reactor network coupled with a detailed soot model.

Unlike other emissions limited for the aero engines such as NOx or CO, the soot formation process includes processes both in gas phase and aerosol dynamics. The chemical kinetics solver used can model gas phase kinetics but cannot model aerosol dynamics in the soot formation process. To include both gas phase mechanisms an aerosol dynamics present during soot formation, a detailed soot model, namely Method of Moments with Interpolative Closure is selected. A solver is developed to solve the equations of this soot model. This solver acts as post-processing to the reactor network results to calculate the soot emissions. In order to conduct this post-processing, the outputs of the reactor network simulation is fed into a solver and the soot emissions are calculated from the solution of these equations.

The developed modeling approach is first validated against jet stirred reactor and jet stirred reactor/plug flow reactor experiments. After the validation, the effect of pressure, temperature and equivalence ratio on soot formation is explored with the developed method. Lastly, this method is employed on predicting the soot emissions of a General Electric CF6-80C2 engine that houses a single annular Rich Burn-Quick Quench-Lean Burn combustion chamber to assess the viability of predicting soot emissions with the developed methodology.

CONTENTS

LIST OF FIGURES

LIST OF TABLES

NOMENCLATURE

Abbreviations

APEX	Aircraft Particle Emissions eXperiment
CFD	Computational Fluid Dynamics
CRN	Chemical Reactor Network
DQMOM	Direct Quadrature Method of Moments
DZ1	Dilution Zone 1
DZ2	Dilution Zone 2
EI	Emission Index
GSP	Gas Turbine Simulation Program
HACA	Hydrogen Abstraction Carbon Addition
ICAO	International Civil Aeronautics Organization
JSR	Jet Stirred Reactor
KM2	Kaust PAH Mechanism 2
MOM	Method of Moments
MOMIC	Method of Moments with Interpolative Closure
MZ	Mixing Zone
NASA	National Aeronautics and Space Administration
nvPM	Non-volatile Particulate Matter
PAH	Polycyclic Aromatic Hydrocarbon
PFR	Plug Flow Reactor
PSD	Particle Size Distribution
PSDF	Particle Size Distribution Function
PSR	Perfectly Stirred Reactor
PZ1	Primary Zone 1
PZ2	Primary Zone 2
QMOM	Quadrature Method of Moment
RQL	Rich-Burn Quick-Quench Lean-Burn
SZ	Secondary Zone
UHC	Unburnt Hydrocarbon

Symbols

α	Fraction of surface sites available for surface reactions	
β	Collision frequency	
$\dot{w}$	Net Creation rate	
η	Viscosity	kg/ms
μ	Normalized moment	
ρ_{soot}	Soot particle density	kg/m^3
τ	Residence time	s
C_v	Heat Capacity	J/K
C	Concentration	mol/m^3
C	Cunnigham Slip Coefficient	
d	Diameter	m
E_a	Activation Energy	kJ/mol
k_b	Boltzmann constant	$138 \times 10^{-23} m^2 kgs^{-2} K^-1$
k_s	per site rate reaction rate constant	m^2/s
m_c	Carbon atom mass	1201amu
MW	Molecular weight	kg/kJ
N_A	Avodagro's Constant	$6022 \times 10^{23} mol^-1$
N	Soot particle number density	$1/m^3$
P	Pressure	Pa
T	Temperature	K
v_x	Velocity	m/s
V	Volume	m^3
Y	Mass Fraction	
M	Moment	$1/m^3$

1

INTRODUCTION

The aviation sector is responsible of emitting gases such as carbon dioxide, nitrogen oxides, sulfur oxides and particulate matters to the atmosphere which have degrading effects on multiple platforms. Currently, aircraft emissions are responsible for approximately 4% of the emissions responsible for the total radiative forcing caused by human activities [19]. Aircraft manufacturers project that the amount of passengers that will use aircrafts for transportation will triple compared by 2030 compared to the aviation passengers of 2010 [20]. This increase in passengers will increase aviation's role in human induced radiative forcing in the upcoming years.

In order to address the current aviation activities and projected increase in aviation activities and their degrading effects via emissions, there is usually a complex mix of existing regulations and standards covering most of the emission sources that are present at airports. These sources range from aircraft engines to transport vehicle engines and aircraft maintenance facilities. Within this complex mix of regulations, the ones that are covering non-aircraft sources are generally established by the respective country and the emissions standards for aircraft engines are agreed internationally through the International Civil Aeronautics Organization (ICAO) and subsequently adopted into domestic regulations [21]. ICAO adopted its first standard named CAEP/1 in 1986, that applied to all in-production engines at the time. These standards are updated for more strict standards for aviation emissions every few years [21]. Until the release of CAEP/9 standards in 2013, the regulations were focused on emissions of nitrogen oxides(NOx), unburnt hydrocarbons(UHC) and carbon monoxide(CO) from aircraft engines. Up to CAEP/9 the soot emissions were regulated with smoke number(SN), which is a measure for visibility of the soot from aircraft engine exhaust. SN is useful to limit the visibility of the exhaust plume, but it is not quantifying physical, chemical, and optical properties of the engine exhaust regarding particulate matter emission[22]. Beginning with CAEP/10 in 2016, standards that limit concentration of nvPM emissions were also added to the standards to address the problems in local air quality in the vicinity of airports and other various effects of soot particles.

The focus on soot emissions in the context of aviation is important in order to minimize its effect on engine performance, health, atmospheric chemistry, local air quality and climate. The health effects of soot particles include premature mortality, aggravation of respiratory and cardiovascular diseases, changes in lung function, increased respiratory symptoms, changes to lung tissues and structure and altered respiratory defense mechanisms [21]. Soot particles emitted from aircraft engines affect local climates by disrupting the radiative balance of the atmosphere and changing the heating and cooling rate of the Earth. The soot particles emitted from aircraft engines contribute to the negative forcing at the lower sections of the atmosphere by absorbing the solar radiations in the visible spectrum and reducing the net shortwave solar radiation. At the upper parts of the atmosphere, soot particles promote positive forcing by affecting cloud condensation nuclear activation and increase the rate of cloud droplet formation [23].

With the arising requirements for particulate emissions from aircraft engines, the need to predict soot emissions during the conceptual design process of an aircraft engines becomes an important topic. If the requirements for the soot emissions are addressed through earlier stages of the design process, the increased cost in the later stages of the design phase to address the soot emissions can be avoided. To be effective during conceptual design, where many alternative designs are compared and the most suitable design is chosen, the emissions evaluation method must be parametric and fast while being accurate. The use of chemical reactor networks (CRN) either by itself or in conjunction with computational fluid dynamics analysis became a rec-

ognized method that can be used in preliminary design process. Especially, the simplicity and comparatively shorter computational time of the CRN method made them an option to predict emission from gas turbines and aero-engines.

1.1. KNOWLEDGE GAP

In the literature, there are examples of chemical reactor networks used to predict the emissions from the gas turbine combustion. One of the approaches is called parcel-box models where a CRN is constructed by representing the combustor and postcombustor flow with multiple reactors that assumes mass transfer with each other. The combustion parameters required for these reactors, such as temperature, turbulence, species concentrations, equivalence ratio, and gas residence time are calculated with computational fluid dynamics(CFD) calculations. Even tough this approach estimates quite accurate results for various emissions for gas turbines, this process is very time demanding and not the most suitable approach for a preliminary design process.

The other approach is the use of multiparcel zero dimensional (0-D) models, assuming that the combustor is composed of distinct sections such as primary zone, secondary zone and dilution zone. This apporach does not require any CFD simulation to initiate the models. The models constructed with this approach yield considerable agreement with experimental data for most major combustion-product concentrations and minor emissions such as NOx and CO. These models are more suitable for preliminary design process since they don't require an initial CFD simulation which is time demanding. Both of the mentioned approaches are used for modeling minor and major combustion products generated by gas-turbine combustors, but there are limited examples where soot emissions and their microphysics are modeled for gas turbines that use kerosene as fuel. This work will address this gap in the knowledge for an aero engine CRN model that uses kerosene as fuel and can predict soot emissions.

1.2. RESEARCH QUESTION AND RESEARCH OBJECTIVES

To address the knowledge gap found in the literature, the research question for this thesis is formulated as

How accurately can the soot emissions for an RQL type aero engine combustor predicted using chemical reactor networks in conjuction with a detailed soot model?

In order to address the research question, the objective of this thesis is to construct a chemical reactor network and couple it with a detailed soot model in order to predict soot emissions for a RQL type combustion chamber. To reach the research objective, a code that computes the soot emissions from the outputs of reactor networks is developed. This code uses Method of Moments with Interpolative Closure, a detailed soot model. The developed soot emission prediction method is validated against experiments conducted on jet stirred reactor/plug flow reactor for ethylene/oxygen/nitrogen combustion. After the validation, a parametric study is conducted to understand how soot formation is affected by the parameters studied, where the fuel studied is changed to kerosene. Lastly, a reactor network model for an aero-engine combustor is constructed and the soot emission model developed is applied to this model to predict the selected aircraft engine's soot emissions for various power settings.

1.3. THESIS LAYOUT

The layout of the thesis is presented in this section. Chapter 2 present the necessary literature for the thesis topic at hand. Chapter 3 describes the methodology and the tools used for constructing CRNs, the theory behind the soot model used in conjunction with the constructed CRNs and how the CRNs and the detailed soot model is coupled to estimate soot emissions. Chapter 4 shows the validation of the developed soot modeling approach according to experimental cases available in the literature. Chapter 5 presents the results of the parametric study conducted to assess the effects of varying combustion conditions on soot emissions. Chapter 6 presents the results for NOx, CO and soot emissions with the developed approach. Chapter 7 presents the conclusions drawn from the thesis study and recommendations for the modeling approach based on the modeling results from previous chapters.

2

BACKGROUND

Combustion is a phenomenon where chemically reacting flows with rapid and exothermic reactions occur. It is an interdisciplinary process that thermodynamics, chemical kinetics, fluid mechanics, and transport phenomena play fundamental roles [1]. In order to understand the behavior of various emissions from aero-engine combustors and develop a conceptual design tool focused on emissions, it is important to address the relevant background on physics, thermodynamics and chemical kinetics aspect of the combustion process. This section will present the background on combustion fundamentals that are relevant for emission modeling in combustion process.

2.1. COMBUSTION

2.1.1. FLAMES

Flames are reaction zones that occur during combustion process of non-homogeneous mixtures and they are sustained by transport phenomena. Depending on how reactants, fuel and oxidizer, are brought to the flame, flames can be distinguished as premixed and non-premixed flames [2]. According to the flow rate of the gases, these two flame types can be classified as laminar or turbulent. In general, flames can be classified as laminar premixed, laminar non-premixed, turbulent premixed or turbulent non-premixed flames. The transition from laminar to turbulent flame takes place as the flow velocity increases.

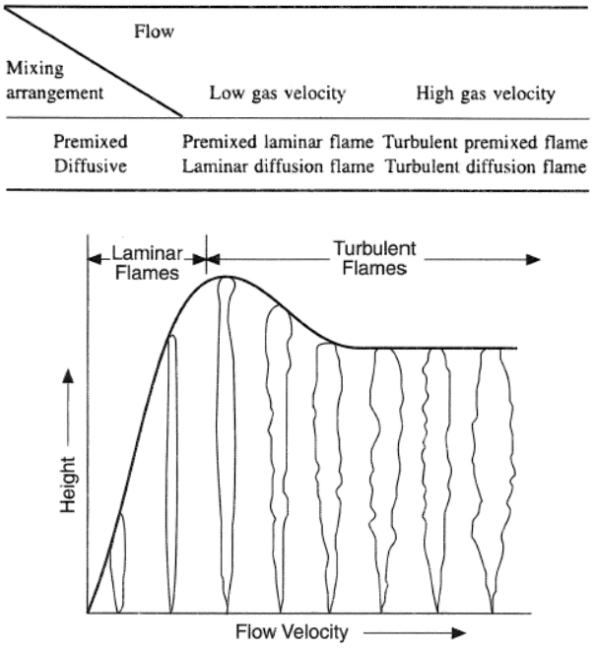

Figure 2.1: The main flame types according to mixing of the reactants and the velocity of the reactants [1]

A premixed flame occurs when the already mixed fuel and oxidizer react. The reaction in premixed flames is initiated when the chemical reaction of the fresh reactants is triggered through their preheating the hot products. This preheating starts a high-activation, exothermic chain reaction that continues until one of the reactants are consumed. The flame is followed by a post flame zone where the mixture slowly reaches equilibrium[2].

In non-premixed flames, the fuel and the oxidant meet at the burner mouth and mix by diffusion processes as the flame burns. In non-premixed flames, the combustion occurs when the reactants are preheated by the combustion products mix after injection [2]. There are two categories within non premixed flames, according to the initial physical state of the fuel and/or oxidant. If both the fuel and the oxidant are initially gaseous, then the flame is referred to as a diffusion flame. If both the fuel and oxidant are initially in different physical states, i.e., liquid and gas or solid and gas, although the system is still diffusion controlled, the process is usually called heterogeneous combustion [4]. The generic flame structure of premixed and non-premixed flame is shown in Figure 2.2.

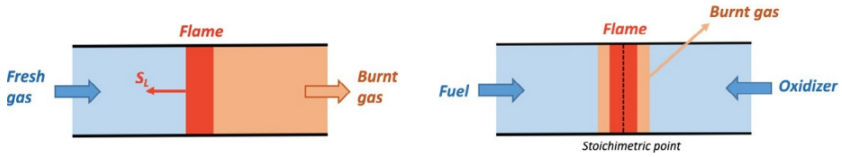

Figure 2.2: Generic Flame Structure of Premixed (Left) and Non-Premixed Flames (Right)[2]

As the flow speed of the reactants increase, the flame will eventually transition from laminar to turbulent regime. While laminar flames show a consistent and clear structure, turbulent flames may be wrinkled and be highly intermittent due to increased turbulence effects. The vortices generated due to turbulence will wrinkle the flame front and the flame surface area will increase. When the turbulence intensity is increased, the strong wrinkling will form pockets in flame front. As the intensity is increased further, flame may even detach from the main flame or a perfectly mixed regime may form. The turbulence-flame interaction will cause different flame regimes for premixed and non-premixed flames. The different flame regimes for premixed combustion is shown in Figure 2.3.

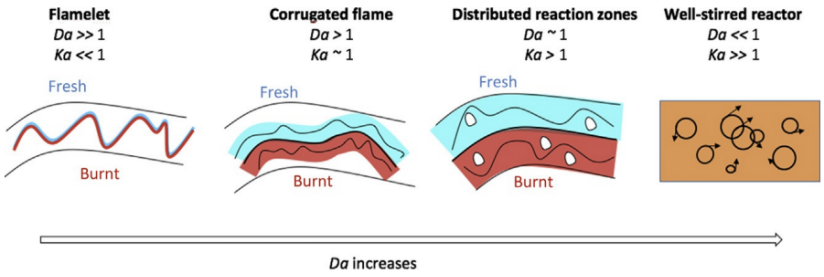

Figure 2.3: Types of turbulent premixed flames [2]

2.1.2. STOICHIOMETRY & EQUIVALENCE RATIO

For an aero-engine combustion, the global reaction equation for a hydrocarbon combustion can be expressed as:

$$C_m H_n + (m + \frac{n}{4})(O_2 + 3.7611 N_2) \rightarrow mCO_2 + \frac{n}{2} H_2O + 3.6711(m + \frac{n}{4}) N_2 \tag{2.1}$$

where the reactants consist of an aliphatic hydrocarbon as fuel and air as oxidizer. During stoichiometric combustion; the fuel and the air used during the combustion process consume each other completely, and all the carbon in the fuel converts to CO_2 and all the hydrogen in the fuel convert to H_2O [16, 24]. According to Equation 2.1, the stoichiometric ratio is $1/(m + \frac{n}{4})$. In practical combustion processes, stoichiometric combustion doesn't have to be reached and the fuel-air mixture may deviate from stoichiometric ratio. This deviation from stoichiometric mixture concentration can be expressed with air equivalence ratio λ or more

commonly by its reciprocal, fuel equivalence ratio $\phi = 1/\lambda$. The equivalence ratio can be expressed as:

$$\phi = \frac{x_{fuel}/x_{air}}{(x_{fuel}/x_{air})_{st}} = \frac{w_{fuel}/w_{air}}{(w_{fuel}/w_{air})_{st}} = \frac{\dot{m}_{fuel}/\dot{m}_{air}}{(\dot{m}_{fuel}/\dot{m}_{air})_{st}} \tag{2.2}$$

where x denotes the mole fraction, w denotes the mass fraction, $\dot{m}$ denotes mass flow rate, and subscript st denotes stoichiometric state. The equivalence ratio can tell the state of fuel-air mixture and this state can be divided into three groups [3],

$$\begin{aligned} \text{Fuel-Lean combustion:} \quad & \phi < 1 \\ \text{Stoichiometric combustion:} \quad & \phi = 1 \\ \text{Fuel-Rich Combustion:} \quad & \phi > 1 \end{aligned}$$

In fuel-lean or lean combustion, there will be excess of oxygen that is not used in the combustion process. In fuel-rich or rich combustion, there will be excess of fuel that is not used by the combustion process.

2.1.3. CHEMICAL EQUILIBRIUM AND GIBBS FUNCTION

In practical combustion processes, the global reaction will never reach completion but rather, the products will reach a state of chemical equilibrium. In most equilibrium cases, the products will mostly consist of complete reaction products accompanied by incomplete combustion products such as CO, H2, NOx and soot, which are inherent to the hydrocarbon combustion process. [16] In emission predictions, chemical equilibrium becomes important as it functions as an initial starting point and a limiting case for the chemical kinetics that determine the pollution formation during combustion process.

The chemical equilibrium lies between the compromise of enthalpy and entropy release during a process. This compromise can be formulated using Gibbs free energy, which is a measure of maximum work available for a system under constant temperature and pressure [25]. Gibbs free energy is formulated as,

$$G = H - TS \tag{2.3}$$

$$\Delta G = \Delta H - T\Delta S \tag{2.4}$$

The free energy change ΔG is an indicator of the spontaneity of a certain process. According to the arithmetic sign of free energy, the spontaneity of a process can be:

$$\begin{aligned} \text{Spontaneous reaction when} \quad & \Delta G < 0 \\ \text{Non-spontaneous reaction when} \quad & \Delta G > 0 \\ \text{Reversible reaction or in equilibrium when} \quad & \Delta G = 0 \end{aligned}$$

As stated, the chemical equilibrium or spontaneity of a reaction is based on the compromise between enthalpy and entropy. This compromise and the degree of spontaneity of a reaction can be seen for four different possibilities according to the sign of enthalpy and entropy change. These are: [25]

- When ΔH and ΔS are positive, the process is endothermic, and the entropy of the system increases. Under these conditions, ΔG will be negative if the magnitude of the $T\Delta S$ is bigger than ΔH meaning the process will be spontaneous and positive for vice-versa. These processes are spontaneous at high temperatures and non-spontaneous at low temperatures.
- When ΔH and ΔH are negative, the process is exothermic and system entropy decreases. In this case, ΔG will be negative if the magnitude of the $T\Delta S$ term is less than ΔH. If the $T\Delta S$ term's magnitude is greater than ΔH, the free energy change will be positive. Such a process is spontaneous at low temperatures and non-spontaneous at high temperatures.
- When ΔH is positive and ΔS is negative, the process is endothermic, and the system entropy decreases. In this case, ΔG will be positive for any temperature value. Such a process is non-spontaneous at all temperatures.
- When ΔH is negative and ΔS is positive, the system is exothermic, and the entropy of the system increases. In this case, ΔG will be negative for any temperature value. Such a process is spontaneous at all temperatures.

2.1.4. CHEMICAL KINETICS

GLOBAL AND ELEMENTARY REACTIONS

The overall process during a chemical reaction where the reactants are converted to products, like combustion of a hydrocarbon fuel, does not happen within a single step. For a reaction to happen in a single step, the necessary number of reactants should collide simultaneously and align themselves such that the products stated at the overall process can be produced in a single step. In molecular level, the possibility of such reaction is extremely low. During a chemical reaction, most of the time, large amount of intermediate reversible elementary reactions occurs to form the final products. The reaction scheme that is the culmination of these elementary reactions and shows the final products from the initial reactants are called global or overall reactions.

There are three types of reactions which can be counted as elementary reactions. The distinction for these elementary reactions is made in terms of molecularity, or the number of species involved during the reaction [26]. The types of elementary reactions are:

- Unimolecular reactions involve a single reactant that rearranges or dissociates themselves to form the products. They can be represented as:

$$\text{A} \rightarrow \text{products}$$

- Bimolecular reactions involve two reactants to form the products. They can be represented as:

$$\text{A+A} \rightarrow \text{products}$$
$$\text{A+B} \rightarrow \text{products}$$

- Trimolecular reactions involve three reactants to form the products. They can be represented as:

$$\text{A+A+A} \rightarrow \text{products}$$
$$\text{A+A+B} \rightarrow \text{products}$$
$$\text{A+B+C} \rightarrow \text{products}$$

REACTION RATE

The reaction rate defines the rate of formation or consumption of species involved in a chemical reaction. A general forward chemical reaction can be represented as [26]:

$$\sum_{i=1}^{N} \nu_i' \mathbf{M}_i \xrightarrow{k_f} \sum_{i=1}^{N} \nu_i'' \mathbf{M}_i \tag{2.5}$$

where i is the index for a species in the chemical reaction, k_f is the reaction rate constant with subscript f stating the forward direction, ν_i' and ν_i'' are coefficients of reactants and products respectively, and M_i is a species in the reaction. The rate of change in molar concentration($\hat{\omega}_i$) for a species i is

$$\hat{\omega}_i = \frac{dc_i}{dt} \tag{2.6}$$

where (c_i) is the molar concentration of species i. The rate of change of molar concentration for a species (moles per unit volume times second) can be used to express the overall reaction rate ω

$$\omega = \frac{\hat{\omega}_i}{\nu_i'' - \nu_i'} = \frac{\hat{\omega}_j}{\nu_j'' - \nu_j'} \tag{2.7}$$

The reaction rate ω has units of moles per unit volume per second and hence, it is an intensive property. The law of mass action states that reaction rate is proportional to the product of the concentrations of the reactants. For the reaction set at Equation 2.5, reaction rate is

$$\omega = k_f(T) \prod_{i=1}^{N} c_i^{\nu_i'} \tag{2.8}$$

where $k_f(T)$ is the specific reaction rate constant and is primarily a function of temperature [26]. Every forward reaction has its corresponding backward reaction. For reactions at Equation 2.5, the backward reaction is

$$\sum_{i=1}^{N} \nu_i'' \mathbf{M}_i \xrightarrow{k_b} \sum_{i=1}^{N} \nu_i' \mathbf{M}_i \tag{2.9}$$

If the forward and backward reaction rates are known, the net reaction rate, where both forward and backward reaction rate occurs, can be found. The overall reaction rate can be stated as

$$\omega = k_f \prod_{i=1}^{N} c_i^{\nu_i'} - k_b \prod_{i=1}^{N} c_i^{\nu_i''} \tag{2.10}$$

At chemical equilibrium, the forward and backward reaction rates are the same which yields no net reaction ($\omega \approxeq 0$). In chemical equilibrium, the rate of forward reaction is balanced by that of backward reaction, and the equality can be stated:

$$\omega = k_f \prod_{i=1}^{N} c_i^{\nu_i'} = k_b \prod_{i=1}^{N} c_i^{\nu_i'} \tag{2.11}$$

Or if the equality is rearranged, the ratio of forward and backward reaction rate constant is equilibrium constant Kc

$$K_c = \frac{k_f}{k_b} = \prod_{i=1}^{N} c_i^{(\nu_i'' - \nu_i')} \tag{2.12}$$

RATE LAW & REACTION ORDER

In chemical reactions, the reaction rate can be mathematically formulated using rate law. Rate law formulates the reaction rate by using concentration of the reactants and their corresponding reaction rate constant for either forward or reverse direction. For an arbitrary chemical equation

$$\mathrm{aA} + \mathrm{bB} + \mathrm{cC} + \ldots \quad \xrightarrow{k} \quad \mathrm{dD} + \mathrm{eE} + \mathrm{fF} + \ldots \tag{2.13}$$

the reaction rate can be expressed as rate of consumption of a specific species. For example, looking at the consumption of species A, the reaction rate (RR) can be expressed as

$$\frac{\mathrm{d[A]}}{\mathrm{d}t} = -k \cdot [\mathrm{A}]^a [\mathrm{B}]^b [\mathrm{C}]^c \tag{2.14}$$

where a, b, c, are reaction orders with respect to the species A, B, C are the species concentration and k is the reaction rate constant at the direction of consumption of species A. The sum of all exponents is the overall reaction order[4].

The change of the concentration of species A in time can be calculated by integrating the rate equation. There are some typical cases for these integrations according to the overall reaction order. The first case is the first order reactions where the overall reaction order is equal to 1. For a first order reaction with rate equation

$$\frac{\mathrm{d[A]}}{\mathrm{d}t} = -k \cdot [\mathrm{A}] \tag{2.15}$$

The integration of the rate equation yields

$$\ln \frac{[A]_t}{[A]_0} = -k \cdot [\mathrm{A}] \tag{2.16}$$

where $[A]_0$ and $[A]_t$ denotes the concentrations of species A at time t_0 and t, respectively.

The other case is the second order reaction where the overall reaction order is 2. For a second order reaction with rate equation

$$\frac{\mathrm{d[A]}}{\mathrm{d}t} = -k \cdot [\mathrm{A}]^2 \tag{2.17}$$

The integration of the rate equation yields

$$\frac{1}{[\mathrm{A}]_t} - \frac{1}{[\mathrm{A}]_0} = k\,(t - t_0) \tag{2.18}$$

The last case is a third order reaction. For third order reaction with rate equation

$$\frac{\mathrm{d[A]}}{\mathrm{d}t} = -k \cdot [\mathrm{A}]^3 \tag{2.19}$$

The integration of third order reaction rate yields the temporal behavior yields

$$\frac{1}{[\mathrm{A}]_t^2} - \frac{1}{[\mathrm{A}]_0^2} = 2k(t - t_0) \tag{2.20}$$

TEMPERATURE DEPENDENCE OF REACTION RATE

The reaction rate coefficient of most reactions depends strongly on the temperature in a nonlinear fashion. According to the Arrhenius law, the dependence of reaction rate constant on temperature can be formulated as

$$k = A \exp\left(-\frac{E_a}{R_u T}\right) \tag{2.21}$$

where A is the pre-exponential factor or frequency factor r and has units of $1/\mathrm{s}$, $\mathrm{cm}^3/(\mathrm{mol}\cdot\mathrm{s})$, and $\mathrm{cm}^6/(\mathrm{mol}^2\cdot\mathrm{s})$ for unimolecular, bimolecular and termolecular reactions respectively. E_a (kJ/mol) is the activation energy that represents the energy of the colliding molecules must have to make the reaction possible. R_u(J/(K·mol)) is the universal gas constant and, T is temperature. The temperature dependence of rate coefficient is shown in Figure 2.4.

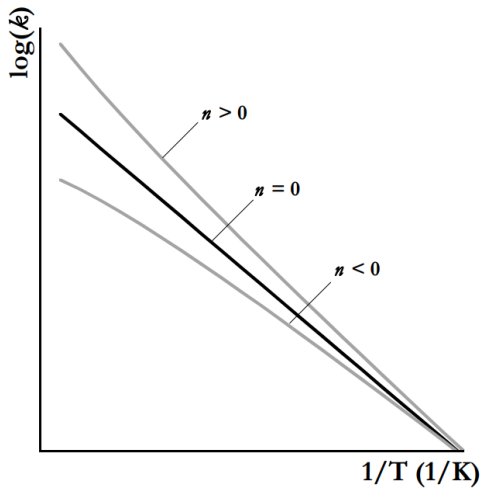

Figure 2.4: The temperature dependence of rate coefficient [3]

For many elementary reactions, the pre-factor A is found to be not a constant, but rather temperature dependent. According to the temperature dependency of the pre-exponential, the Arrhenius equation is introduced to account for this dependency,

$$k = BT^n \exp\left(-\frac{E_a}{R_u T}\right) \tag{2.22}$$

where B is a constant and n is the temperature exponent[3].

CHAIN AND CHAIN-BRANCHING REACTIONS

Radical chain reactions play a major role during the combustion process, including pollutant formation during combustion process. In chain reactions, radical species are formed which react to form other radicals and newly formed radicals react to further form other radicals. Due to their high reactivity, the sequence of this radical production or chain reaction, continues until a stable species are formed from radical species. Chain reactions involve four main steps[26]:

- Chain initiation step: Radicals that will start the chain reaction sequence are formed from stable species.

- Chain propagation steps: The formed radicals react with stable species to form other radical species. These steps are important as they influence the rate of overall chain reaction set the most.
- Chain branching steps: The radical species react with stable species to form two reactive species. These are special kinds of chain propagation steps, as they lead to explosion
- Chain termination steps: The radical species will react to form stable species. Termination can also occur when a radical reacts with a molecule to give either a molecular species or a radical of lower activity that cannot propagate a chain.

2.2. REACTION MECHANISMS

Reaction mechanisms describe the conversion of a certain reactant combinations to final products with collection of elementary reactions. In the context of combustion, reaction mechanisms include all the chemical species and the elementary reactions that are effective during the combustion process. Reaction mechanism do not include every single species and their corresponding reactions because some of the species may not participate during a specific combustion process or the reaction rate of the species may be really small compared to other species[27].

During the combustion of hydrocarbon fuels, the fuel molecules are sequentially fragmented into smaller intermediate species that are ultimately converted into the final combustion products, that is mostly CO_2 and H_2O. These intermediate species may be fuels that include smaller number of carbon atoms inside their molecules. Because of this trend, a reaction mechanism is built systematically, starting from simplest species and reactions that play role in more complex species. Addition of more complex species and their corresponding reactions on top of the initial species and their corresponding reactions proceed until the chemical reaction behavior of the desired reactants can be represented with the reaction mechanism. The added portions of reaction sets are validated through comparison between numerically predicted and experimental results [27].

During the validation of each level of reaction mechanism, multiple experiments will be used to validate the step of a certain mechanism. Different elementary reactions will be dominant in different combustion or experimental conditions. For example, for most of the hydrocarbon systems, reactions between fuel molecules and H atoms are dominant in fuel-rich conditions but much less important in fuel-lean conditions where reactions between fuel and O or OH radicals are most important. If a reaction mechanism can represent the combustion of a fuel for a wide range of conditions, the reaction mechanism will be called comprehensive reaction mechanism [27].

Kerosene used in aero engines is a mixture of many hydrocarbons such as alkanes, cycloalkanes, aromatics compounds. The average chemical formula of kerosene changes from source to source. The chemical formula that represent the kerosene can range from $C_{10.9}H_{20.9}$ to $C_{11}H_{23}$. To represents the combustion behavior of kerosene, mixtures with well-defined composition called surrogate fuels are used in the literature. These surrogate fuels include a small number of hydrocarbons to be as simple as possible. Surrogate fuels can be classified as; physical surrogate fuels that have the same physical properties as the real fuel, chemical surrogate fuels that have the same chemical properties as the real fuel, or comprehensive surrogate fuels that have both the physical and chemical properties of the real fuel. One of the main applications of these surrogate fuels are to formulate kerosene reaction mechanisms that can be used to model different combustion conditions. Some of the kerosene surrogates available in the literature are listed in Table 2.1

Table 2.1: Kerosene surrogates

Year	Name	Species Included	Reactions Included	Surrogate Species	Average Chemical Formula
2002	Dagaut[28] Surrogate	209	1673	n-Decane 0.74 n-PropylBenzene 0.15 PropylCyclohexane 0.11	$C_{9.74}H_{20.06}$
2009	Aachen[29] Surrogate	119	527	n-Decane 0.777 n-PropylBenzene 0.223	$C_{9.78}H_{19.78}$
2010	Jetsurf[30] mechanism	343	2343	n-Decane 0.47 Methyl-Cyclohexane 0.24 Toluene 0.29	$C_{8.4}H_{16}$
2010	Slavinskaya [31]	179	1180	10% propylcyclohexane 13% - iso-octane 20% - dodecane 25% - methylnaphtalene 32% - C16H34 hexadecane	c12.21H22.72
2013	2nd Gen Surrogate Illinois [32]	2080	8310	n-DoDecane 0.4 Iso-Octane 0.3 n-PropylBenzene 0.228 1,3,5 TriMethylBenzene 0.072	$C_{9.9}H_{19.4}$
2018	HYCHEM surrogate[33] [34]	201	1589	$C_{11}H_{22}$	$C_{11}H_{22}$

2.3. POLLUTANT FORMATION MECHANISMS

2.3.1. NITRIC OXIDES (NOX)

NOx is one of the main products of hydrocarbon combustion due to one of the reactants being air or nitrogen bound to the fuel molecules. Minimization of NOx emissions became one of the main research topics due to its effects on the environment. It is one of the main contributors of photochemical fog and ozone in the troposphere, and one of the participants of ozone removal at stratosphere level [16]. The term NOx is describing both NO and NO2 because NO formed during combustion process will eventually oxidize to form NO2 [4]. There are several mechanisms in which NOx can be formed during hydrocarbon combustion that are discussed below.

THERMAL NOX (ZELDOVICH)

In the absence of fuel bound nitrogen, thermal pathway for NOx formation is one of the main sources of NOx in many combustion devices where flame temperature is above 1800K [35]. This mechanism is also called Zeldovich mechanism after Y.B. Zeldovich, who postulated this mechanism in 1946. In this reaction, NO is produced when the molecular oxygen dissociates under high temperatures and reacts with molecular nitrogen. This reaction is followed by molecular oxygen reacting with the N atoms. Also, the OH radicals can react with N atoms to form NO. The thermal NOx mechanism proposed is

$$O_2 \longleftrightarrow 2O \tag{2.23a}$$

$$N_2 + O \longleftrightarrow NO + N \tag{2.23b}$$

$$N + O_2 \longleftrightarrow NO + O \tag{2.23c}$$

$$N + OH \longleftrightarrow NO + H \tag{2.23d}$$

Reaction 2.23a has high activation energy that comes from the strong triple bond in the N_2 molecules. This reaction is sufficiently fast only at high temperatures. Due to its small reaction rate and temperature dependence, Reaction 2.23a is the rate limiting reaction of this reaction set and the reason this mechanism is called thermal.[26] The temperature dependence of the thermal pathway is shown in Figure 2.5, where the reaction rate increases as the temperature increases. The NO formation in this pathway peaks at fuel lean conditions due to the limited availability of oxygen that reacts with the fuel and the nitrogen.

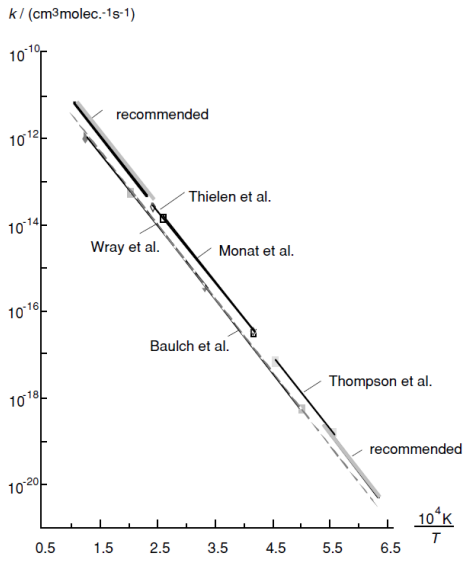

Figure 2.5: Temperature dependence of thermal pathway reaction rate constant of NO formation [4]

PROMPT NOX (FENIMORE)

This mechanism was postulate by C.P. Fenimore in 1979. Fenimore proposed prompt-NO formation pathway to explain the nitric oxide found in the thin reaction zone close to the burner surface in experimental data obtained from CH4, C2H4, and C3H8 flames where the NO concentration should reach to zero at the downstream of the flame according to Zeldovich mechanism [26][35]. The additional mechanism that is promptly producing NO at the flame front is more complicated than thermal NO.[16] The primary route for the prompt NOx formation involves the reaction between N2 and hydrocarbon radicals, predominantly CH, to form NCN and H as:

$$N_2 + CH \longleftrightarrow NCN + H2 \tag{2.24}$$

Subsequently, NCN will undergo fast oxidation with O and OH radical species to form NO via reactions:

$$NCN + OH \longleftrightarrow NO + HCN \tag{2.25}$$

$$NCN + O \longleftrightarrow NO + CN \tag{2.26}$$

In addition, NCN can further react with H to form N and HCN species that can lead to NO formation.

$$NCN + H \longleftrightarrow HCN + N \tag{2.27}$$

$$N_2 + C \longleftrightarrow CN + N \tag{2.28}$$

The nitrogen atoms produced with the last two reactions can react with O2 and OH to enhance thermal-NO formation given in Reaction 2.23c and Reaction 2.23d, while the cyano-compounds react with various oxygen-containing species to form NO.[35] Prompt NO formation is higher at fuel rich flames compared to lean conditions because the CH radical precursor C2H2 is prevalent at fuel rich conditions due to the CH3 recombination [26] that can be seen from Figure 2.6.

Prompt NO does not generally form in any significant quantity in the post-flame zone because the concentration of hydrocarbon radicals is quite small away from the flame front. The formation of prompt NO in the flame zone increases under fuel-rich conditions because of the availability of larger quantities of hydrocarbon radicals [35].

2.3.2. CARBON MONOXIDE

In hydrocarbon combustion, during lean conditions, CO will form due to the dissociation of the CO_2. For fuel rich conditions, CO is mainly formed due to the incomplete combustion where there is insufficient oxygen to complete the reaction to form CO_2. The incomplete combustion may occur due to insufficient burning rates on the primary zone, insufficient mixing of fuel and air, and quenching of post-flame products in the primary zone by liner cooling [4].

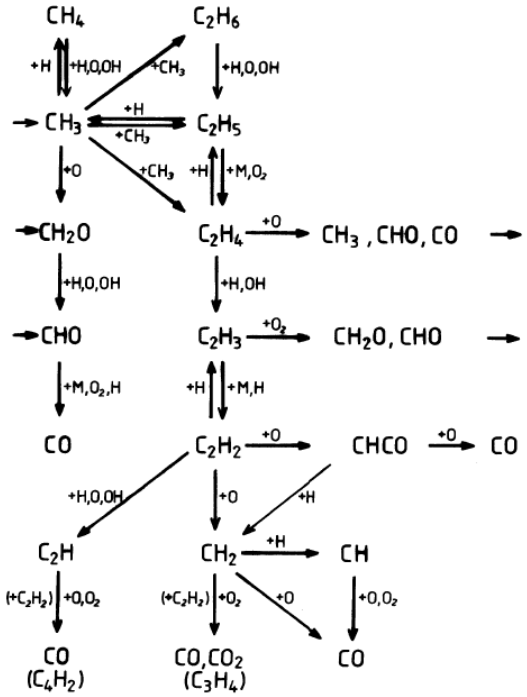

Figure 2.6: CO formation pathways [4]

Hydrocarbon fuel oxidation in a gas turbine can be under three main reaction pathways, which are low, intermediate, and high temperature oxidation regimes. These pathways are separated according to temperature ranges present during oxidation of the fuel happens. Under typical gas turbine operating conditions, oxidation regimes occur above 1200K which is considered to fall under high temperature oxidation regimes. Since most gas turbine operating conditions accommodate for such temperatures during oxidation, reaction pathways for chain branching during high temperature oxidation is considered during gas turbine combustion [35]. During the high temperature oxidation of a higher-order hydrocarbon fuel, alkyl radicals are formed. The alkyl radicals undergo chain reactions with other combustion radicals to form smaller hydrocarbon molecules such as CH_3, C_2H_4, and C_2H_5 that will further react with oxygenated combustion species (O_2, O, OH, and HO_2 to form formaldehyde (CH_2O). The thermal and chemical decomposition of CH_2O will result in formation of HCO and CO [35]:

$$CH_2O + M \longleftrightarrow HCO + H + M \tag{2.29}$$

$$CH_2O + M \longleftrightarrow CO + H_2 + M \tag{2.30}$$

Where M is a third-body collisional species. Apart from this, CH2O will also react with H, O, OH, and HO2 to form HCO [35]:

$$CH_2O + H \longleftrightarrow HCO + H_2 \tag{2.31}$$

$$CH_2O + O \longleftrightarrow HCO + OH \tag{2.32}$$

$$CH_2O + OH \longleftrightarrow HCO + H_2O \tag{2.33}$$

$$CH_2O + HO_2 \longleftrightarrow HCO + H_2O_2 \tag{2.34}$$

The HCO formed will further react to form CO with the following reactions [35]:

$$HCO + O \longleftrightarrow CO + HO_2 \tag{2.35}$$

$$HCO + M \longleftrightarrow H + CO + M \tag{2.36}$$

The CO formed is resistant to oxidation. At high temperatures, CO can be removed via the following reaction to form CO_2 [35]:

$$CO + OH \longleftrightarrow CO_2 + H \tag{2.37}$$

At lower temperatures, the main removing reaction to form CO2 is [35]:

$$CO + H_2O \longleftrightarrow CO_2 + H_2 \tag{2.38}$$

2.4. SOOT

Soot forms as an outcome of local or global fuel rich combustion. During the combustion of liquid or solid hydrocarbon fuels, local regions of fuel rich combustion may exist. In conventional combustors, local fuel rich regions occur near the fuel spray. In these regions, burned products recirculate downstream to the fuel spray region, where local pockets of fuel vapor become enveloped in oxygen-deficient gases at high temperature. The soot formed near the fuel spray at primary zone is mostly consumed at high temperature regions at the downstream. The overall soot formation during a combustion process can be expressed as the difference in soot formation rate in primary zone and soot consumption rate in rest of the combustion chamber [30].

The chemical composition of soot is not uniquely defined. The atomic C/H ratio of soot particles ranges from 8 to 12. The average mass density of soot differentiates between 1.8 and 2 g/cm^3. Soot is mostly made of carbon and up to 10% of hydrogen in terms of moles. When hydrogen is extracted from the soot particles via organic solvents, condensed polycyclic aromatic hydrocarbons (PAHs) are found. Under high resolution electron microscopes, soot particles are observed to be fractal-like aggregates. The dimension of these fractal-like aggregates is usually around 1μm. These aggregates consist of hundreds of nearly spherical particles. The diameter of the nearly spherical particles, called primary particles, are usually in the range of 20 to 50 nm and contain between 105 to 106 carbon atoms. X-ray diffraction shows that the primary soot particles are made up of many randomly arranged grains. Each grain consists of 5 to 10 nearly parallel planes arranged in a turbostratic fashion. Each layer is between 1nm to 2 nm in dimension and contains on the order of 50 carbon atoms. The inner layer spacing is about 0.35 nm, which is of the same order as that of graphite [26].

Soot is not an equilibrium product of combustion. It only becomes an equilibrium product for mixture strengths much richer than the fuel-air mixtures utilized in primary zone of conventional gas turbines. Therefore, it is not possible to predict the formation rate or final concentration of soot just from thermodynamic data. This means that soot formation is also a chemical kinetic problem and it requires a consideration of the underlying reaction mechanism. From the research done to understand and model the reaction mechanism of soot, it is possible to simulate soot formation and consumption with empirical, semi-empirical and detailed chemistry models.[4]

2.4.1. SOOT FORMATION MECHANISM

Based on the studies done to understand soot formation, the steps of soot formation are generally particle nucleation/inception, surface growth by reaction with gas-phase molecules; coagulation of particles through particle-particle sticking collisions; mass removal from particles by pyrolytic processes leading to dehydrogenation and structural rearrangement of the condensed material; and oxidation of soot particles. The steps of soot formation process for a conventional gas turbine combustor is shown in Figure 2.7.

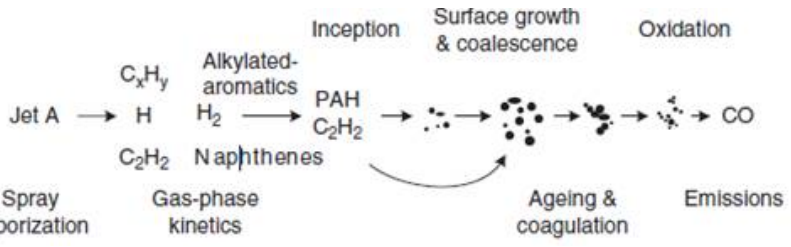

[26]

Figure 2.7: Steps of soot formation during fuel spray combustion

SOOT INCEPTION

The soot inception starts with formation of Polycyclic Aromatic Hydrocarbons (PAH) from singular aromatic ring. The PAH formation starts with polymerization of PAH molecules by the reaction of non-aromatic species. The PAH formation starts with vinyl addition to acetylene. After this addition, the reaction will follow either the high temperature or the low temperature route. At high temperatures, the addition will form vinyl acetylene followed by acetylene addition to n-C4H3 radical that will form phenyl. With hydrogen addition to phenyl, benzene will be formed. At low temperatures, the addition of vinyl to acetylene will form n-C4H5.

The addition of acetylene to n-C4H5 will result in the formation of benzene. The benzene and phenyl formed during this sequence is called first aromatic ring [5].

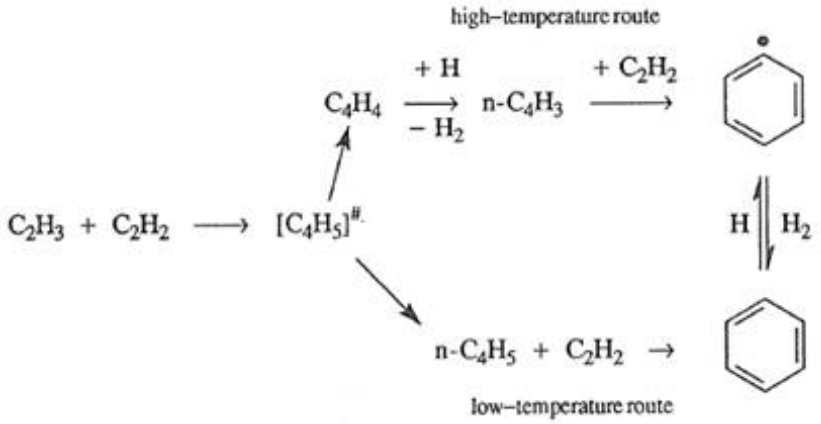

Figure 2.8: Thermal pathway for the formation of first aromatic ring [5]

After the first aromatic ring is formed, the growth of PAH will be promoted with a sequential two-step process: hydrogen abstraction and acetylene addition, or HACA mechanism in short. The addition of hydrogen activates the aromatic molecules and acetylene addition will propagate molecular growth and cyclization of PAH [5]. HACA mechanism also plays a major role in surface growth, which will be explained later. The general sequence for HACA formation is

$$R-H+H\bullet \rightarrow R\bullet + H_2 \tag{2.39a}$$

$$R\bullet + H\bullet \rightarrow R-H \tag{2.39b}$$

$$R\bullet + C_2H_2 \rightarrow R'-H+H\bullet \text{ or } R'\bullet \tag{2.39c}$$

During soot particle inception, the addition of acetylene to an aromatic radical species, like phenyl, makes them more reactive, which leads them to either the bond with an ethynyl (-C2H) group with the aromatic ring, or the formation of an additional condensed aromatic ring. Depending on the neighboring ring structure, the newly formed ring can either be a radical, which can grow readily with acetylene, or it may be a molecular species. The latter will have to be activated through the H-abstraction reaction to produce a PAH radical species, before it can undergo the further growth reaction with acetylene.[3] [5]

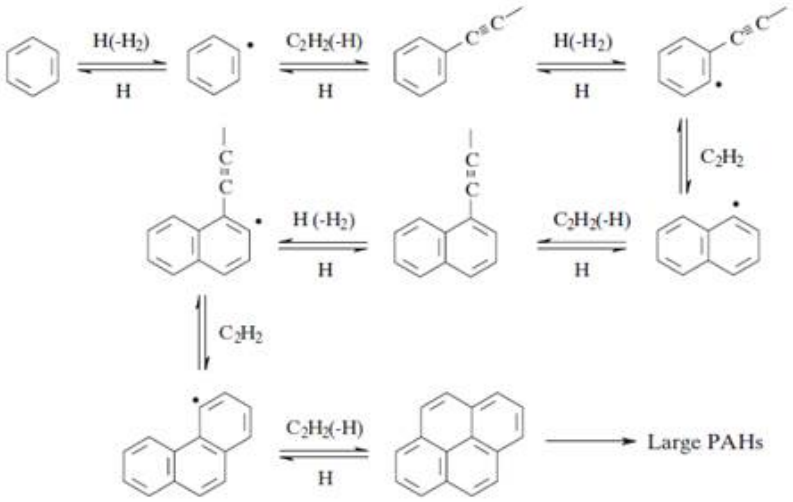

Figure 2.9: PAH growth from first aromatic ring with HACA mechanism [6]

If the concentrations of aromatic species are sufficiently large, PAH growth through direct ring-ring condensation is also possible. For example, benzene and phenyl can react to form biphenyl. Through the H-abstraction reaction, a biphenyl radical forms and can react with acetylene to form the three-ring phenanthrene, or it can react with benzene to form a four ring aromatic species [4][36]. Such a reaction sequence is shown in Figure 2.10.

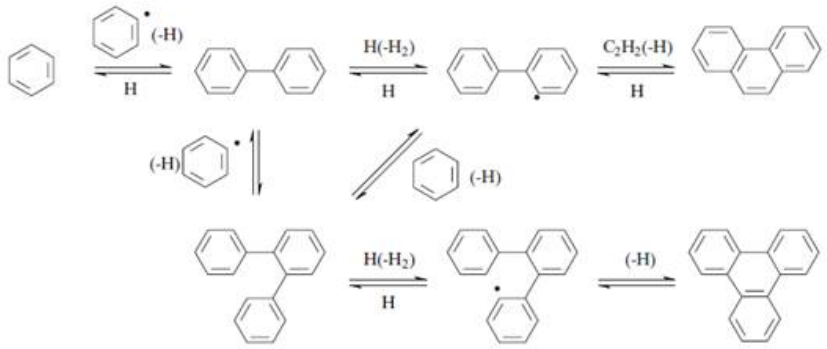

Figure 2.10: PAH growth with direct ring condensation [6]

The competition between the HACA mechanism and the aromatic ring condensation mechanism is largely determined by the ratio of acetylene to benzene. If the concentration of acetylene is substantially larger than benzene's, the HACA mechanism dominates. However, if the acetylene concentration is about equal to benzene's, such as in the very early stage of a premixed benzene flame, then the direct ring condensation mechanism may dominate. When PAHs grow to the size of pyrene (a four ringed PAH) or larger, they may be able to condense onto each other upon collision and form small clusters.

SOOT MASS/SURFACE GROWTH

When PAH molecules reach a certain size, they start to coalesce into each other, forming PAH clusters. The exact mechanism of the coalescence process is still unclear. Nonetheless, experimental studies show that the process is rather rapid, to an extent that a direct measurement for particle inception is almost impossible. The clusters then grow by coagulating into each other, leading to particles that are a few nanometers in diameter. These processes may be physically depicted by the following sequence of reaction like steps[3]:

$$A1 + A1 \rightarrow B2$$
$$A1 + B2 \rightarrow B3$$
$$\cdots\cdots$$
$$A1 + Bn \rightarrow Bn + 1$$

Here A1 denotes a PAH molecule, B2 is a dimer of PAH molecules, B3 is a trimer of PAH molecules, and Bn is a polymer which contains n number PAH molecules. Overall, these processes require the sticking of PAHs and forming clusters upon collision. Most of the soot mass, however, is acquired through gas-surface reactions. Like in PAH growth, the HACA mechanism is responsible of soot surface growth through gas-surface reactions. This surface reaction mechanism is often written as [3].

$$\mathrm{Si-H + H\bullet \rightarrow Si\bullet + H_2} \tag{2.40a}$$
$$\mathrm{Si\bullet + H\bullet \rightarrow Si-H} \tag{2.40b}$$
$$\mathrm{Si\bullet + C_2H_2 \rightarrow S_{i+2-H} + H\bullet} \tag{2.40c}$$

Where S_i represents the soot particle,with size i, specifically the site on soot particle surface where the reaction takes place. There are reaction sets proposed to represent the surface reactions happening on soot particles. One of the surface reaction model was proposed by [37] and shown in Table 2.2. An alternative model was proposed by Colket and Hall [18], where the model treated the oxidation reactions happening on the surface with separate terms, and shown in Table 2.3.

Along with the HACA mechanism, the contribution of the PAH condensation on the soot mass as a surface reaction mechanism during soot formation is started to be recognized. Some of the studies that included PAH condensation to the surface reactions were Benish et al.[38], Blanquart et al. [39], and Mauss et al.[40].

Table 2.2: Surface reactions rates proposed by Frenklach and Wang[17]

No	Reaction
1	$C_{soot} - H + H \longleftrightarrow C_{soot} \cdot + H_2$
2	$C_{soot} - H + OH \longleftrightarrow C_{soot} \cdot + H_2$
3	$C_{soot} \cdot + H \rightarrow C_{soot} - H$
4	$C_{soot} \cdot + C_2H_2 \rightarrow C_{soot} - H + H$
5	$C_{soot} \cdot + O_2 \rightarrow 2CO + \text{products}$
6	$C_{soot} - H + OH \rightarrow CO + \text{products}$

Table 2.3: Surface reactions rates proposed by Colket and Hall[18]

No	Reaction
1	$C_{soot} - H + H \longleftrightarrow C_{soot} \cdot + H_2$
2	$C_{soot} \cdot + H \rightarrow C_{soot} - H$
3	$C_{soot} \cdot \rightarrow \text{products} + C_2H_2$
3	$C_2H_2 + C_{soot} \cdot \rightarrow C(s)CHC'H$
4	$C_{soot} - C(s)CHC'H \rightarrow C_{soot} \cdot + H$

SOOT COAGULATION

Coagulation takes place for relatively small particles. The diameter of the particle may reach up to 10nm with coagulation. Coagulation of soot particles are basically sticking of two particles to each other. During this sticking, a common outer shell forms from depositions linked to the surface growth. The rate of the coagulation can be calculated with relative ease. During the calculations for soot coagulation rate, few characteristic conditions are assumed:

- The soot particles are small in comparison to the gas mean free path
- Each collision of two particles results in coagulation
- All particles are spherical

The first assumption is valid for small particles or low densities such that the particle diameter is much less than the mean free path. This is satisfied in low pressure flames for the entire coagulation process, but can fail at high pressures. The second and third assumptions seem to be well justified for coagulation of soot particles. Based on these assumptions, rate expressions for soot coagulation can be found in literature [41].

SOOT OXIDATION

The soot particles formed can be oxidized by OH radicals, O atoms or O2 molecules. In the majority of the combustion conditions, soot oxidation happens mostly with OH radicals because O atom concentration is usually less than OH radical concentration in flames. Under lean combustion at lower temperatures, the soot particles will oxidize with O2 molecules as radical species are greatly reduced under these combustion conditions [26]. During oxidation of soot particles, the characteristic size of the soot particles is assumed as primary particle size even for agglomerated particles. The agglomerated soot particles are made up of open structures which allow the diffusion of oxidization agents that will oxidize and primary soot particles that make up the agglomerated particles. The oxidation rate of soot particles is kinetically controlled under most combustion conditions [26]. OH and O concentrations in flames are determined by detailed chemical kinetics and cannot be accurately predicted from simple equilibrium at the local temperature and stoichiometry. Therefore, most attempts to model soot oxidation in flames have, by necessity, used a relation based on oxidation by O2 and then applied a correction factor to augment the rate to approximate the effect of oxidation by radicals.

2.4.2. CANONICAL EXPERIMENTS ON SOOT FORMATION AND CONSUMPTION

Experimental studies performed for soot formation and consumption are performed roughly for the last 30 years. These experiments gave researchers better understanding on how different species and operating conditions affect the overall soot volume fractions, soot concentration and soot particles size distribution during typical combustion configurations. These experiments also explain the dependence of different steps of soot formation, such as particle inception, surface growth, and coagulation based on the results of their respective experiments.

Some of the earlier experiments performed to understand the mechanics behind soot formation were done for laminar premixed flames. While measuring soot volume fractions, soot concentrations and soot particles sizes, these experiments also tried to address the underlying reactions that are present during soot particle and soot surface growth based on their experimental data. Takahashi and Glassman [42] investigated the critical sooting equivalence ratio for various hydrocarbons starting from acetylene(C2H2) up to naphthalene and discussed the effect of thermodynamic parameters on sooting limits of the hydrocarbons. Harris [43] measured the particle nucleation rate and net surface growth rate of soot particles in an atmospheric pressure ethylene-oxygen flat flame and discussed the possible factors that affected the inception and net growth rate and measured the particle size distribution during particle inception. McKinnon [44] investigated the role of PAH and acetylene in the soot nucleation and growth mechanisms for a flat benzene/oxygen/argon flame. Zhao [45] and Oktem [46] investigated the premixed ethylene flame to determined temperature, soot volume fraction and particle size distribution function (PSDF) and both studies derived particle size distribution functions based on their measurements on both particle inception and particle growth.

Shock tube experiments were done to understand the soot formation under higher pressure and for more complex species for soot formation at premixed mixtures. Alexiou [47] studied the soot formation during argon-diluted mixtures of toluene and n-heptane and of toluene and iso-octane in a reflected-shock tube and constructed a kinetic model to model the experimental results. Kellerer [48] experimented on soot formation from methane, ethylene, acetylene, propane and n-heptane under 15-100 bars of pressure for rich burning conditions and investigated the effect of pressure on soot formation and growth rates. Douce [49] experimented on even higher-pressure range and heavier hydrocarbons then Kellerer and investigated the soot formation and growth for different oxygen content, temperature, and pressure range.

Apart from laminar premixed flames, researchers also investigated soot formation for laminar non-premixed flames. Mauss [36], Santoro [50] and Moss [51] are some of the researchers who investigated the soot formation and oxidation for laminar non-premixed co-flow flames. Santoro conducted experiments on ethene/air laminar diffusion flames to investigate the effect of fuel flow rate on overall soot yield by varying particle residence time, flame geometry and growth rate on the soot yield. Moss developed a soot formation model based on laminar flamelet approach by experimenting on ethylene-oxygen laminar co-flow diffusion flames. Like Mauss, Moss experimented on laminar ethylene-oxygen co-flow diffusion flames to investigate the effect of ethylene on soot formation and numerically simulated the experiments.

Vandsburger [52] and Mauss [53] investigated the soot formation for laminar counterflow non-premixed flames. Vandsburger conducted experiments on ethylene and propane flames and investigated the effects of varying oxygen concentrations on soot formation and overall soot yield. Mauss [53] studied the formation, growth and oxidation of soot for acetylene-air flame and compared the experimental results with the numerical model they developed.

Table 2.4: List of Experiments on Soot Emissions

Experimental configuration	System	Authors
Homogeneous Mixture(Shock tube)	CH4/CH2/C2H4/ C3H8/CH7-air	Kellerer et al.[48]
	C6H5-CH3-AR-O2	Alexiou/Williams [47]
	C6H5-CH3/C11H10/ C13H20 Ar-O2	Douce et al.[49]
Laminar Premixed Flame	C2H2-air	Takahashi & Glassman[54]
	C2H4-Ar-O2	Harris et al.[43]
	C6H6-Ar-O2	Mckinnon/Howard[44]
	C2H4-Ar-O2	Zhao et al.[45]
	C2H4-Ar-O2	Oktem et al[46].
Laminar nonpremixed counterflow flame	C2H4/C3H8-N2-O2	Vandsburger et. al[52]
	C2H4-air	
	C2H2-air	Mauss et al.[53]
Laminar nonpremixed coflow flame	C2H4-air	Santoro et al.[50]
	C2H4/N2-air	Moss et al.[51]
	C2H4/N2-air	Smooke et al.[55]

2.4.3. MODELS ON SOOT FORMATION AND CONSUMPTION

The success of a soot emission model relies on correct description of both soot formation and soot consumption at the same time, which are competitive and affect the final soot yield in a combustion process. Unlike other aviation emissions, such as NOx, soot emissions are hard to model due to its complex dependence between soot chemical kinetics, flame structure and flow physics. During the studies to model soot emissions for both laboratory conditions and real engines, various soot models are presented in the literature. These models can be categorized under three main branches: empirical models, semi-empirical models and detailed models. This section will present some of selected soot models present and their applications in the literature.

Empirical models for soot emissions provide quick estimate on soot yield for a certain engine/laboratory condition and these models rely on parameters such as equivalence ratio, inlet temperature, pressure, flame structure, engine load, and flow speed. These models cannot be used for other engines and laboratory conditions but can be utilized for time effective zero/one dimensional combustion models. In semi empirical soot models, some aspects of chemistry and physics occurring during combustion processes are tried to be implemented. This approach to include some aspects of the combustion phenomenon rather than experimental data correlations lead to steer these models to have two equations: one for soot volume fraction fv and one for soot number density N. In these two equations, rate equations for reactions, such as nucleation, surface growth, oxidation and coagulation, that increase and decrease soot mass and number density are present.[56]

Detailed soot models include most of the reactions that are currently known to be contributing to soot formation and consumption in the time they are proposed. These models represent nucleation, surface growth, oxidation and coagulation of soot particles with as much detail as possible. The detailed models are usually coupled with statistical models to model soot particle size distribution (PSD). There are three main statistical methods use in detailed soot models: method of moments, discrete sectional method, and Monte Carlo methods. These methods are employed to calculate the particle size distribution either in an approximate way or by solving for a mean value. [56]

The method of moments(MOM) is the most commonly used statistical model for soot simulations. This apporach computes the moments of the soot PSD. Method of moments uses logarithmic polynomial interpolation for the closure of its equations. The reason for its popularity lies on the model being computationally inexpensive because the number of equations solved range from 3 to 6. Due to this, the MOM is implemented for modelling the soot formation for complex and large-scale applications [57]. The downside of this model is that the model cannot estimate the exact PSD of the soot but provide mean values for the soot PSD. Due to this, a distribution type should be assumed to estimate the PSD.

An alternative based on MOM formulation is quadrature method of moment(QMOM), which evaluates the abscissas and weights of the quadrature approximation from the moments of PSD and provide more detailed information for the class sizes included in the PSD. The closure of the equations are done by an efficient moment construction and inversion algorithm, which provides numerically stable solutions for most of its application. Like MOM, QMOM calculations need a presumed distribution type for the PSD it is using [56].

Both MOM and QMOM are not suitable to assess the real time progress of soot PSD. In order to overcome this limitation of the standard MOM and QMOM, a numerically robust and light-weight population balanced model was formulated name direct quadrature method of moments (DQMOM) model or the moving section population balance model. The DQMOM introduces additional transport equations which directly resolve the nodes and weights of the quadrature approximation of the number density function with an internal coordinate such as particle size. This novel approach enables the prediction of the real-time size distribution and hence, further extends the capability and improves the accuracy of soot model [56].

In discrete sectional method, the soot particle size is first discretized into a finite number of sections/ classes/ bins, and the number of soot particles in each section is subsequently evaluated individually rather than inferring to derivative variables. The main advantage of sectional method is that it allows detailed information on the particle size classes that contribute to the PSD. There are two disadvantages of sectional methods. The first disadvantage is the model becomes computationally expensive to provide accurate representation of the PSD. Since soot particle sizes can vary in a broad range based on the simulated flame or combustion conditions, the equations evaluated can become quite substantial. The second disadvantage is the model needs prior knowledge on the node and width of the sections for the particles size classes.

2.5. RICH-BURN QUICK-QUENCH LEAN-BURN (RQL) COMBUSTORS

The Rich-Burn, Quick-Mix, Lean-Burn (RQL) combustor concept was introduced in 1980 as a strategy to reduce oxides of nitrogen (NOx) emission from gas turbine engines and later targeted by National Aeronautics and Space Administration (NASA) in 1990's to reduce NOx emissions in the next generation aero-engines [7]. RQL combustors are used by most of the big engine manufacturers. Pratt & Whitney(P& W) has developed TALON (Technology for Advanced Low NOx) RQL combustors. These engines include TALON I that powers PW4098 engine, TALON II that powers PW6000 engine and TALON X that powers PW1500, PW1130G-JM, PW1133G1-JM engines. Roll Royce used the RQL combustors in their Trent-1000 engines and GE used RQL combustors in their CFM56 series engines.

The main working principle and distinct zones in the RQL can be seen in Figure 2.11. In RQL combustors, the combustion first starts at a fuel rich mixture in the primary zone. The primary zone operates with equivalence ratios between 1.2-1.8 [7]. The rich burn in the primary zone has the advantage of enhancing the stability of the combustion and minimizing the NOx production by keeping the operating temperatures in this zone relatively low and generating lower amount of oxygen containing intermediate species. After the primary zone with the rich burn, a large portion of the dilution air is admitted rapidly in the mixing section to oxidize CO, UHC and smoke that couldn't be exhausted in the rich burn zone and lowering the equivalence ratio substantially. The air in this section is admitted to this zone in a rapid manner to avoid local equivalence ratios closer to unity and avoid NOx formation [8]. The quick mixing zone is then followed with a lean burn zone to consume the remaining CO and UHC from the previous zone. The exit of the lean burn zone includes main combustion products of CO_2, N_2, O_2 and H_2O. This zone operates with equivalence ratio in the range of 0.5-0.7. [8]

Figure 2.11: Rich-Burn/Quick-Mix/Lean-burn combustor equivalence ratio distribution[7]

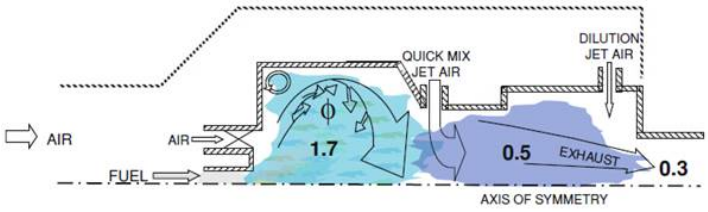

This operating scheme minimizes the NOx production by avoiding peak flame temperatures and peak NOx production by first burning the fuel rich and quickly transitioning to lean burn by the addition of rapid air in the mixing zone which can be seen from Figure 2.12.

Figure 2.12: NOx emissions as a function of Air to Fuel ratio [8]

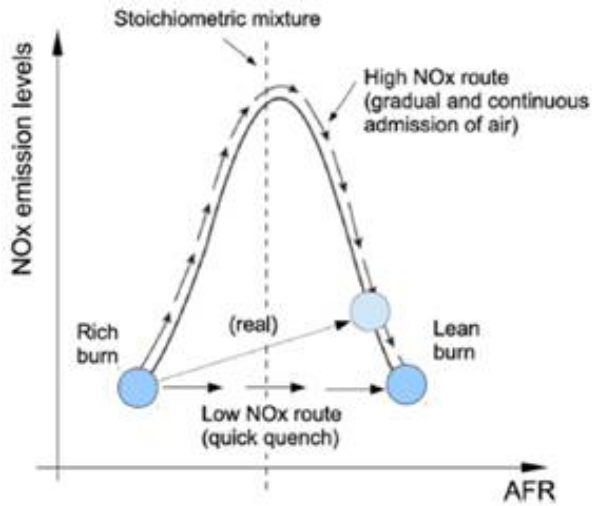

RQL combustors include many advantages which can be listed as:

- Wide operational limit due to elimination of flashback and lean blow out risks with rich burn in primary zone
- Rich burn in the primary zone provides high level of resistance to the lean blow out, especially in low power conditions where combustors operates in very lean conditions
- Lack of oxygen in the lean burn discourages NOx production from fuel bound nitrogen
- It can meet with the full range of combustion system requirements such as safety, relight capability, operability and emissions requirements
- Lower development cost because it is based on conventional combustion technology

Some of the disadvantages of RQL combustors:

- Relatively higher smoke/soot emission due to the rapid mixing in the quick quench zone
- Difficulty in meeting the NOx requirements with increasing engine overall pressure ratios due to the current fuel injection mechanism
- And improved cooling scheme is needed to manage the use of dilution air and improve liner durability due to higher luminous flame radiations from rich burn in the primary zone
- Cooling of the primary section should be designed carefully to avoid peak NOx formation

2.6. REACTOR NETWORKS USED TO MODEL RQL EMISSIONS

There are studies available in literature that uses CRNs to predict NOx, CO, UHC and soot emission of aero engines, including aero engines with RQL type combustors. One of the first example of CRNs used for aero engine emission prediction is from Rizk and Mongia[9]. In their paper, they lay the CRN configurations for an RQL, diffusion flame and lean premixed combustion chambers that use kerosene as fuel. They used the proposed CRNs to estimate the NOx, CO and UHC emissions. By using the results, they also derived correlations between said emissions and parameters such as: temperature, residence time, and equivalence ratio. The reactor network proposed in their study is shown in Figure 2.13.

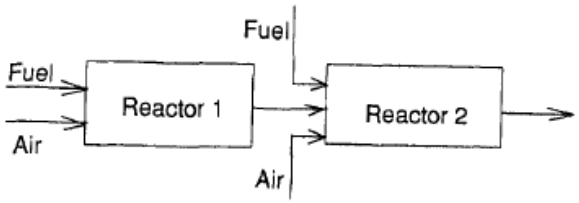

Figure 2.13: Reactor scheme proposed by Rizk and Mongia [9]

Most studies that utilize CRN for aircraft engine emissions are using the schemes proposed by Rizk and Mongia's as their reference. One of most recent study of such is from Rezvani [10] In their study, Rezvani propose a CRN scheme that uses a modified version of the CRN from Rizk and Mongia for the emission prediction section of their whole design campaign. Rezvani modified the CRN scheme proposed by Rizk and Mongia by increasing the number of parallel reactors used to represent the primary zone and by adding more reactors in the post flame zones to model secondary and dilution zone. Along with the parallel reactors, Rezvani used Heywood mixing parameter to allocate the equivalence ratio for the parallel reactors in the primary zone to represent the unmixedness in the primary zone. The proposed model uses a reduced reaction mechanism for kerosene by Roberts [58]. The CRN proposed in the study uses CRNs developed in this study simulate NOx and CO emissions of a NASA Energy Efficient Engine which are compared with the actual emission data of the engine.

In the last few years, researchers started to extend the use of CRNs to predict soot emissions from industrial gas turbines and aero engines. One of the such use is presented by Choo [11]. The CRN developed by the group only models the primary zone of a combustor. The CRN for the primary zone is constructed

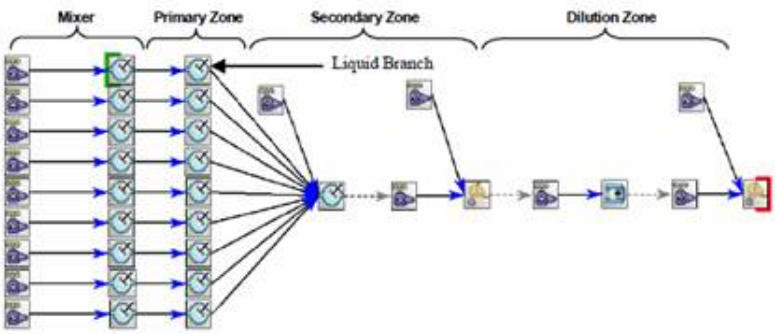

Figure 2.14: The CRN scheme proposed by Rezvani [10]

in CHEMKIN, a commercial chemical kinetics solver. Like Rezvani, this study tries to capture the unmixedness in the primary zone by assigning the equivalence ratio to the parallel reactors in the primary zone with a statistical PDF approach. The statistical method used in the model is based on beta distribution function. The CRN developed in this research uses a detailed kerosene reaction mechanism from Dooley and a semi-empirical soot reaction mechanism proposed by Lindstedt [59] The developed CRN firstly estimates the concentrations of soot precursors in the fuel rich section of the primary zone. The empirical equations taken from literature then used with the predicted precursor concentrations to predict the soot formation rate and total soot yield. After establishing the model, they calibrated CRN with turbulent non premixed flame data from the literature. The CRN used in the research is in Figure 2.15

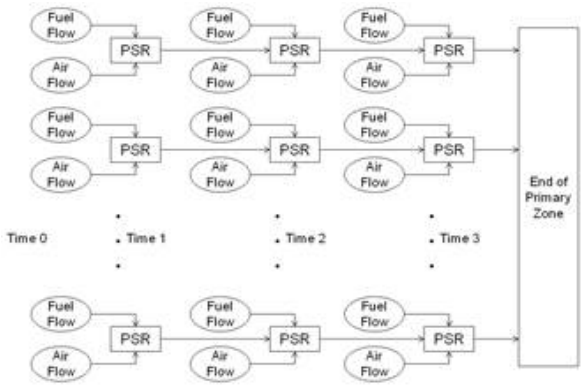

Figure 2.15: The CRN scheme proposed by Choo [11]

Another CRN based emissions prediction model for aero engines is proposed by Moniruzzaman [12]. This model is using multi-parcel gas model with a sectional aerosol dynamics module for soot size distribution that is coupled with a detailed jet fuel combustion reaction mechanism of hydrocarbon, polyaromatic hydrocarbon, nitrogen, and sulfur chemistry [12]. The model developed can predict the temporal evolution and total emissions of CO, NOx, UHC, and soot. The developed emission model is used to simulate the measured emissions data from Aircraft Particle Emissions eXperiment (APEX) campaign of an RQL based CFM56-2-C1 aero engine. The novelty of this study compared to other soot emission prediction models is the use of gas parcels to model unmixedness in each section of the combustion chamber. In this approach, the equivalence ratio of the parallel reactors is designated by a distribution function, like Rezvani. The main difference in this model is, each zone of the combustor (primary, dilution, and turbine & nozzle zone) is modeled with mixed and unmixed parcels where unmixed parcels in each section exchanges mass with the singular mixed parcel over time. The evolution of the mass content of the gas parcels used in the model for different time sections can be seen from Figure 2.16.

Figure 2.16: The temporal evolution of gas parcel distribution in the CRN model by Moniruzzaman [12]

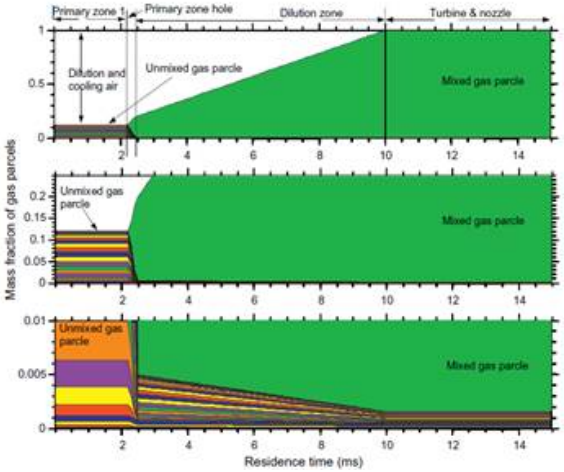

3

METHODOLOGY

3.1. CHEMICAL REACTOR NETWORKS

3.1.1. CANTERA

Cantera is an open source object oriented software that includes multiple modules to solve reacting flow problems. The capability of Cantera extends to topics such as thermodynamics and transport properties, homogeneous and heterogeneous chemistry, chemical equilibrium, reactor networks and steady 1D flames. Cantera can be used with C++, Fortran 77, Fortran 90, Python, or MATLAB environments.[60] For this thesis, Cantera's capabilities on reactors networks are utilized to model emissions for an RQL type combustion chamber. Cantera uses several objects to form the reactor networks. The models used are:

- Ideal Gas Reactor: It is a reactor that considers temperature as its state variable. The chemical reactions inside the ideal gas reactor is considered to mix instantaneously and perfectly with the gases inside the reactor. The results of the reactions are bound to the temperature, composition and residence time reached within the reactor[61] . In Cantera, the state of a gas in a Ideal Gas Reactor is usually represented with temperature, pressure and composition(either mass fractions or mole fractions) of the gas phase. Along with these properties and the prescribed sum of inlet mass flow rate to the reactor, Cantera's internal solver solve the conservation equations for the Ideal Gas Reactor. The conservation equations solved for an ideal gas reactor are:
  - Mass Conservation
  $$\frac{\mathrm{d}m}{\mathrm{d}t} = \sum_{in} \dot{m}_{in} - \sum_{out} \dot{m}_{out} \tag{3.1}$$
  - Species Conservation
  $$\frac{\mathrm{d}(mY_k)}{\mathrm{d}t} = \sum_{in} \dot{m}_{in} Y_{k,in} - \sum_{out} \dot{m}_{out} Y_k + \dot{m}_{k,gen} \tag{3.2}$$
  $$m\frac{\mathrm{d}Y_k}{\mathrm{d}t} = \sum_{in} \dot{m}_{in}(Y_{k,in} - Y_k) + \dot{m}_{k,gen} \tag{3.3}$$
  - Energy Conservation
  $$mc_v\frac{\mathrm{d}T}{\mathrm{d}t} = -p\frac{\mathrm{d}V}{\mathrm{d}t} - \dot{Q} + \sum_{in} \dot{m}_{in}\left(h_{in} - \sum_k u_k Y_{k,in}\right) - \frac{pV}{m}\sum_{out} \dot{m}_{out} - \sum_k \dot{m}_{k,gen} u_k \tag{3.4}$$
- Reservoir: Reservoir objects provides flow with perfectly mixed and non-reacting gases. Reservoirs can be used as a source or sink of flow to the reactor network without changing its thermodynamic state or composition.
- Mass Flow Controller: Mass flow controllers are used to maintain the mass flow rate between reactor and reservoir with other reactor and reservoir objects. Mass flow controllers provide mass flow between objects independent of the pressure difference between the objects.

- Valve: Valve acts like a mass flow controller, where it provides a certain mass flow between reactors. Unlike the mass flow controller, the valve will provide mass flow proportional to the pressure difference between upstream and downstream reactors and a constant defined with the following relation:

$$\dot{m} = K(P_{upstream} - P_{downstream}) \tag{3.5}$$

By combining these objects, reactor networks can be formed to represents various reacting flow scenarios, in our case, combustion process inside an aero engine combustion chamber.

3.2. DETAILED SOOT MODELING

The reactor network constructed with Cantera can predict formation of species within the limits of the reaction mechanism used. On the other hand, soot formation contains multiple processes beyond the reach of gas phase reactions. The formation of PAH molecules that make up the initial soot nuclei can be predicted with the reactor network approach since it is within the capabilities of the reaction mechanism used but particle interactions that make up soot particles such as nucleation, surface reactions and coagulation cannot be modeled with reactor network. To model the particle interactions, a detailed soot model that represents the particle interaction that forms soot particles will be coupled with the reactor network model.

The detailed soot model used is Method of Moments with Interpolative Closure(MOMIC).[62] This model solves moments of the particle size distribution of the soot particles. These moments represent the distribution function parameters of the soot particle size distribution such as mean, standard deviation, skewness and, kurtosis. The basis of the MOMIC method is the Smoluchowski's master equations of Brownian coagulation. The Smoluchowski model[63][64][65] represents the temporal evolution of a particle population with an infinite set of differential equations:

$$\frac{\mathrm{d}N_1}{\mathrm{d}t} = -\sum_{j=1}^{\infty} \beta_{1,j} N_1 N_j \tag{3.6a}$$

$$\frac{\mathrm{d}N_i}{\mathrm{d}t} = -\sum_{j=1}^{i/1} \beta_{j,i-j} N_j N_{i-j} - \sum_{j=1}^{\infty} \beta_{i,j} N_i N_j \quad \text{for} \quad i = 2, ...\infty \tag{3.6b}$$

where N in equation set (3.6) is the number density of a particle with size i or j and β is the collision frequency coefficient for the particles i and j. The amount of equations needed to solve equation set (3.6) makes it impossible to reach a closure for the solution of the equations. In order to reduce the number of equations solved, one the techniques used in the literature is method of moments. With method of moments, rather than solving individual equations for each soot particle size, the moments of the distribution of the soot particles are solved. Each moment solved is linked to a parameter of the soot particle size distribution. The first moment is related to the mean of the distribution, the second moment to the variance of the distribution, third moment to skewness of the distribution and fourth moment is related to the kurtosis of the distribution. The moments and reduced moments in method of moments are described as

$$M_r = \sum_{i=1}^{\infty} m_i^r N_i \quad r = 0, 1, ..., 5 \tag{3.7}$$

$$\mu_r = M_r / M_0 \quad r = 1, 2, ..., 5 \tag{3.8}$$

where m_i represent the mass of the soot particle with size i and N_i represents number density of the soot particle with size i. This mass term is represented with the number of carbon atoms contained in the particle. The reduced mass in Equation (3.8) is used to normalize the moments according to the zeroth moment calculated. The reason for the use of reduced moments is that the moments get quite large numerically and normalizing them allows the solvers used to compute their values without exceeding their computational limits.

In method of moments, equation set (3.6) is rewritten as [66]:

$$\frac{\mathrm{d}M_0}{\mathrm{d}t} = R_0 - G_0 \tag{3.9a}$$

$$\frac{\mathrm{d}M_1}{\mathrm{d}t} = R_1 + W_1 \tag{3.9b}$$

$$\frac{dM_r}{dt} = R_r + G_r + W_r \quad r = 2,3,4,5 \tag{3.9c}$$

In the equation set (3.9), R represents the nucleation moment term, G represents the coagulation moment terms and W represents the contribution of surface reactions to the moments. In the current application of the model, 6 moment equations are solved. In the zeroth moment, only the difference between nucleation term and coagulation term is taken because the model assumes the number density of particles can only be increased with nucleation rate and decreased with coagulation. In the first moment, coagulation is not taken into account because coagulation is assumed to conserve the total mass of the soot particles.

The difficulty of solving the moments equations are obtaining closures for the right hand side of the equations. Two methods are proposed by Frenklach [67] to obtain closure for these equations. In Method I, the closure is obtained by approximating $\beta_{i,j}$ by making it independent of particle size. In Method II, rather than approximating the collision coefficient, the whole summation is approximated. In this thesis, the closure of the moment equations are based on Method II by Frenklach[67] and the equations are derived based on this method.

3.2.1. NUCLEATION

In MOMIC, the nucleation is assumed to happen by coalescent collision of two PAH particles that have reached a certain size. The rate of formation of PAH dimers which acts as the soot nuclei are

$$R_r = \frac{1}{2}\beta_{PAH}(M_0^{PAH})^2 \sum_{k=0}^{r} \binom{r}{k} \mu_k^{PAH} \mu_{r-k}^{PAH} \tag{3.10}$$

where β is the collision frequency of two PAH particles, M^{PAH} and μ_i^{PAH} are moments and reduced moments of PAH particles. The collision frequency for two PAH particles are calculated as

$$\beta_{i,j}^{PAH} = \epsilon \sqrt{\frac{\pi k_b T}{2\mu_{i,j}}} (d_i + d_j)^2 \tag{3.11}$$

ϵ is the Wan der Waals enhacement factor, which is 2.2, k_b is the Boltzmann constant, T is the temperature of the gas phase, $\mu_{i,j}$ is the reduced mass of the colliding particles and d is the collision diameter of the PAH particles. The collision diameter of the PAH particles is expressed as

$$d_i = d_A \sqrt{\frac{2m_i}{3}} \tag{3.12}$$

where d_A in this equation is the length of a single aromatic ring,$1.395\sqrt{3} \times 10^{-10}$m, and m_i is the number of carbon atoms of the PAH species.
The moments for PAH species are expressed as

$$M_i^{PAH} = \sum_{i=1}^{\infty} (m_i^{PAH})^r N_i^{PAH} \tag{3.13}$$

$$= \sum_{i=1}^{\infty} (\#C_{PAH})^r (c_{PAH} \times N_A) \tag{3.14}$$

in which the $\#C_{PAH}$ is the number of carbon atoms per PAH. The number density N_i of PAH molecules is calculated as the product of its concentration $c_{PAH}(mol/m^3)$ and N_A is the Avogadro number($6.022 \times 10^{23} mol^{-1}$). In the current model, the PAH particle that is responsible for the nucleation of the soot particles is assumed to be coronene.

3.2.2. SURFACE GROWTH AND OXIDATION

In the MOMIC approach, four main surface reactions are taken into consideration. In the model, the particle growth via surface reactions are assumed by C_2H_2 addition and PAH condensation on the surface of the soot particles and particle consumption is assumed by surface radicals getting oxidized by O_2 or OH. The PAH species assumed during the condensation are pyrene and coronene. The general form of surface growth moment terms are:

$$W_r^k = k_s c_k \alpha \chi_{soot} \pi C_s^2 \sum_{l=0}^{r-1} \binom{r}{k} M_{l+2/3} \Delta m^{r-l} \tag{3.15}$$

where k_s is the per site rate reaction rate constant(m^2/s), given in Table 3.1, c_k is the concentration of surface reaction species(mol/m^3), α is the fraction of surface sites available for surface reactions, χ_{soot} is the number density of surface radicals, and C_s is a constant representing area of a single carbon soot molecule.

Table 3.1: Surface reactions rates [17]

No	Reaction	A	n	E
1a	$C_{soot}-H+H \rightarrow C_{soot}\cdot+H_2$	4.2×10^{10}	-	5.44×10^{7}
1b	$C_{soot}-H+H \leftarrow C_{soot}\cdot+H_2$	3.9×10^{9}	-	4.60×10^{7}
2a	$C_{soot}-H+OH \rightarrow C_{soot}\cdot+H_2$	1.0×10^{7}	0.734	5.98×10^{6}
2b	$C_{soot}-H+OH \leftarrow C_{soot}\cdot+H_2$	3.7×10^{5}	1.139	7.15×10^{6}
3	$C_{soot}\cdot+H \rightarrow C_{soot}-H$	2.0×10^{10}	-	-
4	$C_{soot}\cdot+C_2H_2 \rightarrow C_{soot}-H+H$	8.0×10^{4}	1.560	1.59×10^{7}
5	$C_{soot}\cdot+O_2 \rightarrow 2CO+$ products	2.2×10^{9}	-	3.14×10^{7}
6	$C_{soot}-H+OH \rightarrow CO+$ products		$\eta=0.13$	

3.2.3. PARTICLE COAGULATION

In MOMIC, the soot particle ensemble is considered to be spatially homogeneous, where particle i has volume $v_i = iv_1$. When the particle mass density is assumed to be independent from particle size, the relationship used for particle volume can also be applied to particle mass where particle i has the mass $m_i = im_1$. With this assumption for the mass, the equations 3.9 can multiplied by m_i^r:

$$\frac{dG_0}{dt} = -\frac{1}{2}\sum_{i=1}^{\infty}\sum_{j=1}^{\infty}\beta_{i,j}N_iN_j \tag{3.16}$$

$$\frac{dG_r}{dt} = -\frac{1}{2}\binom{r}{k}\left(\sum_{i=1}^{\infty}\sum_{j=1}^{\infty}m_i^k m_j^{r-k}\beta_{i,j}N_iN_j\right) \tag{3.17}$$

The main difficulty for these summations lies in the non-additive character of the collision coefficient β. β is defined by the coagulation regime of the gas phase, specified by the Knudsen number Kn=$2\lambda_f/d$, where λ_f is the gas mean free path and d the particle diameter. Based on the Knudsen number, the collision frequency term will change. The three regimes considered in this model are continuum, free-molecular and transition regime.

CONTINUUM REGIME

The continuum regime of coagulation is characterized by $Kn \ll 1$. In this regime, the collision coefficient for coalescent collisions of spherical particles is[64]

$$\beta_{ij}^c = K_c\left(\frac{C_i}{m_i^{1/3}}+\frac{C_j}{m_j^{1/3}}\right)(m_i^{1/3}+m_j^{1/3}) \tag{3.18}$$

where $K_c = 2k_BT/3\eta$ and C the Cunningham slip correction factor, k_B is the Boltzmann constant, T is the temperature of the gas phase and η is the viscosity of the gas phase. The Cunningham slip coefficient can be expressed in terms of Knudsen number as $C = 1+1.257Kn$. With this representation of Cunningham slip coefficient and by substituting (3.18) into (3.16), the coagulation moment for continuum regime can be expressed as:

$$G_0^c = K_c[1+\mu_{1/3}\mu_{-1/3}+K_c'(\mu_{-1/3}\mu_0+\mu_{1/3}\mu_{-2/3})]M_0^2 \tag{3.19a}$$

$$\begin{aligned} G_r^c = \frac{1}{2}K_c\sum\binom{r}{k}[&2\mu_k\mu_{r-k}+\mu_{k+1/3}\mu_{r-k-1/3}+\mu_{k-1/3}\mu_{r-k+1/3} \\ &+K_c'(\mu_{k-1/3}\mu_{r-k}+\mu_k\mu_{r-k-1/3}+\mu_{k-1/3}\mu_{r-k-2/3}+\mu_{k-2/3}\mu_{r-k+1/3})]M_0^2 \end{aligned} \tag{3.19b}$$

where $K_c' = 2.514\eta(\pi\rho_{soot}/(6m_c))^{1/3}$, ρ_{soot} is the soot particle material density, and the definition of moments given by Equation 3.19b is extended to include any real value of r.

FREE-MOLECULAR REGIME

The free-molecular coagulation is characterized by $Kn \gg 8$. In this limit, the collision coefficient for coalescent collisions of spherical particles is given by [64]

$$\beta_{ij}^{f} = K_f \sqrt{\frac{1}{m_i} + \frac{1}{m_j}} (m_i^{1/3} + m_j^{1/3})^2 \tag{3.20}$$

where $K_f = \sqrt{6k_B T/\rho}(3/4\pi\rho)^{1/6}$ and multiplier ϵ is the van der Waals enhancement factor. In MOMIC, these summations are evaluated by a double interpolation scheme among moments.
The reason for the double interpolation scheme can be explained by substituting 3.20 to 3.17. This substitution yields

$$\sum_{i=1}^{\infty}\sum_{j=1}^{\infty}(m_i + m_j)^{1/2} m_i^{1/2} m_j^{1/2} (m_i^{1/3} + m_j^{1/3})^2 N_i N_j \tag{3.21}$$

where equation (3.21) is the right hand side of the summation. In the summation, the $(m_i + m_j)^{1/2}$ term cannot be computed because the m_i and m_j are not given a priori. The $(m_i + m_j)^{1/2}$ term is gonna be present in every moment equation for the free molecular regime. To calculate this summation, a grid function is defined:

$$f_l^{(x,y)} = \sum_{i=1}^{\infty}\sum_{j=1}^{\infty}(m_i + m_j)^l m_i^x m_j^y (m_i^{1/3} + m_j^{1/3})^2 N_i N_j \tag{3.22}$$

It should be noted that the equation 3.21 is the grid function at $l = 1/2$. To calculate equation 3.21, the Lagrange interpolation of grid function with whole number l subscript is calculated. The free molecular regime moments with the grid functions are

$$G_0^f = \frac{1}{2} K_f M_0^2 f_{1/2}^{(0,0)} \tag{3.23}$$

$$G_r^f = \frac{1}{2} K_f M_0^2 \sum_{k=1}^{r-1} \binom{r}{k} f_{1/2}^{(k,r-k)} \quad r = 2,3,... \tag{3.24}$$

By trial and error, the the following interpolations of the grid functions for the five-moment model gives small enough interpolation errors[62]

$$\begin{gathered}\log f_{1/2}^{(x,y)} = L_{1/2}(\log f_0^{(x,y)}, \log f_1^{(x,y)}, \log f_2^{(x,y)}, \log f_3^{(x,y)}) \\ \text{for}(x,y) = (0,0),(1,1),(1,2)\text{and}(2,2);\end{gathered} \tag{3.25}$$

$$\begin{gathered}\log f_{1/2}^{(x,y)} = L_{1/2}(\log f_0^{(x,y)}, \log f_1^{(x,y)}, \log f_2^{(x,y)}) \\ \text{for}(x,y) = (1,3),(2,3),;\text{and}\end{gathered} \tag{3.26}$$

$$\begin{gathered}\log f_{1/2}^{(x,y)} = L_{1/2}(\log f_0^{(x,y)}, \log f_1^{(x,y)}, \log f_2^{(x,y)}) \\ \text{for}(x,y) = (1,4)\end{gathered} \tag{3.27}$$

TRANSITION REGIME

Coagulation in between the two limits, the continuum and the free-molecular, is referred to as the transition regime. The collision frequency in this regime is usually expressed by the semi-empirical formula from Fuchs[63]. The functional form of this expression is rather complex for implementation with the method of moments. Pratsinis[68] suggested to approximate the coagulation rate in the transition regime with the harmonic mean of the limit values

$$G_r = \frac{G_r^f G_r^c}{G_r^f + G_r^c} \quad r = 0,2,3,...,5 \tag{3.28}$$

This equation reproduces the formula of Fuchs[63] within about 20% on average and not exceeding 30% [17]

TRANSLATION OF MOMENTS TO SOOT PARTICLE PARAMETERS

Based on the results of the MOMIC approach, certain parameters regarding the soot emissions can be calculated. With MOMIC, the mean number density of the soot particles, soot mean mass density, soot mean volume fraction, soot mean particle diameter, and soot mean particle surface area can be computed with the following relations

$$N_{soot} = M_0 \tag{3.29}$$

$$M_{soot} = M_1 \tag{3.30}$$

$$f_v = \frac{M_1 m_C}{\rho_{soot}} \tag{3.31}$$

$$\bar{d}_{soot} = \left(\frac{6m_c}{\pi\rho_{soot}}\right)^{\frac{1}{3}} \mu_{1/3} \tag{3.32}$$

where N_{soot} is the soot number density, M_{soot} is the soot mass density, f_v is the soot volume fraction and $\bar{d}_{soot}$ is the mean diameter of soot particles.

LOGARITHMIC LAGRANGE INTERPOLATION

The coagulation moment equations for all regimes require closure for the fractional order-moments. In MOMIC, the closure is accomplished by using Lagrange interpolation among logarithms of the whole-order moments whose values are available at each integration step of moments. The Lagrange interpolation is expressed as

$$P(x) = \sum_{i=1}^{n} \left(y_i \prod_{j \neq i} \frac{(x - x_i)}{(x_i - x_j)} \right) \tag{3.33}$$

The positive-order fractional moments are computed by Lagrange interpolation among logarithms of the all of the whole-order moments

$$\log \mu_p = L_p(\log \mu_0, \log \mu_p, ..., \log \mu_{r_{max}}), \quad p > 0 \tag{3.34}$$

where operator L_p represents Lagrange interpolation with respect to p, the moment order, and $\mu_{r_{max}}$ is the maximum whole-order moment computed with 3.16. In the case that order of the moment computed is negative, the negative-order moments are computed with the the Lagrange interpolation with the first three moments

$$\log \mu_p = L_p(\log \mu_0, \log \mu_1, \log \mu_2), \quad p < 0 \tag{3.35}$$

3.3. INTEGRATION OF CHEMICAL REACTOR NETWORK WITH DETAILED SOOT MODEL

The general flow of coupling CRNs with MOMIC calculation is shown in Figure 3.1. The modeling approach to model the emissions using CRNs with the detailed soot model based on MOMIC is two parts. The first part of the approach is using CRNs to model the gas phase kinetics of the combustion for a given inlet mixture and conditions. According to the conditions and the structure of the combustion system, a CRN model is constructed using Cantera, mentioned in 3.1.1. After the construction and solution of the CRN, the results of the CRN is fed to a subroutine that calculates the soot moments for each reactor, acting as post-processing to the CRN results. In the current approach, the soot moment calculations do not assume consumption or generation of species that take role in soot formation.

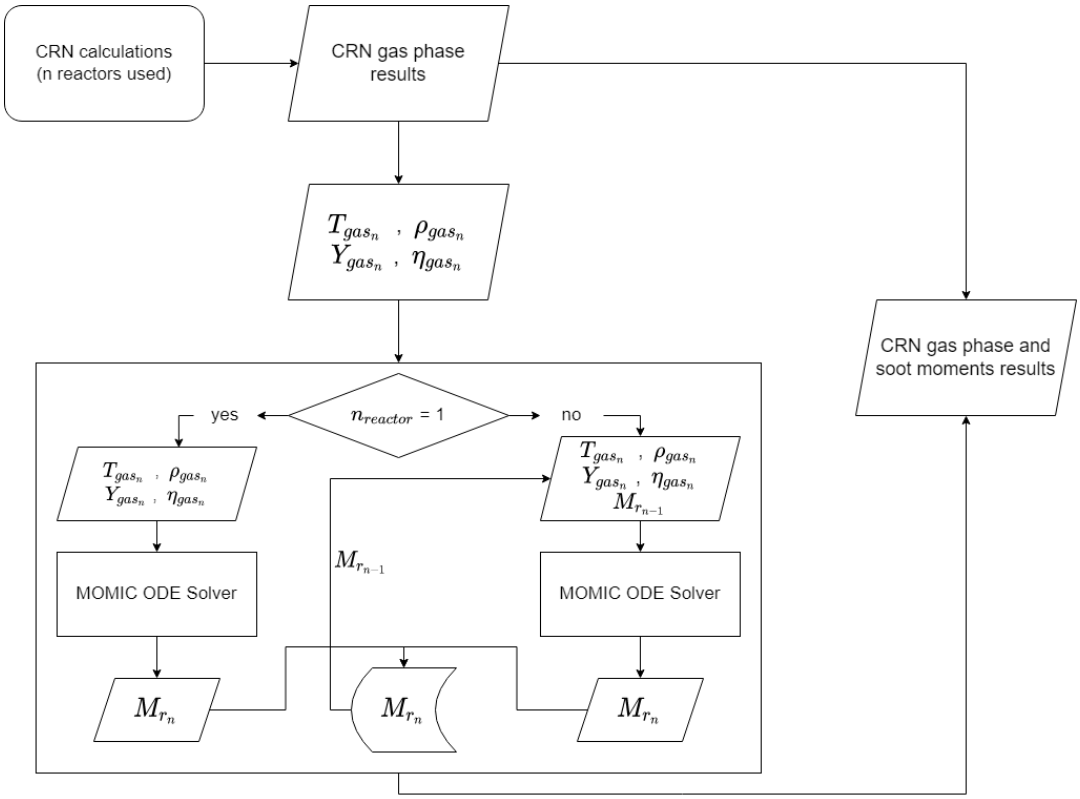

Figure 3.1: Flow Chart for CRN - Detailed Soot Modeling Coupling

The flow chart that shows the evaluation of the moment equations in the subroutine used to solve the MOMIC equations are shown in 3.2. In order to create the moment equations to be solved in each iteration of the ode solver, three functions for nucleation, surface reactions and coagulation are evaluated. To each type of moment term, certain parameters from the CRN calculations are fed. The temperature(T) is fed into the terms to be evaluated in their respective collision frequency terms. The density(ρ_{gas}) and the mass fractions(Y_{gas}) are fed in to terms in order to calculate the number density of the PAH species used or to calculate the concentration of the surface reaction species used. Lastly, the dynamic viscosity(η) is used to calculate Kc constant for the collision coefficient for coagulation in continuum regime as shown in Equation 3.18.

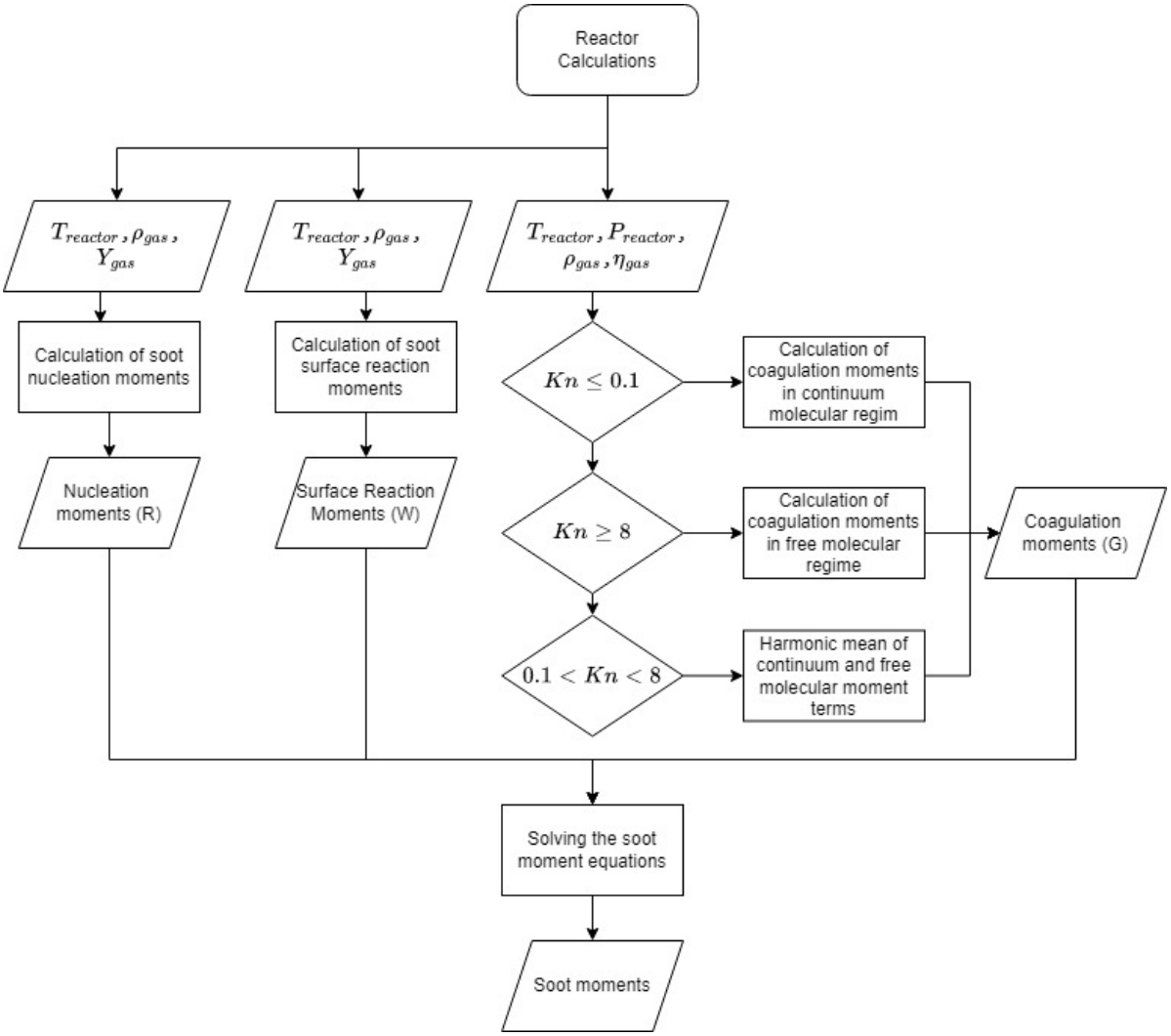

Figure 3.2: Flow Chart for the function evaluation for MOMIC

In the calculation of soot moments, the temperature, density, mass fractions/mole fractions of the gas phase and viscosity of each reactor used in the CRN is taken as input. These inputs are evaluated at different parts of the MOMIC equations. The inputs are fed into a ODE solver written which solves the soot moment equations with ODE15s, a stiff ODE solver present in MATLAB. Based on the location of the reactor or the type of the reactor the soot moments are calculated for, one of the three types of equation sets are solved by the ODE solver. If the reactor evaluated is either at the beginning of the CRN or is the sole reactor in the CRN, the following equations are solved

$$\frac{\mathrm{d}M_r}{\mathrm{d}t} = Q_r - \frac{M_r}{\tau} \qquad \mathrm{r} = 0, N_{moments} \tag{3.36}$$

where Q_r is the change in soot moments calculated with Equation set 3.9, M_r is the soot moments solved and τ is the residence time of the reactor and $N_{moments}$ is the number of moments, which in this thesis is taken as 5.

If the reactor evaluated is located where there is a reactor connected at the upstream of the reactor, the following sets of equations are solved.

$$\frac{\mathrm{d}M_r}{\mathrm{d}t} = Q_r + \frac{(M_r^* - M_r)}{\tau} \qquad \mathrm{r} = 0, N_{moments} \tag{3.37}$$

where the moments from the previous reactor calculation (M_r^*) are also taken into consideration while calculating the results.

Lastly, if the evaluated reactor is a PFR rather than a PSR as in the previous examples, the following formulation is used to calculate the soot moments for a PFR

$$\frac{\mathrm{d}M_r}{\mathrm{d}t} = Q_r \qquad \mathrm{r} = 0, N_{moments} \tag{3.38}$$

4

VALIDATION OF THE MODELING APPROACH

This chapter of the thesis will explain the validation of the detailed soot model developed to estimate the soot mass and number density in conjunction with a chemical reactor network. The first section of this chapter introduces the experimental setup modelled. The second section explains the structure of the modelling effort used to model the experimental setup. The third section showcases the comparison of the modeling results with the experimental results.

4.1. VALIDATION CASES

To validate the approach developed to estimate the soot emissions, two well documented experimental campaigns are chosen. The first experimental campaign used to validate the detailed soot model is for the combustion of $C_2H_4/O_2/N_2$ in a jet stirred reactor(JSR) conducted by Vaughn [69]. In Vaughn's experimental campaign, the formation of various hydrocarbons, major combustion species, polycyclic aromatic hydrocarbons and soot mass density are reported. The experiments are conducted under atmospheric pressure with reactor temperatures of 1628K and 1750K. The equivalence ratio of the inlet flow is varied between 1.4 to 2.4 with residence time ranging from 5ms to 7ms. The second experimental campaign used to validate the detailed soot model is the combustion experiments conducted on the same JSR setup coupled with a plug flow reactor(PFR) by Marr [13]. Marr conducted the experiments for $C_2H_4/O_2/N_2$ under atmospheric pressure and temperatures of 1520K, 1630K and 1705K. The equivalence ratio studied is 2.2. In this experimental campaign, the measurements for various hydrocarbons, major gas species, polycyclic aromatic hydrocarbons, soot mass and mean particle diameter are reported.

There are few reasons for the selection of these experimental campaigns for the validation of the detailed soot model. Firstly, the construction of both setups makes it easy to model the experiments with the modules and reactors available within CRN approach. The jet stirred reactor can be represented as a perfectly stirred reactor due of the degree of mixedness achieved with the JSR. The plug flow reactor section of the experimental setup can be modeled as a plug flow reactor with CRN based on the flow experiments reported by Marr [13], where the flow in the plug flow portion of the setup becomes fully developed early on the axial length of the PFR. The second reason is, uniformity of the reacting flows in both JSR and PFR makes it easier to assess the chemical kinetics within the experimental setup compared to flame experiments. Thirdly, the data provided for the experimental campaigns includes the progress of many gas species including various hydrocarbons, PAHs and, soot particle mass density and soot particle mean diameter. Lastly, both experimental campaigns are complimentary with each other. The conditions assessed by Vaughn for 1628K with $C_2H_4/O_2/N_2$ as inlet flow at ϕ=2.2 are almost identical with Marr's experiment for the 1630K at ϕ=2.2 for $C_2H_4/O_2/N_2$. Marr's experimental campaign doesn't include data about outlet of the JSR, so Vaughn's data provides further confirmation regarding the accuracy of the modeling approach employed to simulate the results of both experiments.

The JSR used for the experiments is a toroidal well stirred reactor with volume of 250cm^3. The construction of the JSR is shown in Figure 4.1a. The JSR is originally developed by Nenniger [70] and all the details regarding the construction, design, thermal and aerodynamic performance of the setup can be accessed from the Nenniger's study. The JSR provides near homogeneous mixing with 32 radially distributed jets that inject the premixed fuel/air mixture into the reactor in near sonic speeds.

The PFR used in conjunction with the JSR at Marr's experiments is shown in Figure 4.1b. The PFR is 50.8 cm long and has a radius of 5.8cm. Under the experimental conditions investigated, the PFR section provides more than 14ms of residence time. The JSR section of the setup is coupled to the PFR with a flow straightener. The flow straightener eliminates the angular momentum caused in the JSR and introduces the flow to the inlet of the PFR without any angular component. During the transition from JSR to PFR, the temperature of the flow drops approximately by 10K. The flow is in the PFR is assumed isothermal based on previous experiments done with the same setup by Lam [71].

(a) Schematic of the toroidal jet stirred reactor used for the experiments

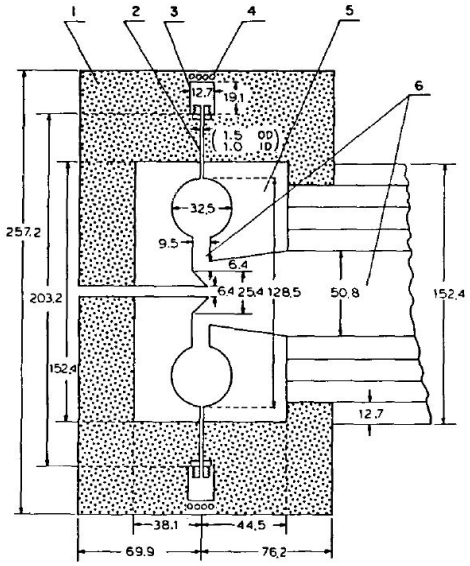

(b) Schematic of the JSR-PFR [13]

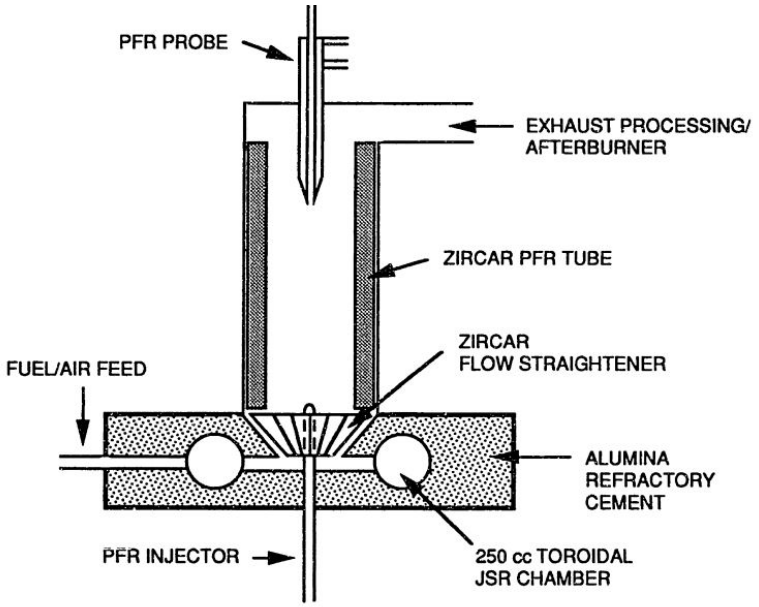

4.2. MODELLING APPROACH

4.2.1. CRN FOR JSR VALIDATION CASE

The structure of the reactor network created with Cantera to model the combustion in the JSR only setup is shown in Figure 4.2. The JSR is modeled as a single PSR. The inlet flow is fed to the JSR with a singular reservoir through a mass flow controller. The composition of the inlet flow at each equivalence ratio is set as reported in the experimental campaign. The mass flow rate into the reactor is calculated by multiplying the inlet molar flow rate with the mean molar mass of the inlet flow. The JSR is then connected to an exhaust represented by a reservoir with a valve object.

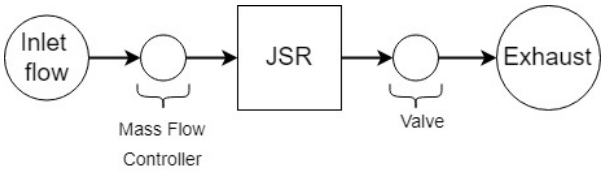

Figure 4.2: Reactor network to model the JSR experimental setup

4.2.2. CRN FOR JSR-PFR VALIDATION CASE

The JSR-PFR setup is modeled with two parts. The JSR portion of the setup is modeled as stated in Section 4.2.1. The PFR portion of the setup is modeled as an ODE solver that solves the PFR conservation equations adapted from Turns et al.[72]. This ODE solver is favored in the modelling effort rather than representing the PFR section as series of PSRs due to the capability of the ODE solver capturing the PFR behavior much more accurately than series approach. The PFR conservation equations are solved with ode15s solver, a stiff ODE solver, in MATLAB. After the CRN constructed for JSR is solved, the exhaust temperature, pressure and mass fractions of the gas phase species along with the mass flow rate from the outlet of the JSR is defined as the initial/inlet conditions of the PFR solver. The complete structure of the JSR-PFR is shown in Figure 4.3.

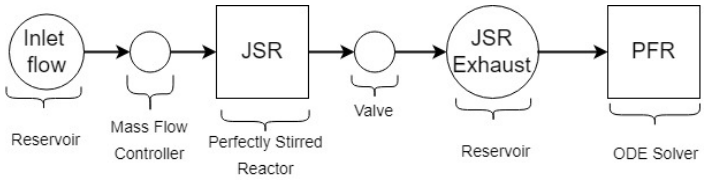

Figure 4.3: Reactor network to model the JSR-PFR experimental setup

The PFR conservation equations adapted from Turns et al. [72] and solved by the stiff ODE solver is shown Equations 4.1. The following assumptions apply to the PFR equations solved:

- Steady-state, steady flow
- No mixing in the axial direction
- Uniform properties in the direction perpendicular to the flow(i.e., one-dimensional flow)
- Ideal frictionless flow
- Ideal-gas behaviour

$$\frac{\mathrm{d}\rho}{\mathrm{d}x} = \frac{\left(1-\frac{R_u}{c_p MW_{mix}}\right)\rho^2 v_x^2\left(\frac{1}{A}\frac{\mathrm{d}A}{\mathrm{d}x}\right)+\frac{\rho R_u}{v_x c_p MW_{mix}}\sum_{i=1}^{N} MW_i\dot{w}_i\left(h_i-\frac{MW_{mix}}{MW_i}c_pT\right)}{P\left(1+\frac{v_x^2}{c_pT}\right)-\rho v_x^2} \tag{4.1a}$$

$$\frac{\mathrm{d}T}{\mathrm{d}x} = \frac{\mathrm{d}v_x^2}{\mathrm{d}\rho c_p}\frac{\mathrm{d}\rho}{\mathrm{d}x}+\frac{v_x^2}{c_p}\left(\frac{1}{A}\frac{\mathrm{d}A}{\mathrm{d}x}\right)-\frac{1}{v_x\rho c_p}\sum_{i=1}^{N} h_i MW_i\dot{w}_i MW_i \tag{4.1b}$$

$$\frac{\mathrm{d}Y_i}{\mathrm{d}x} = \frac{w_i MW_i}{\rho v_x} \tag{4.1c}$$

The equations solved in Equation set 4.1 are to be solved for density, temperature and species mass fractions for every axial location of the PFR modeled. The R_u is universal gas constant, c_p is the specific heat constant under constant pressure, MW_{mix} is the mean molecular weight of the gas phase, v_x is the axial velocity of the gas phase, A is the cross sectional area of the plug flow reactor, MW_i is the molecular weight of species i, $\dot{w}_i$ is the net creation rate of species i, h_i is the specific enthalpy of the species i, T is the temperature and Y_i is the mass fraction of species i.

4.2.3. REACTION MECHANISM USED

The reaction mechanism used for ethylene/air combustion is selected to be the reduced version of KAUST PAH Mechanism 2 (KM2) proposed by Wang et al.[73]. This reaction mechanism is developed for C1–C4 gaseous fuels. The reaction mechanism is validated against various ethylene and propane flames. The reaction mechanism is based on USC Mech[74] and modified to include molecular growth of PAH molecules up to coronene ($C_{12}H_{24}$). The reaction mechanism contains 111 species and 784 reactions.

4.3. RESULTS

4.3.1. RESULTS FOR JSR

For the validation of the model against JSR, Vaughn's experiments for the combustion of $C_2H_4/O_2/N_2$ at T_{JSR} = 1628K, P_{JSR} = 1atm for equivalence range from ϕ=1.4 to ϕ=2.4 are modeled.

Figure 4.4 shows the concentration of major gas species of CO, CO2, H2, O2, C2H2, C2H4 and concentrations of some of the main PAHs, benzene (A1), naphthalene (A2), phenanthrene (A3) and pyrene (A4) are shown. These species are chosen because they contain enough information regarding the performance of the modeling efforts and the reaction mechanism used. The model captures the general trend of major gas species with increasing equivalence ratio and estimates them quite accurately apart from the O_2 concentration. The model captures the increasing nature of O_2 concentration with increasing equivalence ratio but it underestimates its concentration by approximately 25% of the experimental results. The model also captures the increasing state of aromatics with increasing equivalence ratio. The model slightly underestimates the benzene for lower equivalence ratios but the underestimation starts to increase after $\phi = 2$. For naphthalene and pyrene, the model underestimates their values but captures their increasing state with increasing equivalence ratio. Unlike the other aromatics, the model overestimates the phenanthrene concentration for the equivalence ratio range modeled but still captures its increasing trend with increasing equivalence ratio.

Figure 4.4: Concentrations major gas species

(a) CO

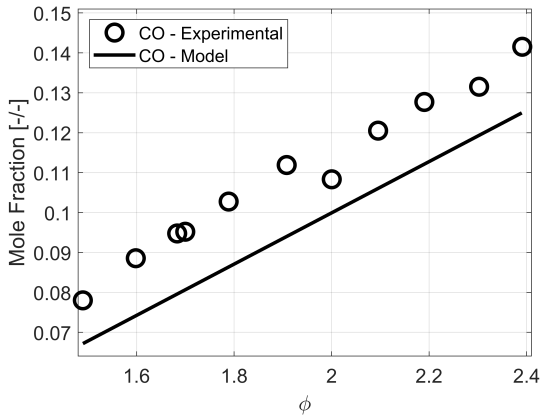

(b) CO2

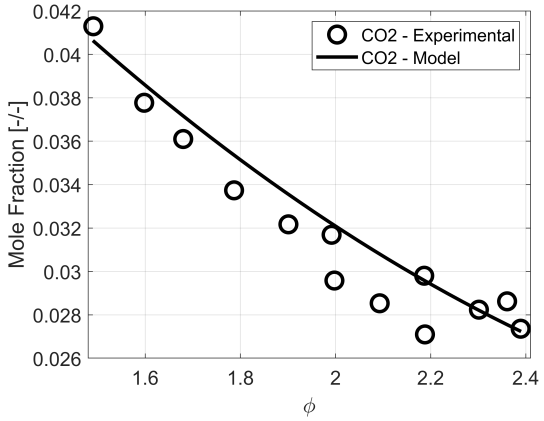

(c) H2

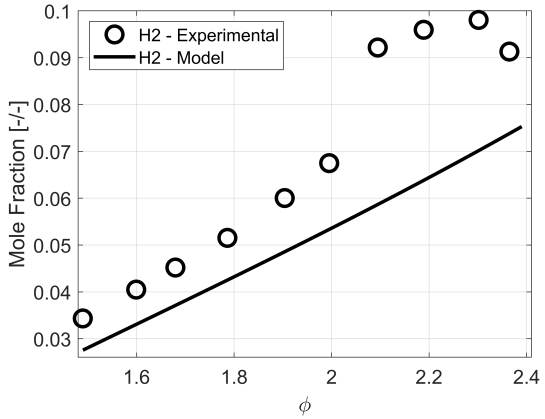

(d) O2

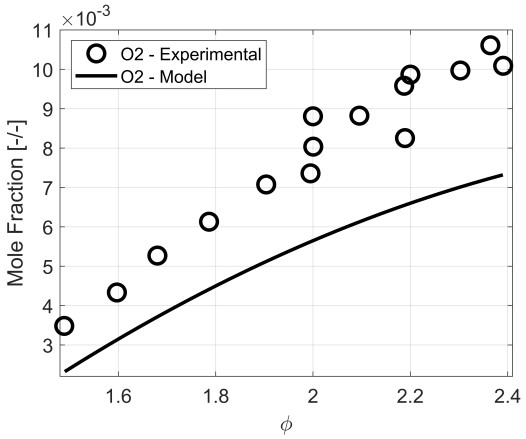

(e) C2H2

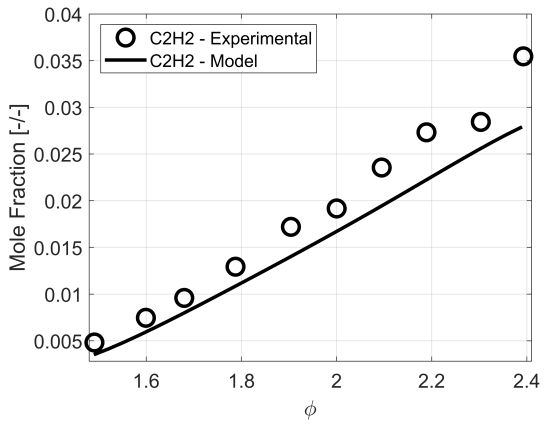

(f) C2H4

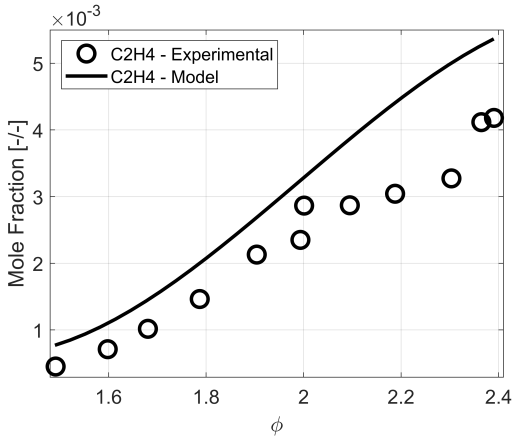

(g) Benzene(A1)

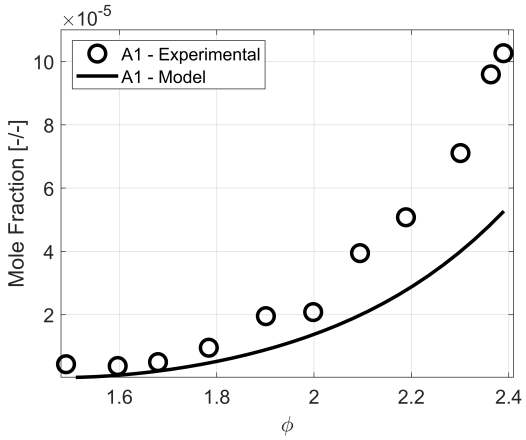

(h) Napthalene(A2)

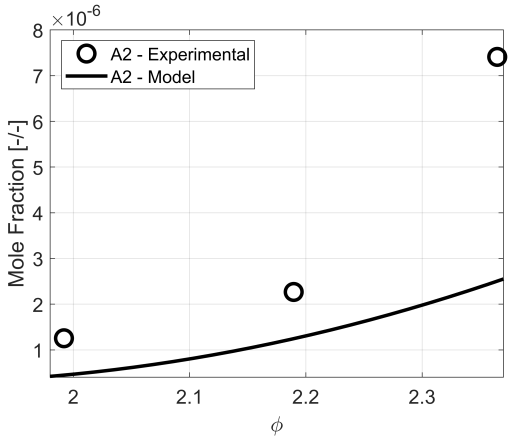

(i) Phenantrene(A3)

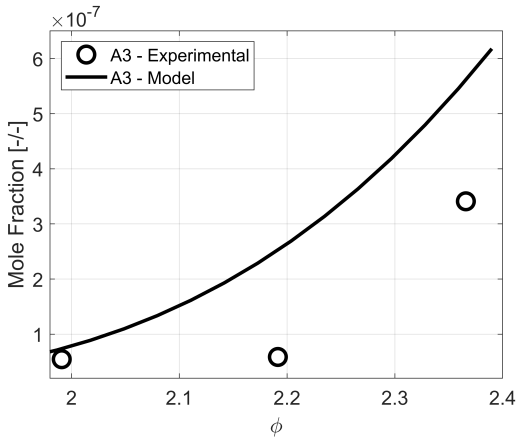

(j) Pyrene(A4)

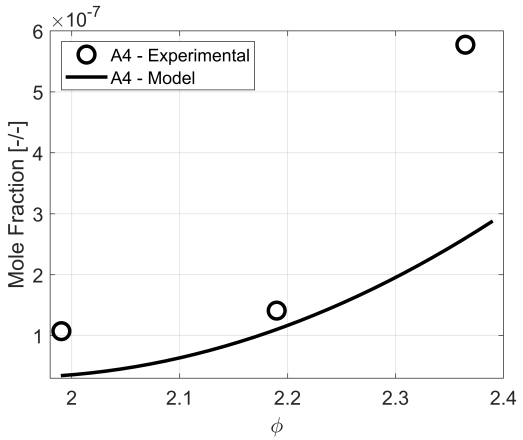

The PSR model seems to estimate the concentrations for the main combustion species within acceptable accuracy apart from O_2. The model also captures the main trend of the PAH species with increasing equivalence ratio but underestimate their concentrations apart from phenanthrene, which is overestimated. The difference between the experimental results and the model might be attributed to model's assumption of complete mixedness within the reactor. The JSR model assumes all the properties of the gas phase inside the reactor as completely uniform due to perfect mixing. In the experimental setup, not all gas phase properties

are constant. The non-uniformity of the gas phase in the experimental setup can be seen from the temperature profiles inside the reactor provided by Vaughn. Figure 4.5 shows the reactor temperature profiles for varying equivalence ratio at reactor temperature of 1750K and 1628K during Vaughn's experiments. As shown in Figure 4.5, there is a certain temperature deviation along the radial direction of the reactor and these deviations increase with increasing equivalence ratio and reach up to ±30K. This variation in temperature might be the reason for the difference between the modelling effort and the experimental conditions.

Figure 4.5: Reactor temperature profile of neat ethylene combustion at 1750K and 1628K

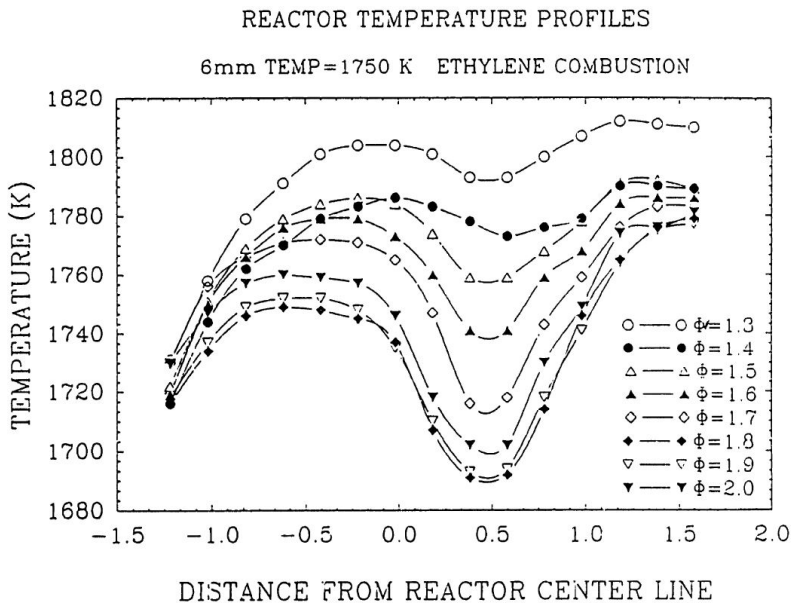

(a) Reactor temperature variation for 1750K [69]

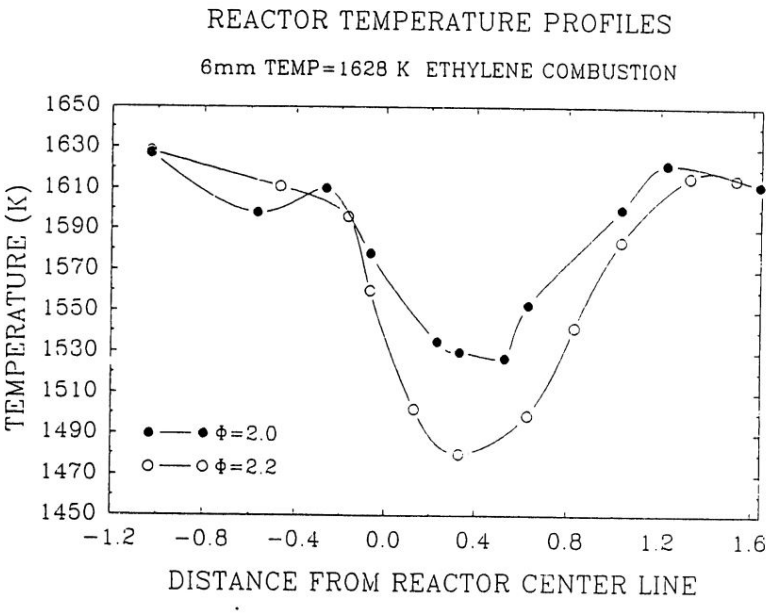

(b) Reactor temperature variation for 1628K [69]

The results for soot mass fractions are shown in Figure 4.6. The model underestimates the soot mass fraction up to $\phi = 2.1$ by half of the experimental values and overestimates the soot mass fraction at $\phi = 2.2$ by 1.5 times of the experimental soot mass density but still predicts the soot mass fraction for the mentioned equivalence ratios within the same order of magnitude. After $\phi = 2.2$, the model starts to overestimate the soot mass fraction with an increasing rate. At $\phi = 2.4$, the model overestimates the soot mass fraction by approximately a factor of 4.

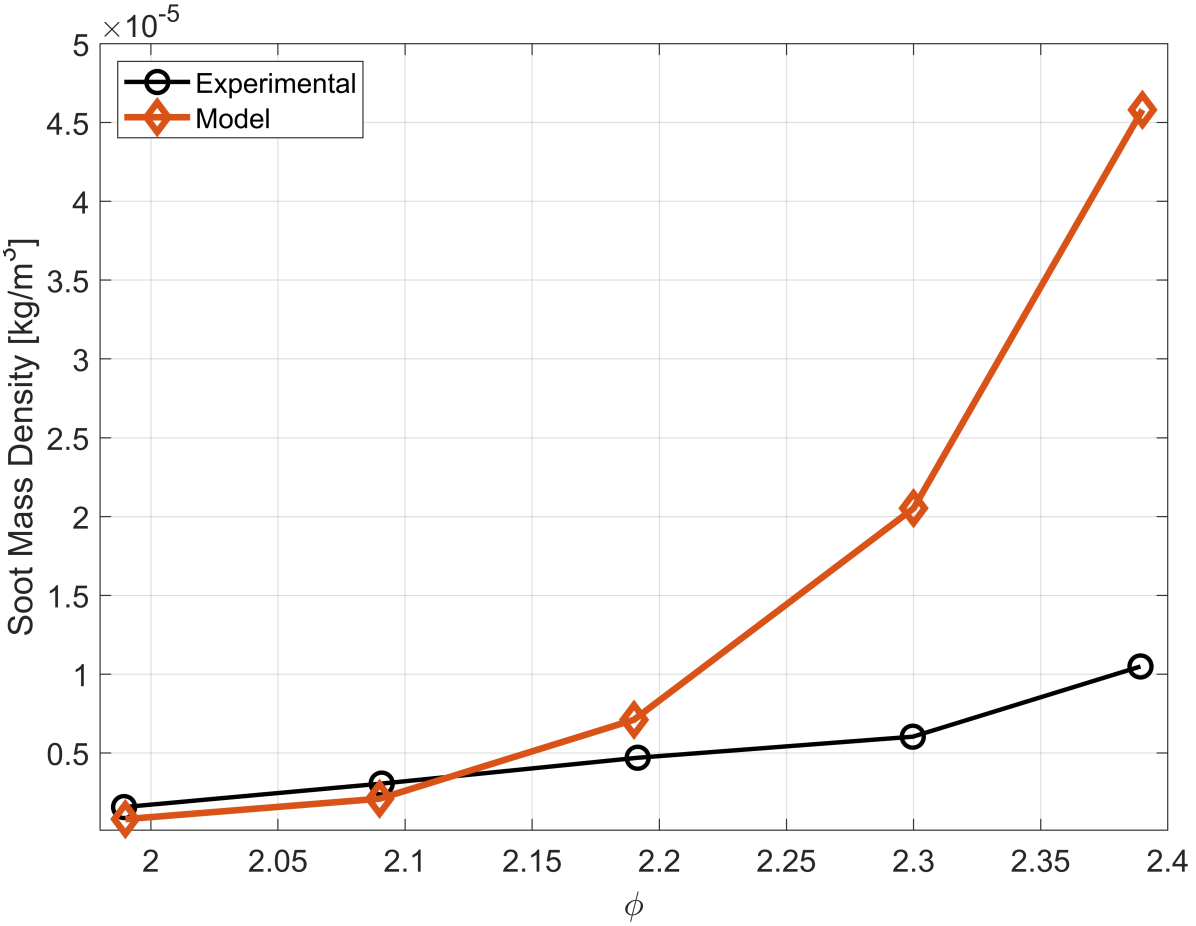

Figure 4.6: Soot mass density results for the JSR experiments

The contribution nucleation, acetylene addition(HACA), oxidation by O2, and PAH condensation on the first soot moment calculated by the model is shown in Figure 4.7. The oxidation by OH is not shown in the figure because its contribution to the soot mass was minuscule compared the other mechanism. Apart from PAH condensation, all of the mechanisms follow a similar trend in increase, only in different orders of magnitude. It seems as the amount of soot particles increase, which can be seen from the increase in nucleation term, the magnitude of the other terms also increase with the amount of soot particles available. For all the equivalence ratios evaluated, the surface growth by acetylene addition or HACA mechanism seems to be the main contributor to the soot mass according to the model. Following HACA mechanism, PAH condensation is the second biggest contributor to the soot mass which is followed by nucleation. The magnitude of the contribution by PAH condensation increases much faster than other additive mechanisms. The surface oxidation by oxygen seems to be not able to compete with the other mechanisms. As the equivalence range evaluated is quite rich, this behavior by the model is expected.

When the behavior of the total soot mass from Figure 4.6 is investigated based on the the contribution of soot formation/oxidation mechanisms to soot mass, two points can be made. For the investigated conditions, the soot mass seems to be most affected by two of the soot formation mechanisms. The first factor is the nucleation term which dictates the amount of soot particles available for surface reactions to occur, and the second factor is the acetylene addition on the soot surface by HACA mechanism which is the main contributor to the soot mass for the investigated conditions. The soot mass seems to be sensitive to one of these two

mechanisms and one or both of these mechanisms seems to be responsible for the overestimation of the soot mass after $\phi = 2.2$.

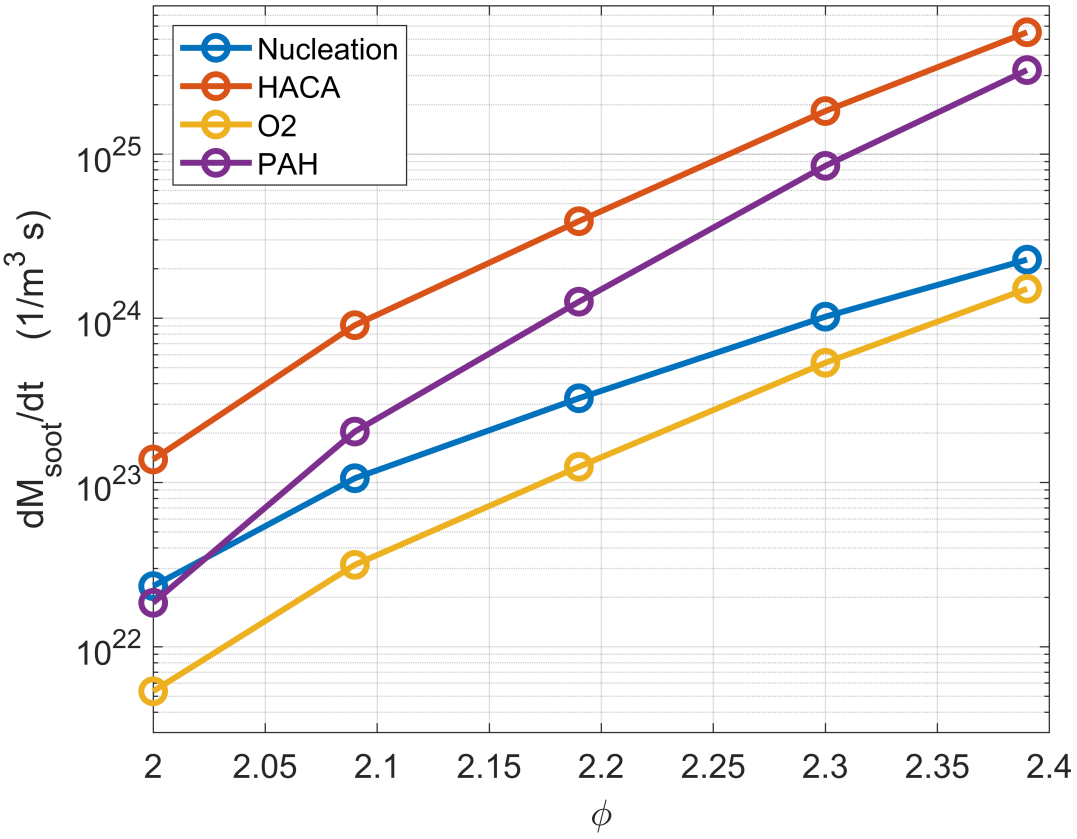

Figure 4.7: Contribution of Nucleation and Surface Reactions to Soot Mass

4.3.2. RESULTS FOR JSR-PFR

For the validation of the model against JSR-PFR setup, Marr's experiments for $C_2H_4/O_2/N_2$ combustion at $\phi = 2.2$, $T_{JSR} = 1630$, $T_{PFR} = 1630$, and $P_{JSR} = 1$atm modeled. Figure 4.8 shows the concentration of CO, CO2,H2, C2H2, CH4 and C2H4. The JSR-PFR model captures the general trend of the major species against increasing residence time but underestimates the CO and H2 species and overestimate the CO2 concentration. For the major hydrocarbon species, the model underestimates their concentration but captures their decreasing trend with increasing PFR residence time. All the species investigated so far are estimated within the error margin of 15% stated for the experimental setup reported by Kronholm[75], who also used the same experimental setup and experimental conditions in his study.

Figure 4.8: Concentrations major gas species for JSR/PFR

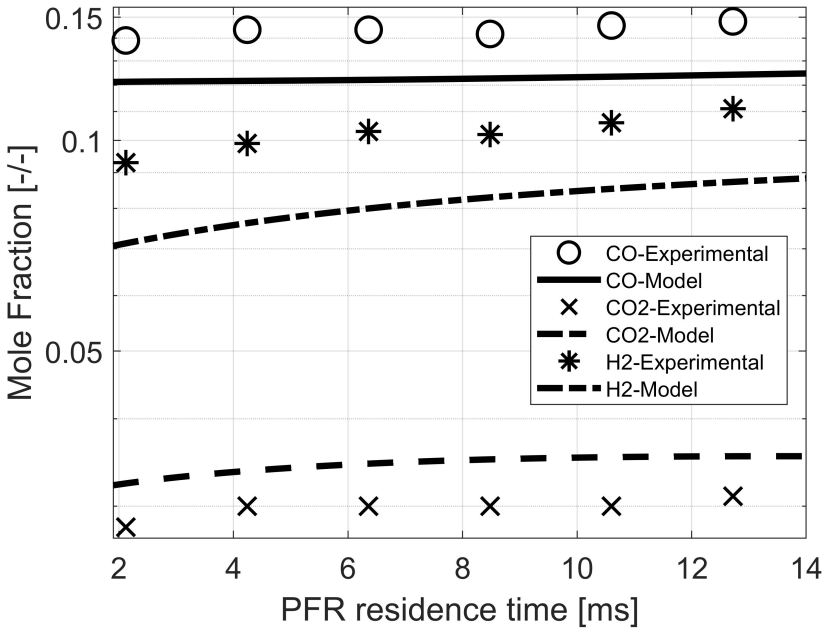

(a) Concentration of CO, CO2 and H2

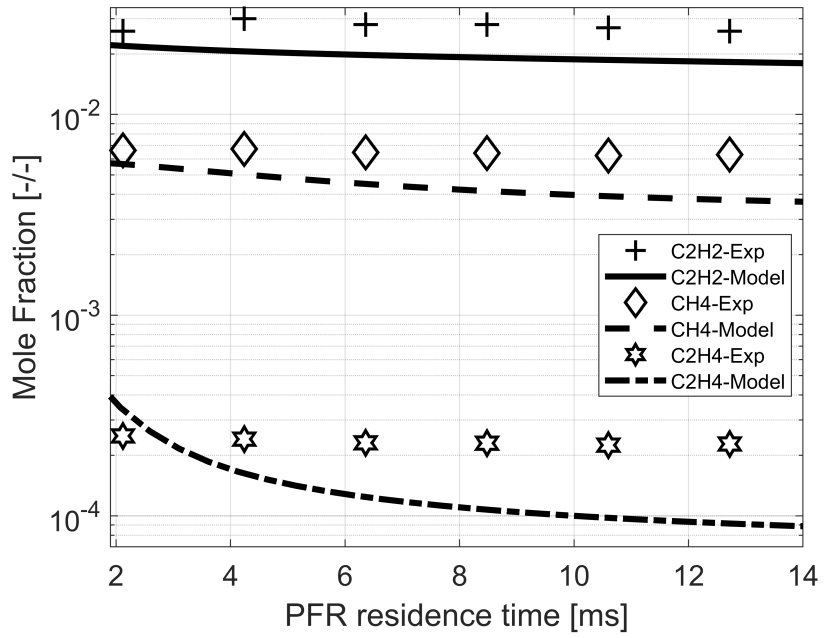

(b) Concentration of CH4, C2H2 and C2H4

The modeling results for the PAH molecules with PFR residence time are presented at Figure 4.9. The model is able to capture the increasing trend of the PAH species with increasing residence time. The model estimates the benzene concentration quite accurately at the beginning of the PFR but assumes the benzene concentration increases in a much higher rate. At the end of the PFR, the model overestimates the benzene concentration by a factor of 4. The model initially underestimates the napthalene concentration by half at the beginning of the plug flow reactor, but like benzene concentration, the model assumes a higher increase rate for the naphthalene. After τ = 7ms, the model starts to overestimate the naphthalene concentration. Lastly, the model consistently overestimates the phenanthrene concentration along the PFR length and underestimates the pyrene concentration.

Figure 4.9: Concentrations Major PAH species for JSR-PFR

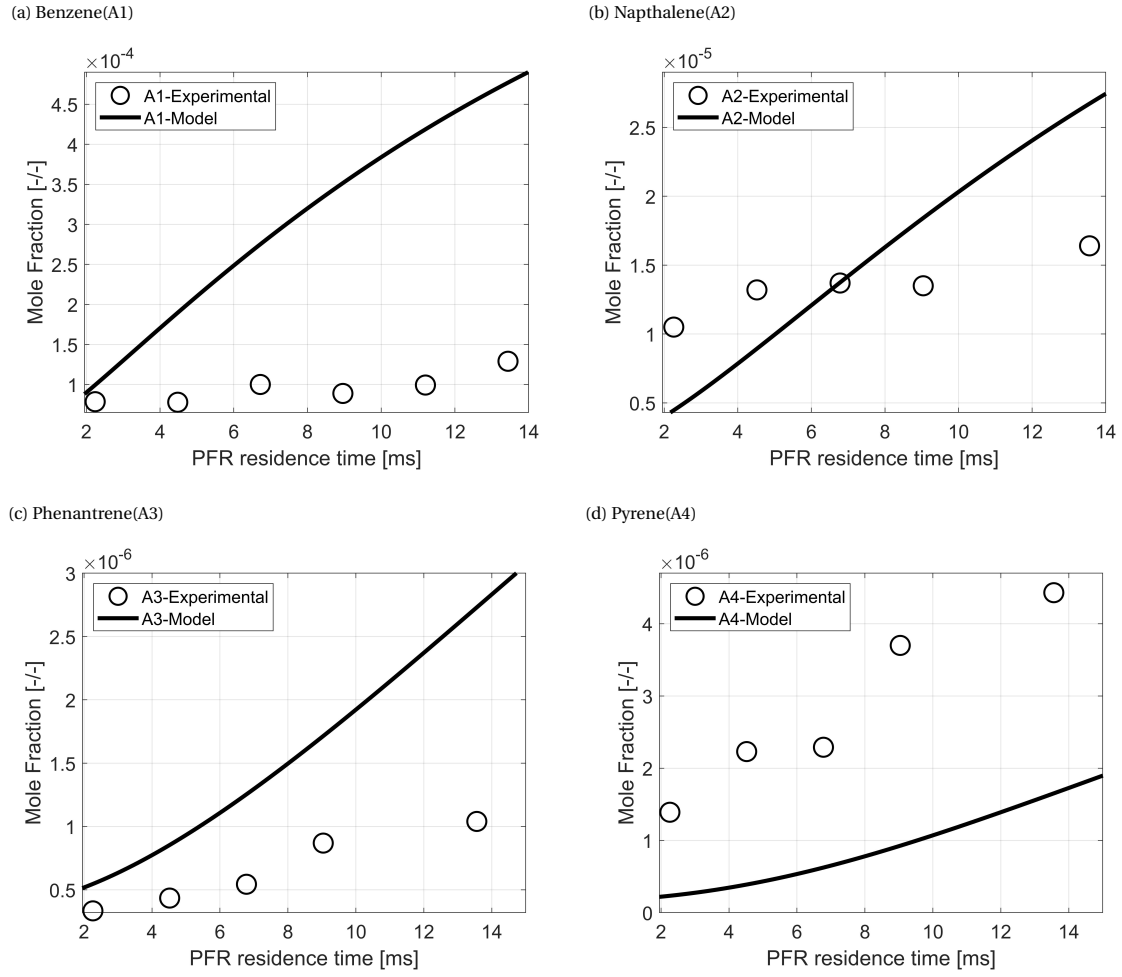

Based on the results reviewed for the PSR-PFR setup, certain comments on the CRN model's performance can be made. In general, the CRN model is capturing the concentration of major gas species within the error rate that is stated by Kronholm [75]. The model is able to capture the increasing trend of aromatics with increasing residence time but either overestimates them or underestimates them within an order of magnitude difference. The CRN model seems to assume the combustion of ethylene is more complete than the experiments based on the underestimation of CO and C_2H_4 and overestimation of CO_2 concentration. This behavior for the results might be due to the PFR model's assumption where the progresses in variables happen in axial direction and the gas phase variable are constant in radial and tangential direction at each axial location. Based on the hot wire anemometry experiments reported in Marr [13], this is not the case for the experimental setup until a certain residence time. The hot wire anemometry done to identify the velocity profiles at various locations of the plug flow reactor is shown in Figure 4.10. Based on this figure, the velocity profile seems to reach a fully developed state after 5 inches of the PFR length. Up to this point,

there are distinguishable variations in the velocity profiles. This variation also suggests potential temperature variations in radial direction of the PFR cross-section until 5 inch length of the PFR, assuming pressure and density is constant in each axial location. This temperature variation might be the reason for the differences between the experimental campaign and the CRN model.

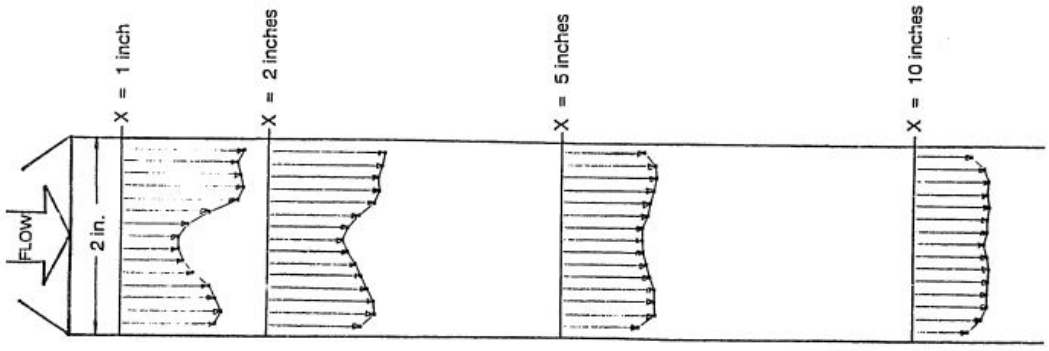

Figure 4.10: PFR flow velocity profiles, as measured by how wire anemometry at varios location above the flow straightener [13]

The modeling results for soot mass fraction are shown in Figure 4.12. The model captures the increasing trend of soot mass fraction with increasing residence time. Initially, the model underestimates the soot mass by half. The model then estimates the soot mass density at τ = 8ms mark but starts to overestimate the soot mass density after this point. The soot mass modeled is approximately 2 times of the experimental model at the last experimental point.

Figure 4.11: Soot mass density for JSR/PFR

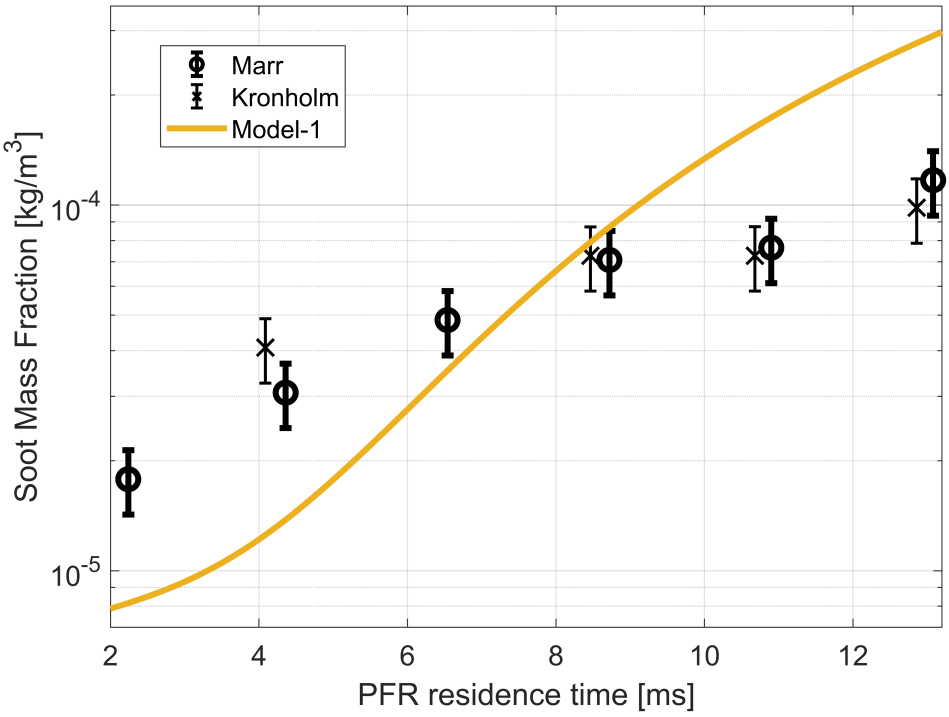

Figure 4.12: Soot mass density

Marr didn't provided any exact numerical data on the number density of soot particles but provided particle number density distribution for varying soot particle diameters for 3 three distinct PFR residence time, which is shown in Figure 4.13.

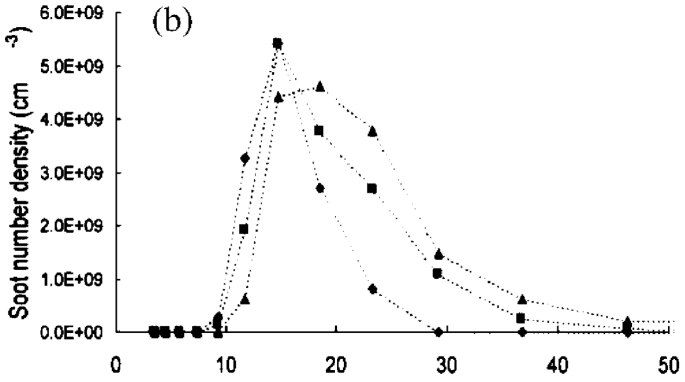

Figure 4.13: Soot particle size distribution vs number density at JSR/PFR setup for τ = 4.1ms(⋄), τ = 8.5ms(□), τ = 12.9ms(△) [14]

Based on this distribution, the total soot particle number density is calculated and compared with the modelling results. The comparison of the number density for the experimental data and modelling effort is shown in Table 4.1. According to the experimental data, the number density of soot particles are increasing but after τ = 8.5ms, the soot number density seems to be not changing too much with increasing residence time. On the other hand, the model assumes the number density of the particles increase continuously with increasing residence time. The bigger difference between the modeling effort and the experimental data is that the model over predicts the number density of soot particles by an order of magnitude of 2. There are few potential reasons for this discrepency which will be discussed in the discussion section.

Table 4.1: Modeled and Experimental Soot Particle Diameters

PFR Residence Time	Number Density($1/m^3$) - Model	Number Density($1/m^3$) - Experimental
4.1	1.24e16	2.40e18
8.5	1.53e16	6.33e18
12.9	1.55e16	9.86e18

The contribution nucleation, acetylene addition(HACA), oxidation by O2, and PAH condensation on the first soot moment calculated by the model for the JSR/PFR experiment is shown in Figure 4.14. The oxidation by OH is not shown in the figure because its contribution to the soot mass was minuscule compared the other mechanisms. The contributions of the mechanisms show a similar trend with the JSR results in the terms of which soot mechanisms dictates the overall mass of the soot emissions. The main contributor to the soot mass is the acetylene addition with the HACA mechanism followed by PAH condensation. On the other hand, the oxidation term seems to decrease with increasing residence time.

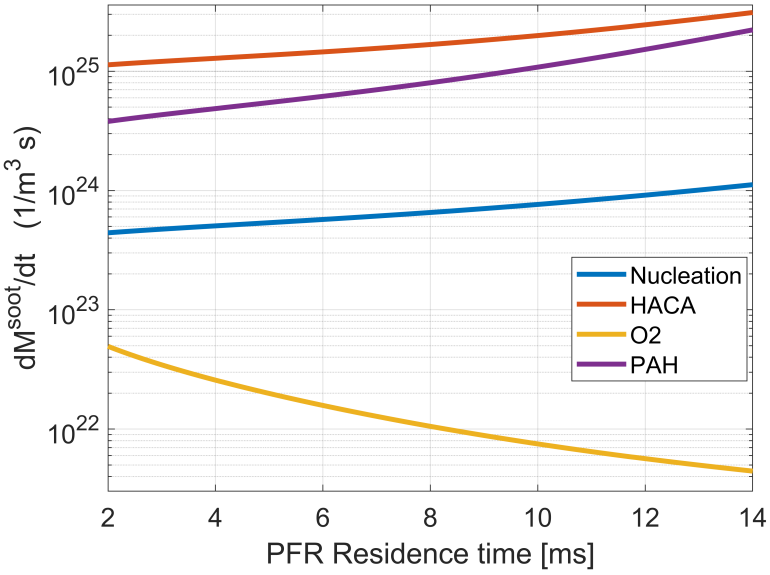

Figure 4.14: Contribution of Nucleation and Surface Reactions to Soot Mass in JSR-PFR experiment

4.4. DISCUSSION

Based on the comparison of the modeling results with the experimental results, some of the main strengths and weaknesses of the MOMIC approach becomes apparent. The model's strength is its ability to predict the soot mass density close to the experimental results based on the selection of the soot precursor species, pyrene and coronene. On the other hand, the model's weakness is its overprediction of the soot particle number density by an order of magnitude of 2. According to the theory and the structure of the soot model, there are three possible reasons as to why the model is overestimating the number density of the soot particles.

The first possible reason might be the underestimation of the coagulation rate. As seen in Equation 3.9a, coagulation acts to decrease the number density, represented as zeroth moment, while increasing mass per soot particle. If the coagulation rate is underestimated, the model might assume the PAH dimers formed are not coagulating enough to decrease the soot particle number density. This possibility also brings out another potential inherent issue with the model in regards to surface growth terms which contribute to soot mass. Surface reactions terms which contribute to the soot mass are calculated based on the amount of soot particles and the average particle surface area corresponding to soot particles. If the coagulation rate is lower than it should be, it means the model is also underestimating the average particle surface area, hence available surface area where the surface growth terms are calculated from.

The second potential reason might be the nucleation moment terms assumed. The number density of the soot particles are calculated from zeroth moment and only nucleation and coagulation is influencing the number density, as seen from Equation 3.9a. The nucleation term used in the moment equations assume the dimer formation is happening by the collision of PAH molecules selected. The nucleation rate is calculated based on the amount of PAH molecules and a certain collision frequency. The nucleation moment term might overestimate the dimer formation either due to the amount of potential PAH molecules colliding are more than it should be or the collision frequency between PAH molecules are bigger than it should be. In order to address , there are two approaches available in the literature. The first approach is addition of another collision coefficient to the nucleation term based on the size of the PAH molecules that participates in the dimer formation [39]. The second approach is to define the dimer formation rate based on a temperature dependant reaction rate which is derived from certain experimental conditions [76]. The application and comparison of these approaches with the current nucleation term might yield a more definitive answer in regards to the accuracy of the nucleation term used in the moment equations.

The last potential reason is the omission of agglomeration mechanism in the calculation of the moment terms. The current system of equations used to calculate the moments of the soot particle size distribution does not take into account the agglomeration of the soot particles. The agglomeration process acts like coagulation where it decreases the number of particles while increasing the mass per particle. The addition of the agglomeration term might be able to decrease the number density of the particles while increasing the calculated soot mass at the same time. There are currently two types of agglomeration terms that can be applied to MOMIC approach which is presented by Frenklach [62] and Balthasar et al.[77]

5

PARAMETRIC STUDY

This chapter will show the results of the parametric study conducted to understand the effect of pressure, temperature, and equivalence ratio on the soot formation and how the model employed behaves for the mentioned parameters. The parametric study is done to understand the behaviour of the model developed for wider operational conditions compared to the validation cases assessed in Chapter 4. Since the model used in Chapter 6 to model the emissions of an RQL combustor assume higher operating pressures, a larger equivalence ratio range, and Jet-A as the fuel rather than ethylene, the parametric study is conducted to bridge the gap between Chapter 4 and Chapter 6, and also understand the behavior of the detailed soot model employed better.

5.1. METHODOLOGY

The simulations to conduct the parametric study is carried out by using CRN that compromises a single PSR, where the structure of the CRN is given in Section 4.2.1 and shown in Figure 5.1. The inlet conditions of the PSR is varied in order to observe the effect of temperature, pressure, equivalence ratio and residence time on the formation of soot particles. In order to keep the residence time constant for varying pressure, temperature and equivalence ratio, the inlet mass flow rate is varied while keeping the reactor volume constant.

Figure 5.1: Reactor network to model the JSR experimental setup

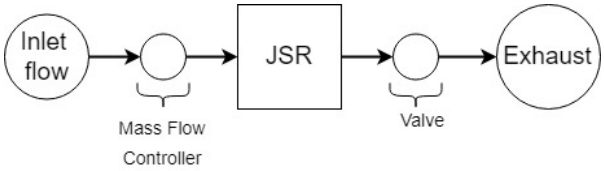

5.1.1. KEROSENE REACTION MECHANISM

Based on the literature survey conducted, no kerosene reaction mechanism was found that included both PAH molecules and nitrogen chemistry at the same time. The only way assumed to have a kerosene reaction of such capability was to combine certain portions of multiple reaction mechanisms. Based on this assumption, the kerosene reaction mechanism is chosen to be the Jet A-1 reaction mechanism developed with hybrid chemistry (HyChem) approach.[33] This approach is proposed as an alternative to surrogate approach for the high-temperature combustion chemistry of jet fuels. The reaction mechanisms developed with HyChem approach models kerosene as a single-component and lumps kerosene's pyrolysis into the seven semi-global reaction steps. The primary pyrolysis products are H,CH4, C2H4, C3H6, 1-C4H8 (1-butene), i-C4H8 (isobutene), C6H6 (benzene), C6H5CH3 (toluene), and the methyl radical CH3. Further pyrolysis of these species are based on USC Mech II. The HyChem Jet-A reaction has a version which includes nitrogen chemistry as well. The nitrogen chemistry subset is taken from Glarborg et al.[78]

The HyChem kerosene reaction mechanism includes single ring aromatics such as benzene and toluene, however it doesn't include bigger aromatics which are required by the soot model investigated in this thesis.

In their study, Gkantonas et al.[15] combined HyChem kerosene reaction mechanism with the PAH routes available in KAUST PAH Mechanism 2[73]. Since both reaction mechanisms are derived from USC Mech-II mechanisms[74], the species and reactions added for PAH route are compatible with HyChem kerosene mechanism. 17 species and 43 reactions are incorporated from KAUST PAH Mechanism 2 for the addition of PAH routes to HyChem. In their study, Gkantonas et al.[15] showed that the addition of the PAH routes does not substantially effect the concentrations of the main pyrolysis and oxidation products. The effect of this the addition of PAH routes to some of the main pyrolysis and oxdiation products are shown in Figure 5.2. Zhang et. al[79] also used this reaction mechanism combination to model soot formation for a kerosene laminar coflow diffusion flame and concluded that this approach is viable to model soot emissions for jet fuel combustion in laminar coflow diffusion flame.

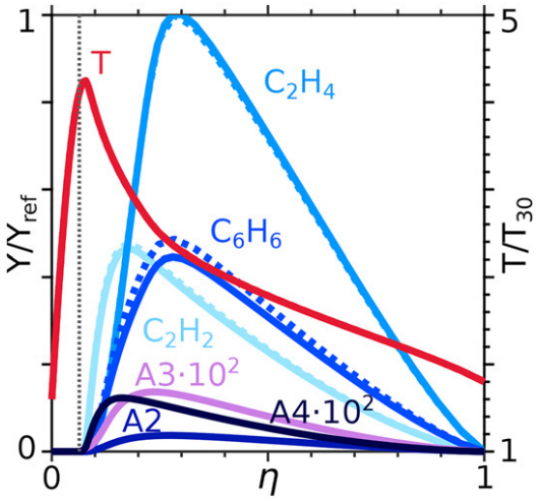

Figure 5.2: Change in the concentration of major species with the addition of the PAH pathways from KM2 to HyChem Jet-A reaction mechanism [15]

5.2. EFFECT OF PRESSURE AND EQUIVALENCE RATIO ON SOOT FORMATION

This section discusses the effect of pressure and equivalence ratio on soot formation and the behavior of the model. The combustion parameters assessed in this study are shown in Table 5.1

Table 5.1: Combustion parameters assessed for the effect of pressure on soot formation

Parameters assessed	Parameter Range
Equivalence Ratio	1-2.5
Reactor Pressure	1,5,10,20 atm
Reactor Residence Time	10 ms

The soot mass density and number density for varying equivalence ratio and pressure at $\tau = 10$ms is shown in Figure 5.3. For the assessed conditions, both soot mass and soot number density show similar behaviour with increasing pressure and equivalence ratio. With increasing equivalence ratio, the soot mass and number density for all pressures increase. Especially after $\phi = 2$, the increase rate of both mass and number density starts to increase and then starts to reach a plateau after $\phi = 2.2$. As the equivalence ratio is increased and mixture becomes richer, the amount of incomplete combustion products increases as well. As PAH precursors are mostly incomplete combustion products, with an increase in PAH precursor production PAHs and soot particles are also going to increasing with increasing equivalence ratio. The progress of both main PAH precursors and PAH molecules with increasing equivalence ratio for 10atm pressure are shown in Figure [**?**]

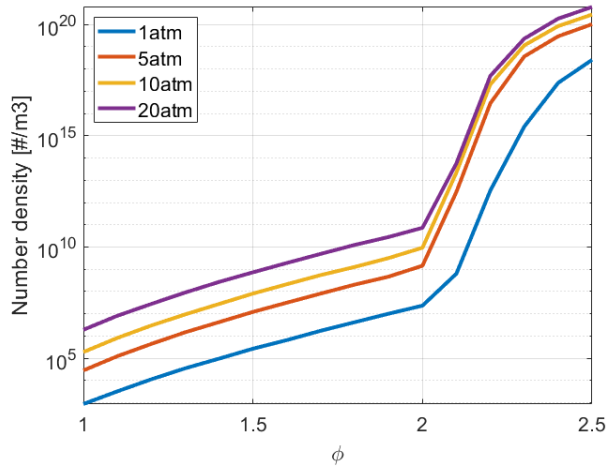

(a) Soot number density

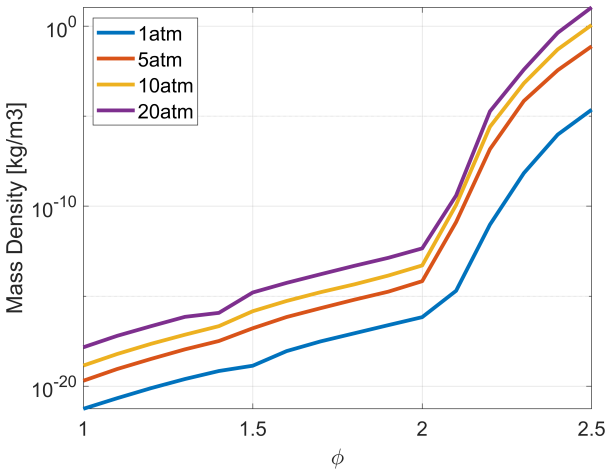

(b) Soot mass density

Figure 5.3: Soot number density and mass density for varying reactor pressures

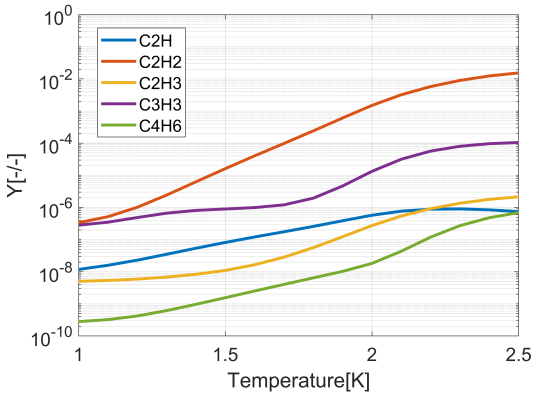

(a) Progress of main PAH precursor species concentration for varying equivalence ratio at P=10atm

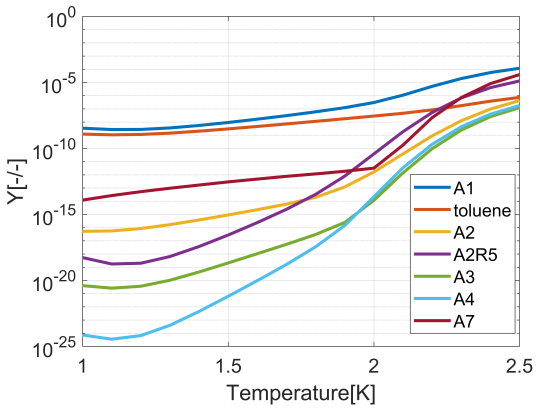

(b) Soot mass density

Figure 5.4: Progress of main PAH species concentration for varying equivalence ratio at P=10atm

The soot mass density and number density seems to increases with increasing pressure. However, the increase rate of soot mass and number density seems to decrease as the pressure is increased. Pressure has two main effects that are attributed to the soot formation. The first one is the increase in density with the increase in pressure. The increase in density increases the amount of soot precursors available. The increase in soot precursors will increase the amount of nucleated particles and the amount of species available that contributes to soot surface growth. Also, the increase in the amount of young soot particles will also increase the coagulation rate and agglomeration rate which will further increase soot formation. The second effect is the increase in reaction time with increasing pressure. The increased time scale allows the soot growth mechanisms,which are inherently slow, to reach completion and form soot particles.[80] Since the residence time is kept constant in this study, the consequences of first attribution is applicable to our study, which is supported by the gas phase densities calculated for the assessed parameters and shown in Figure 5.5 and the calculated species that are contributing to soot mass growth shown in Figure 5.6. With increasing pressure, the reactions taking place reaches further completion. With this completion, the amount of oxidizers,such as O2 and OH, decreases and the amount fuel dissociation products, such as acetylene and other smaller hydrocarbons that act as the precursor to PAH molecules increase. The increase in availability of these species also increase PAH concentration and ultimately soot particles increase. In consequence, the PAH amounts also increase with increasing pressure.

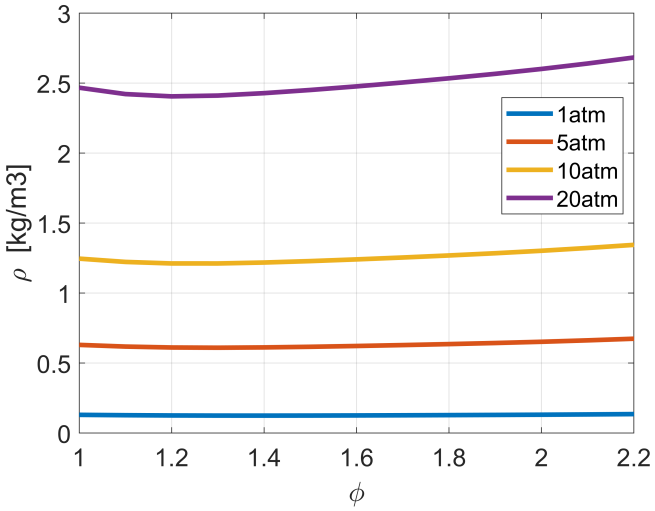

Figure 5.5: Density of the gas phase for varying pressure and equivalence ratios

The effect of pressure and equivalence ratio on soot formation can be further commented by investigating the contributions of the mechanisms assumed in the soot model. The mechanisms responsible for the soot mass growth for all pressure values are shown in Figure 5.6. The mechanisms responsible for soot mass growth shows the same behavior across all the pressure values investigated in this study. For equivalence ratios lower than 1.5, oxidation by oxygen is the dominant mechanisms to the mass growth. Due to the oxidation being the dominant mechanism, the soot formation is mostly inhibited up to $\phi = 1.5$ and starts to increase as acetylene addition and nucleation overcome oxidation. This behavior is expected as the mixture becomes richer, the oxygen concentration decreases and species that are precursor to PAH and soot formation increase in concentration and contribute to the soot formation more. This competition seems to be the reason for the increased rate of soot mass increase with increasing equivalence ratio. In the cases assessed, the PAH condensation always contribute less to the soot mass compared to both nucleation and acetylene addition. However, as the equivalence ratio increases, the magnitude of PAH condensation increases more rapidly than both nucleation and HACA growth. This behaviour suggests that if the equivalence ratio is increased further, the main contributer to the soot mass is going to be PAH condensation.

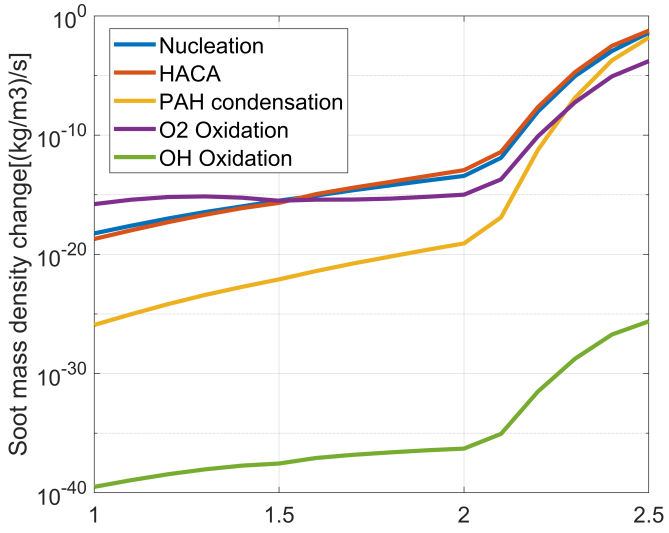

(a) 1 atm

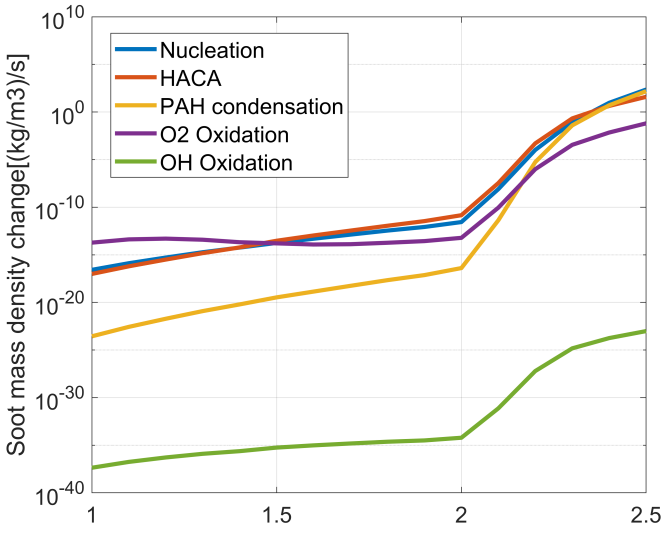

(b) 5 atm

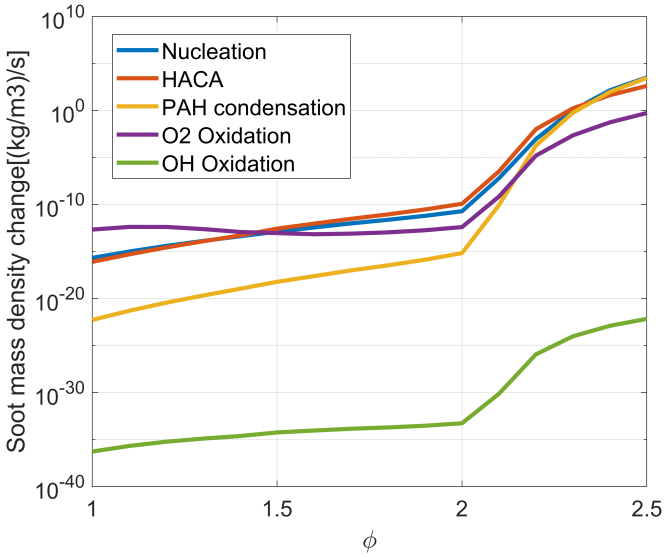

(c) 10 atm

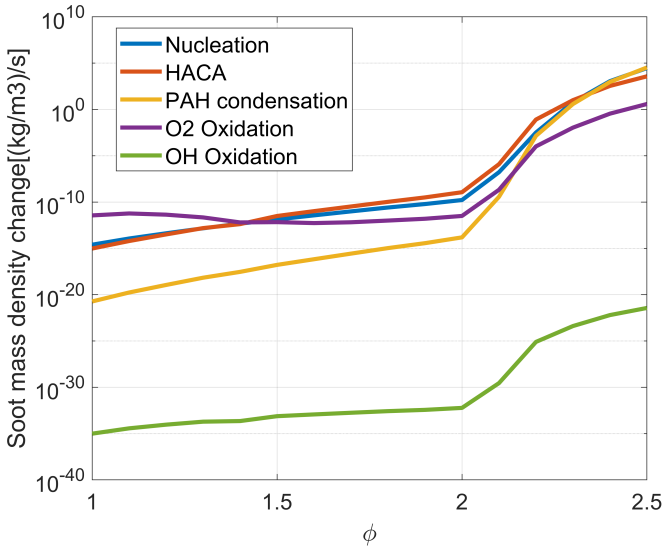

(d) 20 atm

Figure 5.6: Soot growth mechanisms for increasing pressure

5.3. EFFECT OF TEMPERATURE ON SOOT FORMATION

This section discusses the study made to investigate the effect of temperature on soot formation using the detailed soot model developed. The parameters investigated in this study are listed in Table 5.2

Table 5.2: Combustion parameters assessed for the effect of temperature on soot formation

Parameters assessed	Parameter range
Temperature (K)	1500-2500
ϕ	2
Pressure (atm)	10
Residence Time (ms)	10

The soot mass number density and the soot mass density studied for the parameters given in Table 5.2 are shown in Figure 5.7 . Both number density and mass density show a similar behaviour with increasing temperature. Both soot parameters increase exponentially as temperature increases up to 1800K and then decreases exponentially again after the peak values.

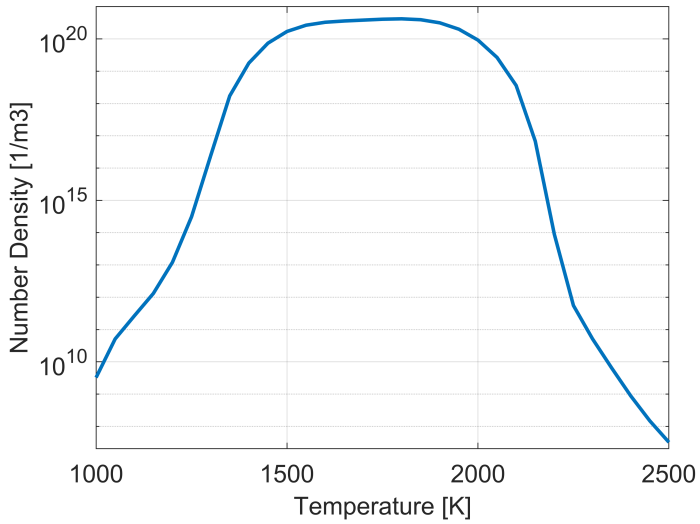

(a) Soot number density

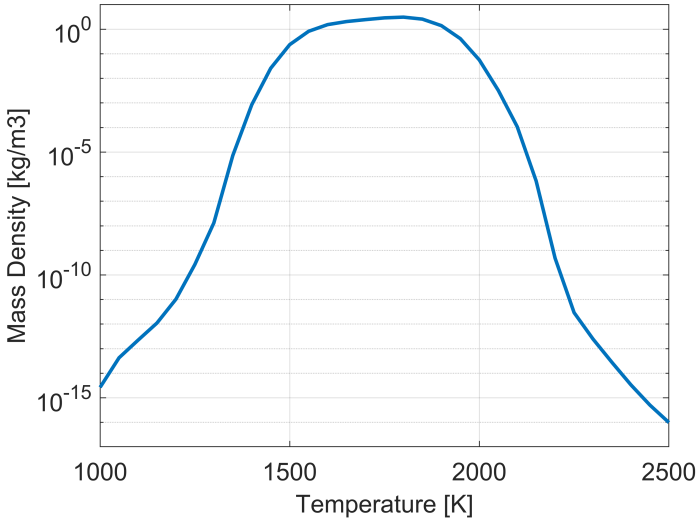

(b) Soot mass density

Figure 5.7: Soot number density and mass density for varying reactor temperature

The bell like curve achieved for the conditions evaluated show behaviour similar to previous studies done to investigate the effect of soot with temperature. The studies done concluded that the effect of temperature are two fold. The first is the availability of precursors needed for PAH and soot formation. At lower temperatures, the radicalic precursors like C2H3 or C3H3 does not form. With the increase in temperature, the formation rate of these radicalic precursors, and ultimately the formation rate of PAH molecules and soot particles increase. On the other hand, after a certain temperature is exceeded, the precursors that form the soot particles start to pyrolize and oxidize which inhibits the formation of soot particles [4]. This behavior is captured by the modeling study conducted as well. On Figure 5.8, the progress of some of the important precursors for benzene formation and some of the main PAH species with increasing temperature at P = 10 atm and $\phi = 2.0$ is shown. As seen in the Figure 5.8a, the concentration C2H, C2H2, C3H3 and C2H3 initially increase with increasing temperature, reach a plateau and then start to decrease with increasing temperature. The availability of the benzene precursor species can be seen on the formation of PAHs as well. The Figure 5.8b shows the progress of some of the main aromatic species for the assessed conditions. Smaller PAH species like benzene(A1), toluene(C7H8) and napthalene(A2) show a continuously decreasing behavior with increasing temperature. The concentration of bigger PAH species, like pyrene(A4) or coronene(A7) on the other initially increase with increasing temperature, reach a plateau and then starts decreasing with increasing temperature.

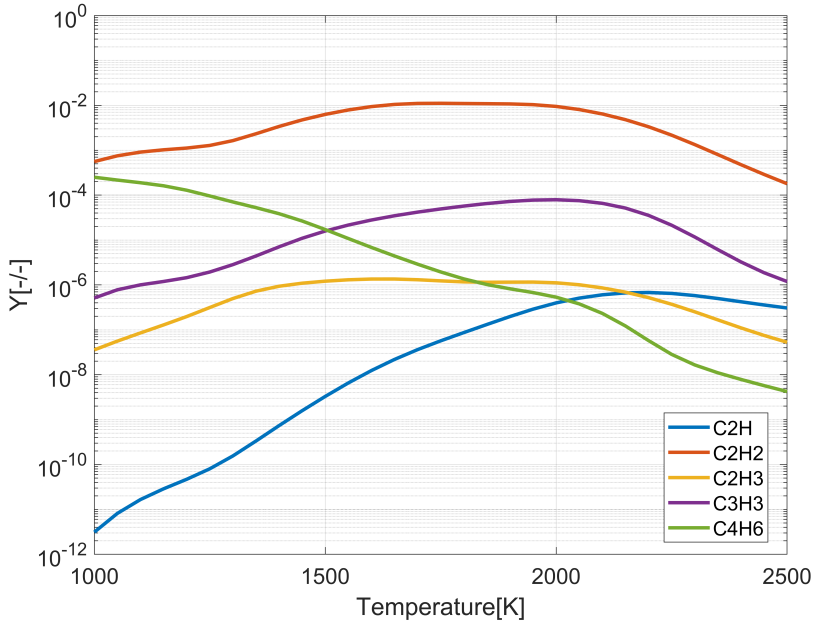

(a) Progress of main benzene precursors

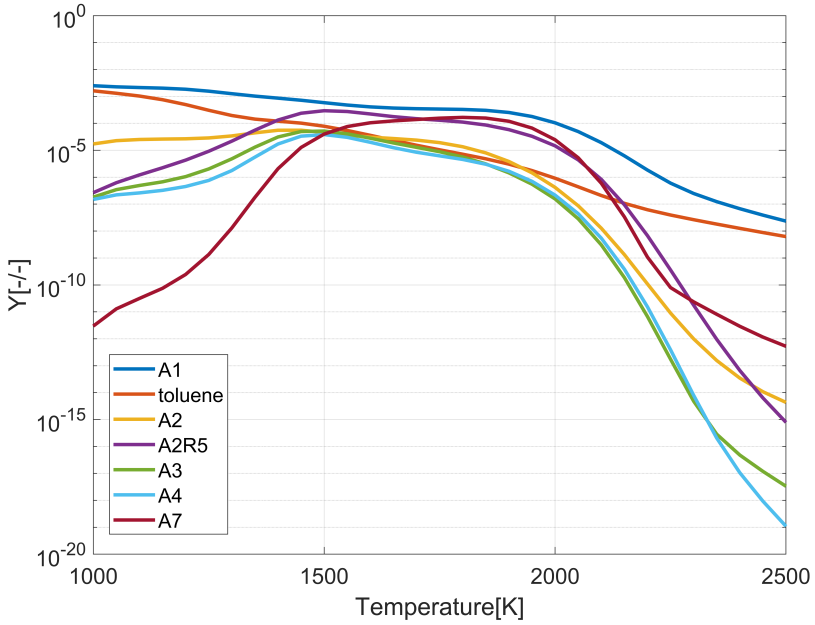

(b) Progress of main PAH species

Figure 5.8: Concentration of benzene precursor and main PAH species for temperature range 1000K-2500K for ϕ = 2.0 and P = 10atm

The behavior of the soot formation can be further investigated with the contribution of different soot mechanisms included in the soot model. The contribution of nucleation, acetylene addition(HACA), PAH condensation, O2 and OH oxidation for the investigated conditions are shown in Figure 5.9. From the Figure, it can be seen that the mechanisms also show a bell like curve. Initially, The main mass addition mechanism is nucleation, which progresses head to head with oxidation. After 1400K, oxidation rate exceeds nucleation but at the same time both HACA and PAH condensation exceed the amount of oxidation, PAH condensation becoming the main contributor to soot mass. After 2100K, the contribution of PAH condensation decreases faster than other mechanisms which let HACA the main soot mass contributor.

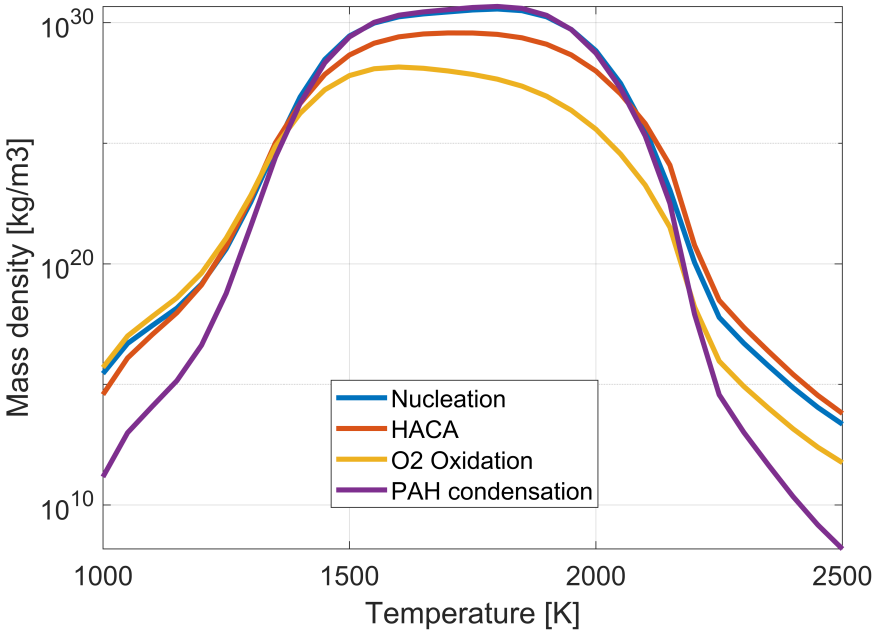

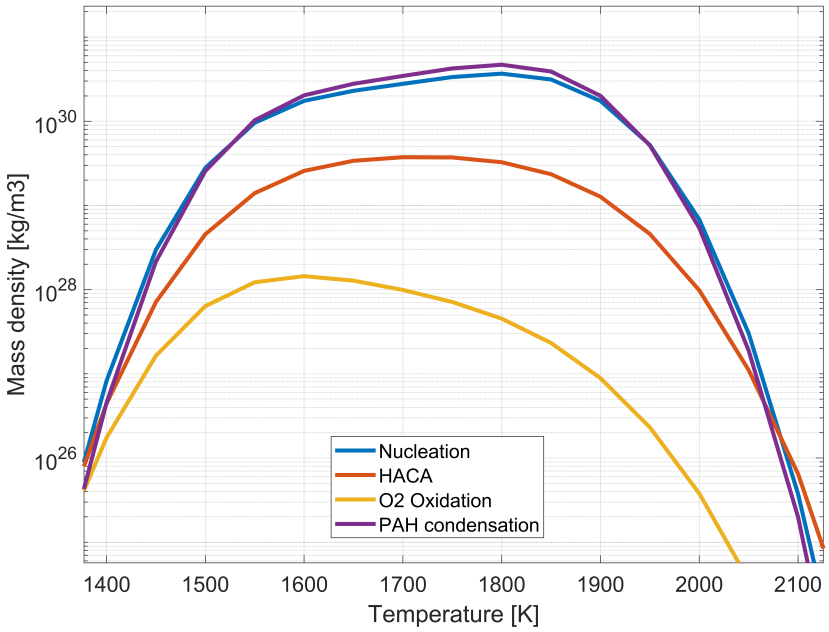

Figure 5.9: Contribution of soot mechanisms on soot mass density at 1000K-2500K for ϕ = 2.0 and P = 10atm

6

EMISSION MODELING FOR RQL COMBUSTOR

This chapter will describes the assessment of the soot emission modeling for an aero-engine with RQL type combustion chamber. The chapter explains the methodology on the construction of the CRN used and how the air distribution among reactors are done. The emission results for the LTO thrust settings are presented based on the air distribution found and the found results are assessed.

For the application of the soot model developed and validated in the previous chapters, the combustion chamber of General Electric(GE) CF6-80C2 engine is chosen. The CF6-80C2 is a high bypass turbofan engine first developed in the 1970s by General Electric. Over the years variants of the basic design were developed. The CF6-80C2 variant is currently used on aircrafts such as the Airbus A300 and Boeing 747, 767. The engine has a bypass ratio of 5:1. The overall pressure ratio is 30.08 and the engine has a rated output of 249 kN. It has an RQL based single annular combustor. The general schematic for GE CF6-80C2 is given in Figure 6.1

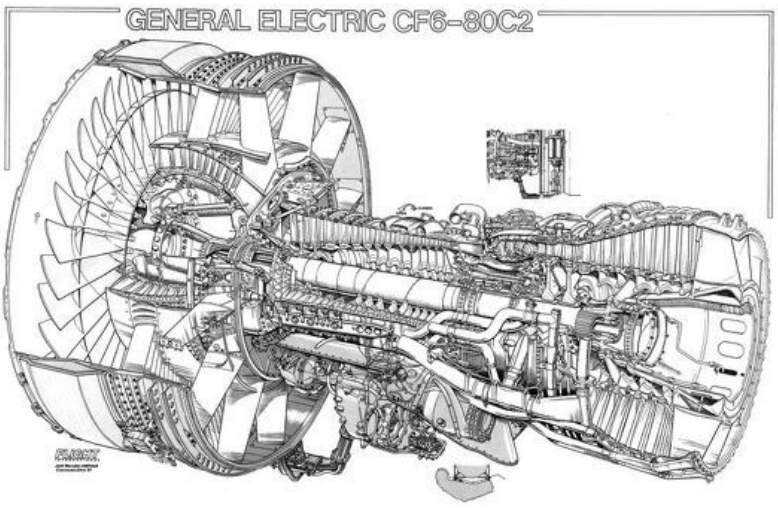

Figure 6.1: Cutaway of CF6-80 engine

6.1. MODELING APPROACH

6.1.1. ENGINE CYCLE PARAMETERS

The engine cycle parameters are adapted from the work of Telidevara[81]. Telidevara obtained the cycle parameters for the GE CF6-80C2 engine by using Gas Turbine Simulation Program(GSP), a gas turbine simulation program. The engine cycle parameters were obtained for the four thrust setting of the Landing Take-off (LTO) cycle. The engine cycle parameters obtained for the LTO thrust settings and used in this thesis are listed in Table 6.1.

Table 6.1: GE CF6-80 Engine cycle parameters

Thrust Level	Operating condition	[K]	P_{T_3} [bar]	$\dot{m}_{air_3}$ [kg/s]	$\dot{m}_{fuel_3}$ [kg/s]	ϕ_{overall}
100% FN	Takeoff	796.56	30.48	124.1	2.29	0.27
85% FN	Climbout	768.54	26.42	109.97	1.91	0.26
30% FN	Approach	626.44	12.14	58.06	0.69	0.18
7% FN	Idle	508.71	5.88	33.05	0.24	0.11

T_{T_3} is the total temperature of the inlet flow to the combustion chamber, P_{T_3} is the total pressure of the inlet flow to the combustion chamber, $\dot{m}_{air_3}$ is the total incoming air mass flow rate that is partitioned in the combustion chamber, $\dot{m}_{fuel_3}$ is the mass flow rate of the fuel to the combustion chamber, and ϕ_{overall} is the final equivalence ratio of the gas phase at the end of the combustion chamber.

6.1.2. REACTOR NETWORK

In order to model the soot emissions of the GE CF6-80C2 aero engine, a CRN arrangement more detailed than the previous CRNs used for the validation cases and the parametric study was required. Based on the structure and the operating conditions of the RQL combustion chamber, the CRN structure in Figure 6.2 is used to model the emissions of the aero engine.

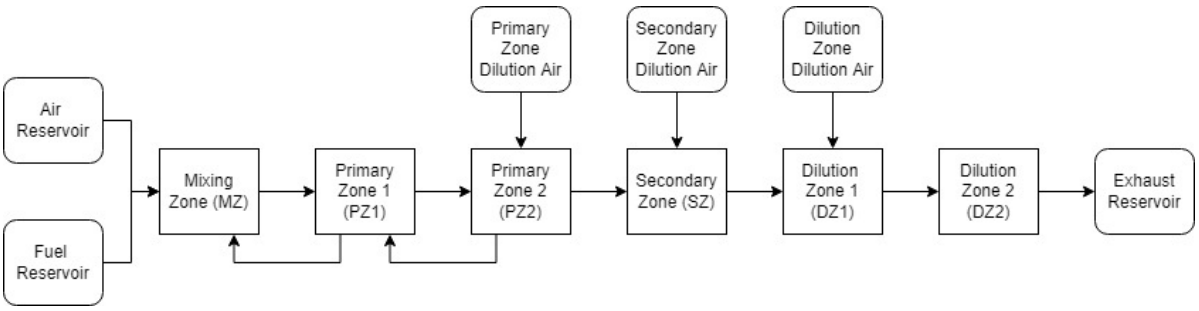

Figure 6.2: Reactor network to used to model the combustion chamber of GE CF6-80C2 engine

The combustion chamber is represented with 6 ideal gas reactors. The division of the reactors are based on the geometry of the combustion chamber and the location of the dilution air introduced to the combustion chamber, which is explained in detail by Shakariyants[82]. The first reactor represents the mixing zone(MZ) of the combustor and assumed to only promote mixing of the inlet air and fuel flow, and assumed chemically inert. The primary zone is represented with two reactors, the first one named primary zone 1(PZ1) and the second one is named primary zone 2 (PZ2) where the the dilution flow to the primary zone is introduced at. The secondary zone (SZ) of the combustor is represented with a single reactor and the second dilution air flow is introduced to this reactor. Lastly, the dilution zone of the combustor is represented with two reactors where the third and last dilution air is introduced to the dilution zone 1(DZ1) reactor followed by dilution zone 2(DZ2) reactor. In order to simulate the effect of recirculation, 15% of the primary zone 2 reactor mass flow is fed back to primary zone 1 reactor and 15% of the primary zone 1 mass flow reactor is fed into mixing zone reactor.

The inlet air flow and fuel flow is introduced to the reactor network with reservoirs. The whole fuel flow is fed into the mixing zone reactor. The air flow, on the other, is distributed among four reservoirs, one for the head of the combustion chamber, three for the dilution air introduced to the primary zone, secondary zone and dilution zone through the annulus flow. The distribution of the air flow is performed by assigning an

overall equivalence ratio for the reactors and split the air accordingly. The calculation of the air flow is done with the following equations:

$$\phi_{MZ} = \frac{\dot{m}_f}{\dot{m}_{aMZ}} \Big/ \left(\frac{\dot{m}_f}{\dot{m}_a}\right)_{st} \tag{6.1}$$

$$\phi_{MZ} = \phi_{PZ1} \tag{6.2}$$

$$\phi_{PZ2} = \frac{\dot{m}_f}{\dot{m}_{aMZ} + \dot{m}_{aPZ2}} \Big/ \left(\frac{\dot{m}_f}{\dot{m}_a}\right)_{st} \tag{6.3}$$

$$\phi_{PZ2} = \frac{\dot{m}_f}{\dot{m}_{aMZ} + \dot{m}_{aPZ2} + \dot{m}_{aSZ}} \Big/ \left(\frac{\dot{m}_f}{\dot{m}_a}\right)_{st} \tag{6.4}$$

$$\dot{m}_{aDZ1} = \dot{m}_{aTOTAL} - (\dot{m}_{aMZ} + \dot{m}_{aPZ2} + \dot{m}_{aSZ}) \tag{6.5}$$

The terms $\dot{m}_{aMZ}$, $\dot{m}_{aPZ2}$, $\dot{m}_{aSZ}$, and $\dot{m}_{aDZ1}$ is used to refer to the air mass flow rate added to the reactors mixing zone, primary zone 2, secondary zone, and dilution zone 1 respectively through the reservoirs shown in Figure 6.2. The subscripts f and a are used to refer to fuel and air.

The equivalence ratio assigned to the reactors are calculated by using an optimization scheme in MATLAB. To calibrate the equivalence ratios and match the model's NOx and CO emissions with the emission data from ICAO databank, Patternsearch feature of MATLAB's Global Optimization Toolbox is used. Patternsearch method uses gradient free methods to calculate the objective function, which is suitable for this case. The objective function written for the CRN has large gradients and many local minima due to the complex relationships present in chemical reactions included in the employed reaction mechanism. Due to this behavior of the objective function, the use of a global optimizer is deemed appropriate. The objective function used for the optimization is

$$\delta_{NOxCO} = \left(\frac{EINOx_{model} - EINOx_{ICAO}}{EINOx_{ICAO}}\right)^2 + \left(\frac{EICO_{model} - EICO_{ICAO}}{EICO_{ICAO}}\right)^2 \tag{6.6}$$

where δ_{NOxCO} is the outcome of the objective function that is minimized and EINOx and EICO are the emission index values from the model and the ICAO databank, with subscripts model and ICAO in order.

The reaction mechanism used to represent Jet-A1 fuel for the CRN calculations is the reaction mechanism mentioned in Section 5.1.1.

6.1.3. REACTOR VOLUMES AND AREAS

The volumes used for the reactor network are adapted from Telidevara [81]. Telidevara obtained the reactor volumes with AeroComb [82], a toolbox developed at TU Delft that calculates combustor geometries based on the given input conditions and geometric parameters. For the generation of the combustor geometry, parameters from take-off condition are used.

Table 6.2: Reactor Volumes and Cross Sectional Areas used in the RQL CRN

Reactor Zone	Reactor Volume [m^3]	Reactor Area [m^2]
Mixing Zone	0.00195	0.082
Primary Zone 1	0.0152	0.302
Primary Zone 2	0.0042	0.302
Secondary Zone	0.0176	0.302
Dilution Zone 1	0.0186	0.302
Dilution Zone 2	0.0112	0.182

6.2. RESULTS

6.2.1. AIR DISTRIBUTION

The reactor equivalence ratios found by the optimization scheme used are shown in Table 6.3. The model is able to replicate the shift in equivalence ratio during the addition of the initial dilution air. As mentioned in Section 2.5, RQL combustors introduce the air in the primary zone in order to avoid the peak temperatures at stoichiometric conditions and avoid peak NOx formation. In all power settings, the found air distribution shifts the rich equivalence ratio at PZ1 to a lean equivalence ratio at PZ2. With the further addition of air in the downstream of the combustion chamber, the overall equivalence ratios per zone drops further to the value at dilution zone. Apart from Idle condition, the overall equivalence ratios of the reactors seems to increases with increasing power setting. In Idle power setting, the equivalence ratios at PZ1 is richer compared to Approach conditions. Also, the equivalence ratios from PZ2 to SZ drops much rapidly in Idle thrust compared to the other power settings in order to match the emissions from ICAO databank, which will be discussed later.

Table 6.3: The air flow distribution for the LTO power settings

Power Setting	MZ	PZ1	PZ2	SZ	DZ1	DZ2
Idle	1.42	1.42	0.71	0.23	0.11	0.11
Approach	1.24	1.24	0.77	0.50	0.18	0.18
Climb out	1.53	1.53	0.82	0.53	0.26	0.26
Take off	1.69	1.69	0.84	0.60	0.27	0.27

klThe air flow distribution corresponding to the equivalence ratios are shown in Table 6.4 and the percentage of the total air mass distribution per section is shown in Figure 6.3. For all the power settings, approximately half of the inlet air is distributed the among head of the combustion chamber, primary zone dilution air and secondary zone dilution air. The remaining half of the dilution air is injected into the dilution zone. This allocation of the inlet air among reactors seems reasonable since bulk of the air flow is injected into the dilution zone in order to stop the reactions happening and drop the temperature of the combustor flow to a point that is acceptable for the turbine section of the engine.

Table 6.4: Total mass flow allocated to each reactor for the LTO thrust settings

Thrust Setting	$\dot{m}_{MZ}$ (kg/s)	$\dot{m}_{PZ1}$ (kg/s)	$\dot{m}_{PZ2}$ (kg/s)	$\dot{m}_{SZ}$ (kg/s)	$\dot{m}_{DZ1}$ (kg/s)	$\dot{m}_{DZ1}$ (kg/s)
Idle	2.74	2.74	5.23	15.68	33.31	33.31
Approach	8.89	8.89	13.82	21.21	58.75	58.75
Climb-out	20.26	20.26	36.36	54.77	111.88	111.88
Tale-off	21.88	21.88	42.18	58.96	126.39	126.39

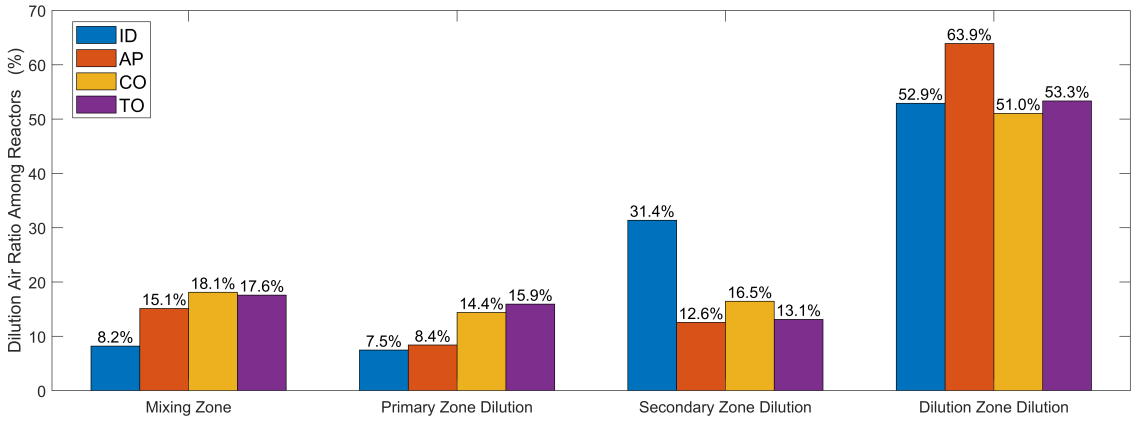

Figure 6.3: Air mass distribution for LTO power settings

6.2.2. TEMPERATURE, PRESSURE AND RESIDENCE TIME OF THE REACTORS

TEMPERATURE

Based on the air distribution found for each power setting, the temperatures calculated at each reactor for the LTO thrust settings are shown in Figure 6.4. The general trend for the progress of temperature for each zone, apart from PZ1 temperatures, shows a similar trend. The addition of dilution air decreases the temperature attained in the PZ2 reactor until DZ2, where the temperature stays almost constant after DZ1 due to the addition of the bulk of the dilution air which virtually pauses reactions in the dilution zone. The behavior of the temperature change from PZ1 to PZ2 can be explained by comparing their respective reactor equivalence ratios. The change in adiabatic flame temperature according to equivalence ratio is shown in Figure 6.5. As seen in the Figure, the adiabatic flame temperature reaches its peak value somewhere slightly richer than stoichiometric equivalence ratio. For take-off and climb-out conditions, the PZ1 equivalence ratio is farther to the stoichiometric conditions than PZ2 equivalence ratio, meaning the amount of total reactants that contribute to the heat release at PZ2 is more than PZ1. Due to this, the heat released at PZ2 is more for the take-off and climb-out which causes PZ2 temperature to be higher than PZ1. For approach and idle conditions, the opposite scenario applies.

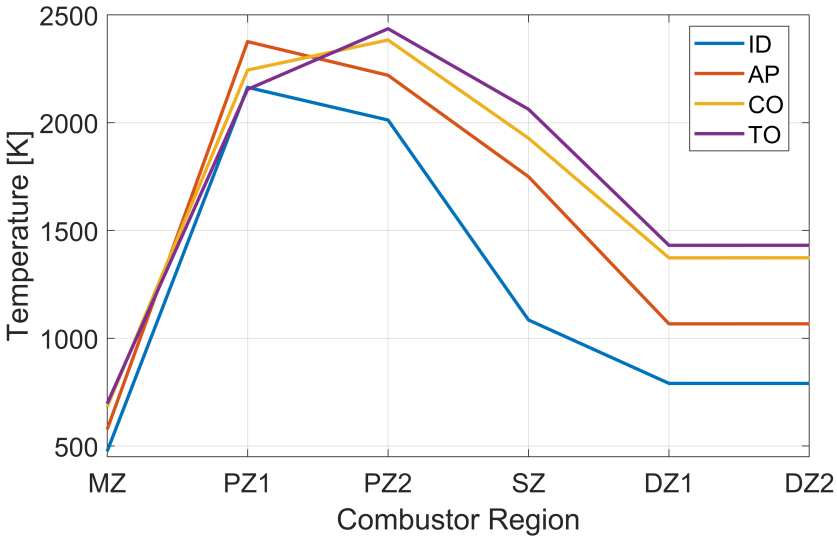

Figure 6.4: Temperature of each combustor zone for LTO power settings

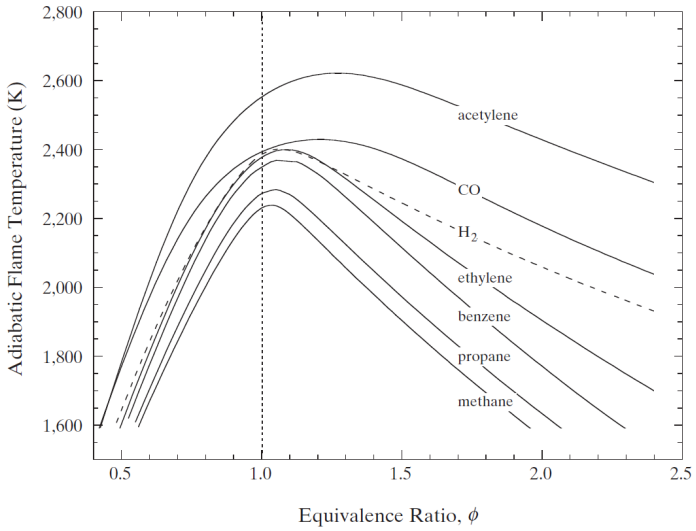

Figure 6.5: Adiabatic flame temperature as a function of fuel equivalence ratio [16]

RESIDENCE TIME

The progress of residence time along the combustion chamber for both cumulative manner and individual reactors are shown in Figure 6.6. Apart from take-off conditions, as the power is lowered, the overall residence time spend inside the combustion chamber increases. As the power is lowered, the overall pressure and the mass flow rate through the reactors decrease. The decrease of both overall pressure,consequently density, and the mass flow rates with decreasing power increases the total residence time. The residence time for the take-off condition doesn't fit the usual behavior of the of the residence time. Even tough the total take-off residence time isn't bigger than approach or idle conditions, it is still higher than climb-out conditions. Main reason for this behavior can be seen from Figure 6.6b. As seen from Figure 6.6b, the residence time at reactor PZ1 for take-off is larger than climb-out. For the other reactors downstream, the individual residence times seems to be more or less the same. At take-off, even tough the operating pressure and gas phase density at PZ1 is higher at take-off than climb out, the higher ratio of dilution air admitted to the mixing zone at climb-out conditions caused the velocity of the flow at PZ1 for climb-out to be higher than take-off, hence the lower residence time in PZ1 at climb-out conditions.

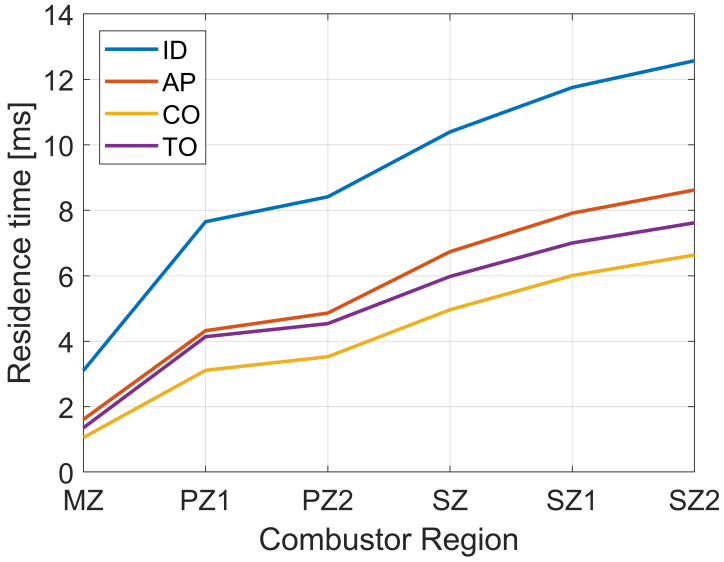

(a) Cumulative residence time of each combustor zone for LTO power settings

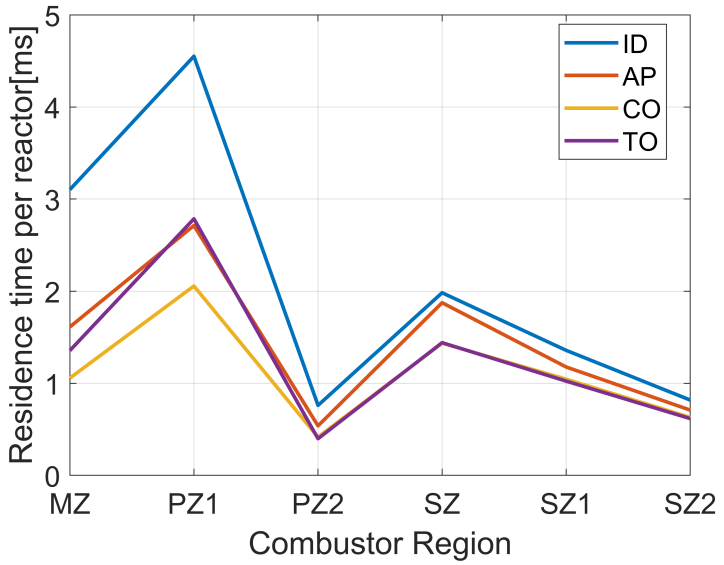

(b) Individual residence time of each combustor zone for LTO power settings

Figure 6.6: Progress of residence time along the RQL-CRN reactors

6.2.3. NOx AND CO EMISSIONS

This sections presents the NOx and CO emissions calculated with the CRN based on the optimization scheme used to tune the dilution air distribution among reactors for each LTO thrust setting. This section will include comparison of the modelling results with the ICAO databank results along with the progress of NOx and CO emissions inside the combustion chamber.

The progress of NOx emissions along the combustion chamber zones for each power setting are shown in Figure 6.7. Based on the modeling results, the main trend of the NOx emissions is at PZ2, the NOx emissions reach its peak value compared to other reactors at the respective power setting, and then progressively decrease until DZ1, where the addition of the air basically freezes the reactions for the formation and consumption of NO. With the addition of the dilution air at the downstream of the primary zone and the drop in the temperature caused by the addition of dilution air is lowering the NOx formation. The amount of NOx emissions at every reactor increases with increasing power after PZ1. With the increase in power, the overall temperatures of the combustion chamber is increasing which in return seems to increase the level of NOx formation.

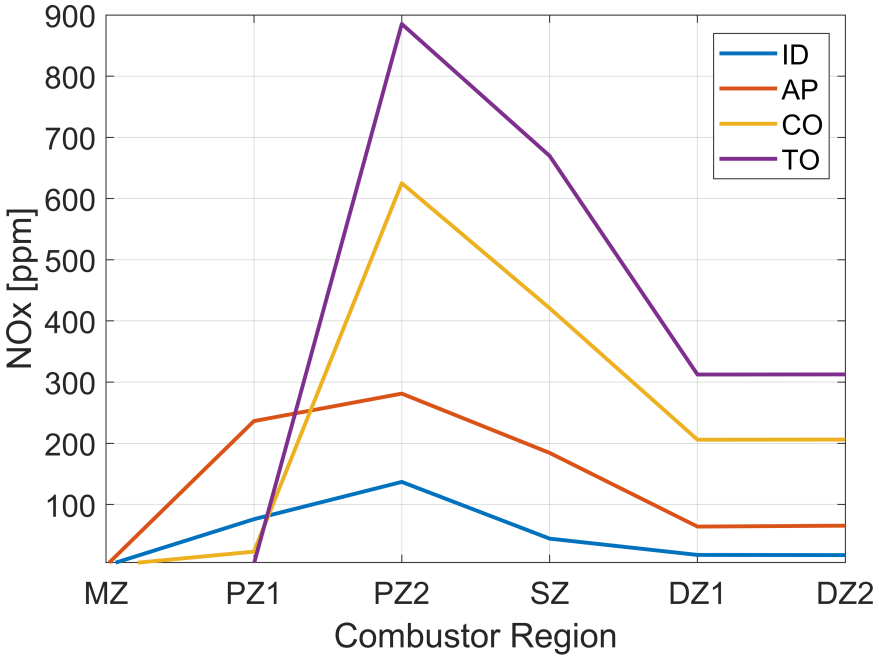

Figure 6.7: Progress of NOx emissions(in terms of mole fractions) along the combustion chamber zones

The progress of CO emissions along the combustion chamber zones for each power setting are shown in Figure 6.8. The CO is mostly formed in PZ1 where the gas phase is fuel rich and partial oxidation products of the fuel that form CO are more compared to the other zones. With the addition of rest of the dilution air at the downstream of the PZ1 reactor, the equivalence ratio is shifted to fuel lean conditions, which stops the formation of the incomplete combustion products that further form CO. With the addition of air and pause of CO formation, the formed CO molecules at the PZ1 starts to oxidizes along the downstream of the combustion chamber, until DZ2. It seems at DZ2, the addition of remaining dilution air pauses the reaction for CO formation and consumption happening at Idle and Approach conditions, but the temperatures at DZ2 for climb-out and take-off conditions seems to be high enough for the consumption of CO molecules to continue unlike the lower thrust setting conditions. The CO formed in the PZ1 seems to be parallel to the equivalence ratios of the PZ1 at different power settings. The CO formed in the PZ1 seems to increase with increasing PZ1 equivalence ratio. The highest CO formation happens at take-off, which has the richest equivalence ratio for the PZ1 reactor, followed by climb-out , which has the second richest PZ1 equivalence ratio, then followed by idle and approach. The consumption of the CO at the downstream of the PZ1 decreases with decreasing thrust due to the lower overall temperatures at lower thrust settings. As the temperatures are lowered, the oxidation of HCO to CO and the oxidation of CO to CO2 is lowered. Even tough the lower power settings provide more residence time, the increased residence time seems to be not contribute to CO's

oxidation into CO2.

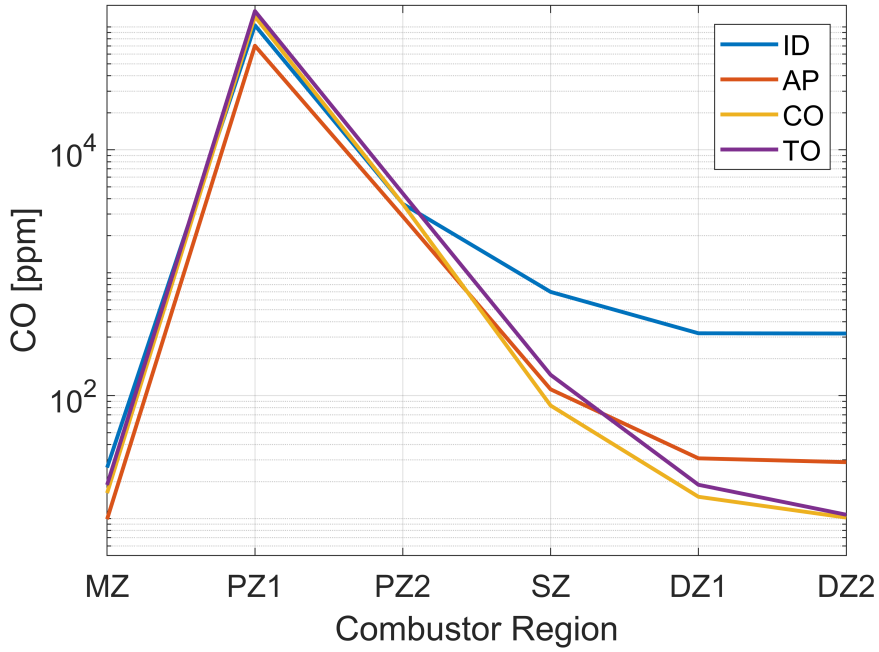

Figure 6.8: Progress of CO emissions(in terms of mole fractions) along the combustion chamber zones

Based on the dilution air distribution computed for each LTO thrust setting, the comparison of the modeling results and the ICAO databank results for NOx and CO emission index(g/kg-fuel) results are shown in Table 6.5. According to the ICAO databank, as the power is increased, NOx emissions increase and CO emissions decrease. Even tough CO emissions decrease with increasing power in general, it seems the CO emissions at climb-out conditions are lower than take-off conditions. When the modeling results and the ICAO databank results are compared, it can be concluded that the modeling results are able to capture the trend of both NOx and CO emissions with varying power while estimating the NOx and CO emissions for each power setting well below the deviations given for CO and NOx emissions, which are approximately stated to be ±5.56% for CO emissions and ±4.83% for NOx emissions. It can be concluded that the constructed CRN is able to estimate the CO and NOx emissions for LTO thrust setting for the engine with acceptable accuracy.

Table 6.5: Modeling Results for NOxEI and COEI

Thrust Setting	NOxEI Model (g/kg-fuel)	NOxEI ICAO (g/kg-fuel)	NOx Error (%)	COEI Model (g/kg-fuel)	COEI ICAO (g/kg-fuel)	CO Error (%)
Idle	3.81	3.73	2.07	43.01	43.22	0.49
Approach	8.84	8.83	0.12	2.37	2.37	0.03
Climb-out	21.33	21.26	0.31	0.55	0.55	0.64
Take-off	27.75	28.11	1.31	0.58	0.58	0.40

6.2.4. SOOT EMISSIONS

This sections shows the soot emissions calculated with the results of the CRN constructed for the RQL combustor. This section will include the progress of the soot emissions in terms of mass and number density along the reactors and the comparison of the modelling results with the ICAO databank results.

PROGRESS OF SOOT MASS AND NUMBER DENSITY IN THE CRN

The progress of the soot number density and soot mass density among the reactors used in the CRN for each LTO thrust setting is shown Figure 6.9. In accordance with the ICAO databank, soot number density and soot mass density are presented in terms of nvPMEInum and nvPMEImass respectively, where number density and mass density are normalized by the amount of fuel burned for each thrust setting. For all the power settings, the soot number density follows a similar trend along the combustion chamber. The soot number density attains its highest value at PZ1 where fuel rich burn is happening, and then decreases as the flow progresses through the downstream of the combustion chamber. However, the soot number density shows a peculiar behavior at SZ where the number density increases at SZ for all thrust settings apart from Idle. The reason for this behavior might be the increased residence time at SZ compared to PZ2 with the addition of the dilution air and the decrease in temperature, which might have lead the solver to calculate a higher number density of soot particles SZ. After the secondary zone, the number density continues to decrease albeit slightly after DZ1.

According to the model, the soot mass reaches its peak value at PZ1 for Idle and Approach conditions and reaches its peak at PZ2 for the higher thrust settings. For idle and approach, this behavior is expected since the soot is formed in PZ1 where the rich burn is happening and it is consumed after PZ1. The slight increase in the soot mass for climb-out and take-off conditions suggests that the increase in oxidation rate with addition of dilution air at PZ2 was not enough to start the consumption the soot mass at PZ2 as it did for the lower power settings. However, after the soot mass reaches its peak for all power settings,whether it is at PZ1 or PZ2, as further dilution air is introduced in the downstream, soot mass continuously decreases until DZ2, where it slightly increases for idle conditions and slightly decrease for the rest of the power settings.

The progress of the soot parameters show that the model is able to capture the general progress of both soot number density and soot mass density within zones of the combustion chamber. The kinks in the model, such as the sudden increase if number density at SZ or the mass density increase in DZ2, suggest that the number of reactors used in the downstream of the PZ1 might not provide enough information to explain the progress of the soot parameters with the change in axial length/increasing residence time. The flow downstream of the rich burn section/PZ1 might require further 'resolution' in axial direction. This resolution can be provided by using more PSRs in series or by using plug flow reactors to represent the secondary zone and the dilution zone.

It should be mentioned that the soot number density and mass density show similar progression along the combustion chamber based on the modeling results but the magnitudes of both number density and mass density for different power settings vary by quite a large margin. For both number density and soot mass density, the difference between the lowest and highest values are approximately 17 to 18 orders of magnitude, which is not realistic. The potential reasons for this discrepancy between the magnitudes of both soot number density and mass density for different thrust settings will be discussed in the next section.

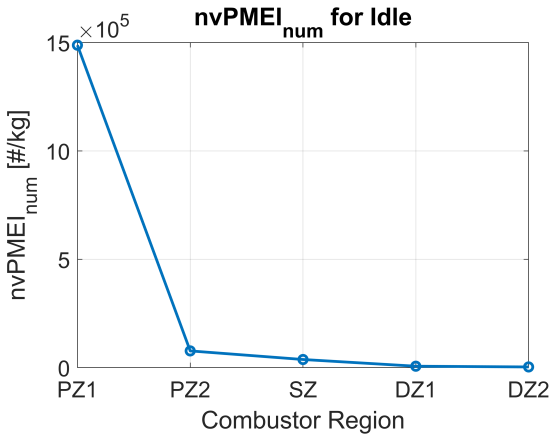

(a) Soot number density at each combustor zone for Idle

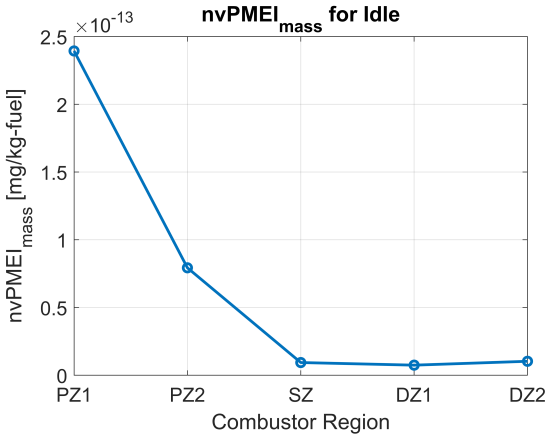

(b) Soot mass density at each combustor zone for Idle

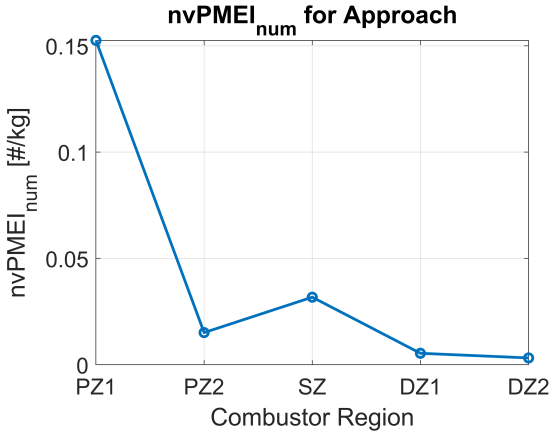

(c) Soot number density at each combustor zone for Approach

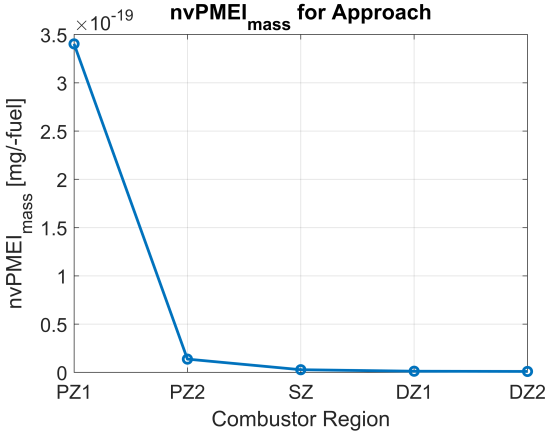

(d) Soot mass density at each combustor zone for Approach

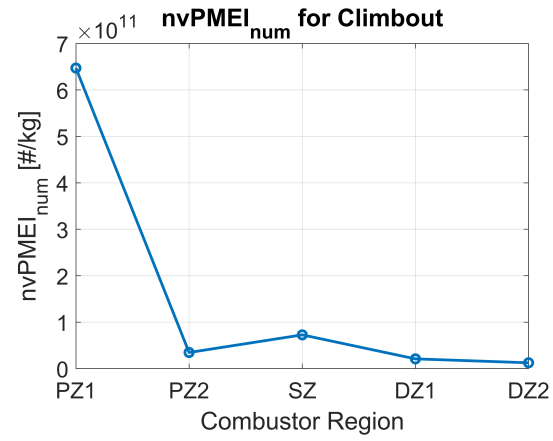

(e) Soot number density at each combustor zone for Climb-out

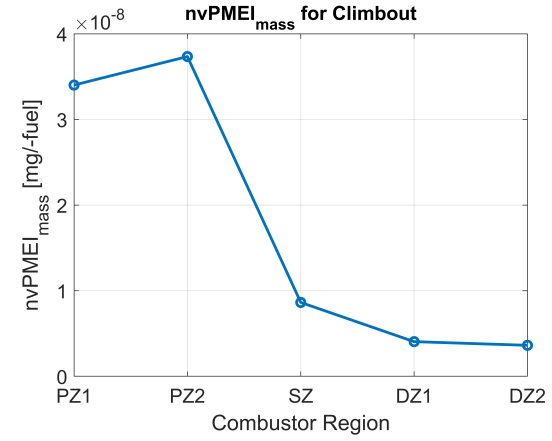

(f) Soot mass density at each combustor zone for Climb-out

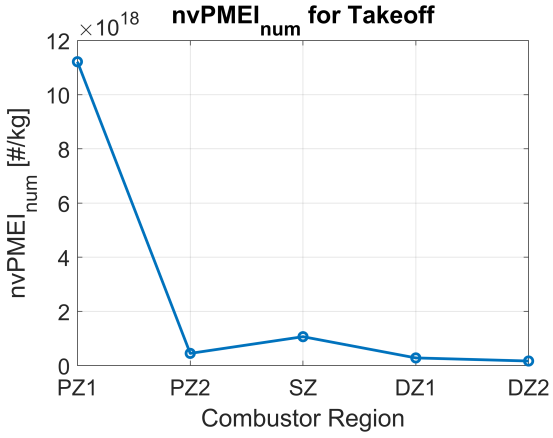

(g) Soot number density at each combustor zone for Take-off

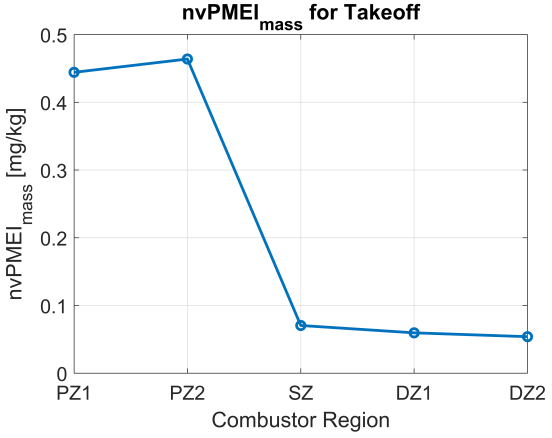

(h) Soot mass density at each combustor zone for Take-off

Figure 6.9: Progress of soot number density and soot mass density among CRN reactors for LTO thrust settings

nvPMEInum and nvPMEImass

Based on the dilution air distribution found for each LTO thrust setting, the soot emission results in terms of number density and mass density from the constructed CRN is shown in Table 6.6. Based on the ICAO databank, the mass density of the soot particles increase with increasing thrust setting. According to ICAO databank, the soot number density slightly decreases from Idle to Approach power setting, increase by an order of magnitude from approach to climb-out and slightly decrease from climb-out to take-off. When the modeling results and the ICAO databank results are compared, it can be seen that the model severely underestimates both number density and mass density of soot emissions for the Idle, Approach and Climb-out thrust settings. For the take-off conditions, the model underestimated the soot mass density by an order of magnitude. On the other hand, the model overestimated the number density of soot particles by an order of magnitude of 3.

Table 6.6: Modeling results for soot number density and soot mass density

nvPMEInum(#/kg-fuel)			nvPMEImass(mg/kg-fuel)		
Power Setting	ICAO	Model	Power Setting	ICAO	Model
Idle	6.54×10^{13}	5.36×10^{4}	Idle	1.2	1.03×10^{-14}
Approach	3.96×10^{13}	2.93×10^{2}	Approach	1.3	1.02×10^{-21}
Climb-out	2.39×10^{14}	1.33×10^{10}	Climb-out	18.3	3.61×10^{-9}
Take-off	2.36×10^{14}	1.33×10^{17}	Take-off	34.9	3.31

Based on the comparison of the modeling results and ICAO databank results for take-off conditions, certain comments about the performance of the model can be deduced. Firstly, the model is overestimating the soot number density by few orders of magnitude, which was also seen for the validation of the model against Marr's experimental results and was shown in Table 4.1. In the modeling approach, the number density of the soot particles are calculated based on the value of the zeroth moment as

$$N_{soot} = M_0 \tag{6.7}$$

and the zeroth moment is calculated by integrating the zeroth moment term for nucleation and coagulation

$$\frac{\mathrm{d}M_0}{\mathrm{d}t} = R_0 - G_0 \tag{6.8}$$

As the zeroth moment is mostly proportional with the nucleation term, the overestimation of the number density suggests the nucleation rate assumed by the model is overestimated since the number density is proportional with the nucleation term in the MOMIC equations as shown in Equation 6.8. The nucleation term for the MOMIC equations might overestimate the number density of the soot particles for few reasons. These reasons are

- Concentration of the soot precursor
- Overestimation of the collision frequency

The over-estimation of the concentration of the of the soot precursor is one of the potential reason for the overestimation of the soot number density. As the nucleation terms are proportional with the square of the number of precursor particles, the overestimation of the concentration of the soot precursor can cause the nucleation term to be overestimated. The concentration can be overestimated due to the selection of the soot precursor species or inherently overestimated based on the construction of the reaction mechanism used.The second reason for the overestimation of the nucleation term might be due to the collision frequency term used during the nucleation term. The collision frequency used in the nucleation term might assume a higher collision success for the PAH molecules to form initial PAH particles. This is likely the case as there are multiple examples in the literature that addresses the overestimation of the nucleation and propose methods to modify the nucleation terms. For example, Blanqaurt et al.[39] assume nucleation is initiated with the self collision of PAH molecules within the size range from napthalene to cyclodpenta[cd]pyrene and assign an additional collision coefficient to the nucleation term based on the size of the PAH molecule that collides. Another example of a correction factor was proposed by Wang et al.[83] where they assumed the PAH species responsible for the nucleation were ranging in size between pyrene to coronene and they assigned correction factors to the nucleation terms. They assigned the correction term because the initial collision efficiency

employed in their model was based on premixed ethylene flames but their current study is on counterflow diffusion flame, which exhibit different temperature ranges and chemical environment that alters the collision behavior of the PAH molecules.

The second comment that can be made based on the comparison between modeling results and the ICAO databank for take-off condition is the the model is underestimating the soot mass density by an order of magnitude. This behavior seems to stem from the underestimation of the soot surface growth terms. The underestimation of the surface growth terms can be substantiated by comparing the soot mass per particle ratio in the take-off conditions. The soot mass per number density ratio for the ICAO databank is 1.48×10^{-13}mg/particle and the ratio for the model is 2.49×10^{-17}mg/particle. The lower ratio found by the model means the surface growth term employed by the model is underestimating soot mass accumulated on soot particles. This underestimation might happen due to certain reasons. The first reason might be the mass growth terms used in the moment equations are assuming a much lower surface growth rate. This might stem from the selection of the soot precursor species assumed for PAH condensation. In the model, the soot precursor species are assumed to be pyrene and coronene. This selection was made in order to employ pyrene, which is a popular selection for the soot formation and coronene, a PAH molecule that is much more stable then pyrene under elevated temperature and pressure conditions. As mentioned before, there are no consensus on which PAH species act as the precursor to soot formation. If we give examples from mentioned literature, Blanquart et al.[39] assumes the species active on PAH condensation are varying in size from napthalene to cyclopenta[cd]pyrene PAHs used for nucleation. On the other hand, Wang et al.[83] is using PAHs varying between pyrene and coronene as the condensating PAH species. As the PAHs used among the literature are varying quite alot, the selection of PAH molecules that is suitable for the combustion conditions evaluated at RQL CRN might improve the the accuracy of the soot surface growth.

Another reason for the underestimation of the soot mass might be due to not including the effect of agglomeration. In agglomeration, spherical soot particles formed will stick to each other forming a necklace like structure. The agglomeration process also increases available surface are per particle which can promote further growth by surface reactions. The agglomeration mechanism usually take places after the flame and it increases the soot mass per particle while decreasing the number density of soot particles. In the literature, there are two examples of agglomeration models proposed to modify MOMIC equations. Frenklach [62] proposed that the agglomeration happens after particles reach a certain size, 25nm to 30nm. When the particle exceeds this limit, a new set of equations are added to present the agglomerated particles and solved along with the normal MOMIC equations. Balthasar et al.[77] proposed an additional agglomeration term to be solved with the MOMIC equations which modify the initial MOMIC terms with a coefficient. The addition of terms to model the agglomeration as mentioned in the previous examples can shift the modeling results closer to the actual soot emissions results.

For the rest of the power settings, unlike the take-off conditions, both number density and mass density of the soot emissions are severely underestimated, especially for climb-out and approach conditions. Based on the ICAO results, both soot number density and mass density are in the same order of magnitude for take-off - climb-out pair and approach - idle pair. Based on the results of the model, take-off soot emissions results are much bigger than climb-out results and idle soot emission results are much bigger than approach results. This behavior of the modeling results seems to be parallel with the equivalence ratio of the PZ1 reactor for the respective thrust setting. As shown in Table 6.3, the equivalence ratio of the PZ1 decreases as the power is lowered, apart from Idle which has a higher equivalence ratio than Approach. This relation between the PZ1 equivalence ratios are also reflected to the PAH formation and in parallel soot formation in PZ1. Figure 6.10 shows the calculated progress of benzene, napthalene, phenanthrene, pyrene, and coronene for the LTO thrust setting conditions. As seen in the figure, the aromatics are formed in PZ1, where the reacting mixture is rich, and then consumed along the downstream with the addition of dilution air. Also, among the thrust settings, PAH concentrations show great difference in terms of magnitude. Apart from the climb-out condition, all power settings show similar behavior along the combustion chamber but in different orders of magnitude. This shows the PAH formed in primary zone is highly sensitive to the equivalence ratio assumed for the PZ1 and the air distribution found based on the NOx and CO emission might not be sufficient to predict the PAH concentrations in the combustor.

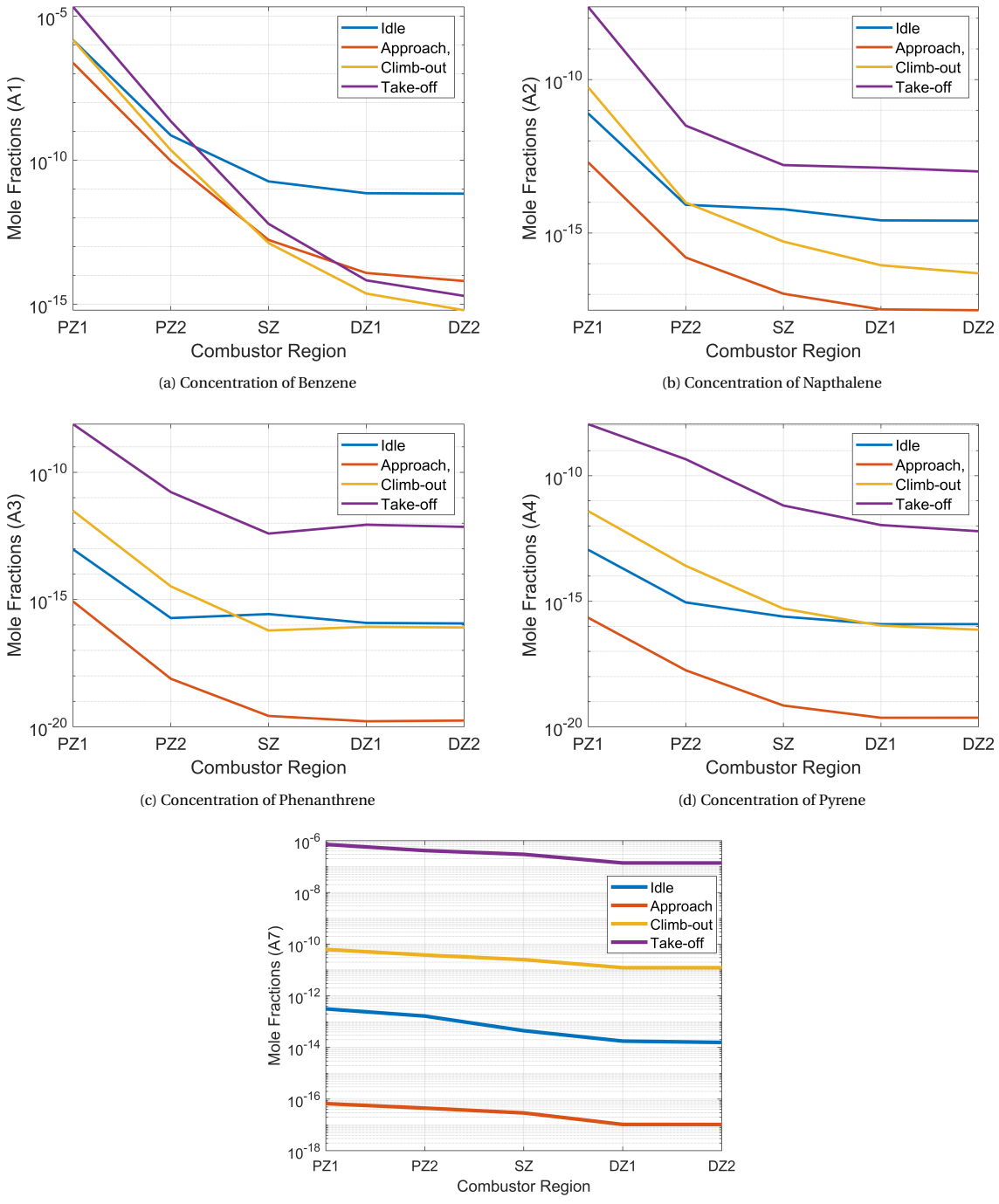

(a) Concentration of Benzene

(b) Concentration of Napthalene

(c) Concentration of Phenanthrene

(d) Concentration of Pyrene

(e) Concentration of Coronene

Figure 6.10: Progress of PAH species along CRN reactors for LTO thrust settings

The progress of the concentration of PAH precursor, C_2H_2 and C_3H_3 for the varying power settings are shown in Figure 6.11. Like the PAH molecules, the PAH precursor species also formed in PZ1 reactor and the magnitude of the PAH precursor species seems to be parallel with the equivalence ratios at different power settings where the higher the equivalence ratio, higher the PAH precursor formed in PZ1. Unlike the PAH species, their concentrations seems to be affected more by their consumption along the downstream of primary zone 1.

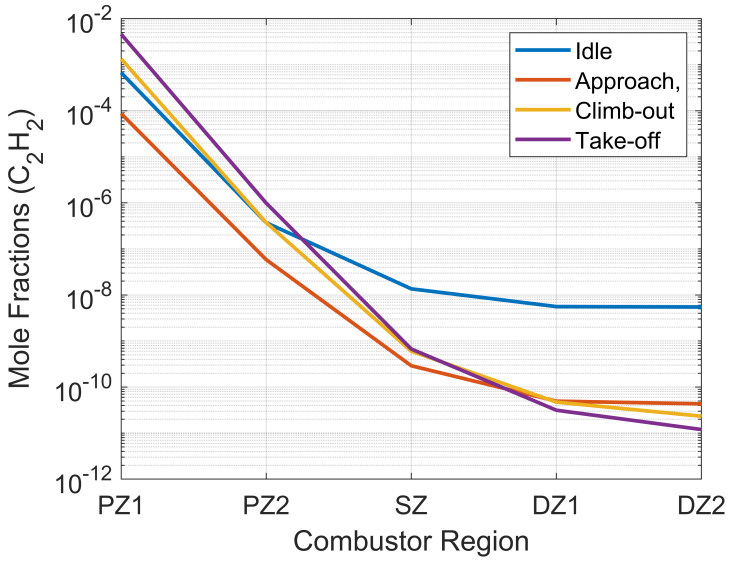

(a) Soot number density at each combustor zone for Idle

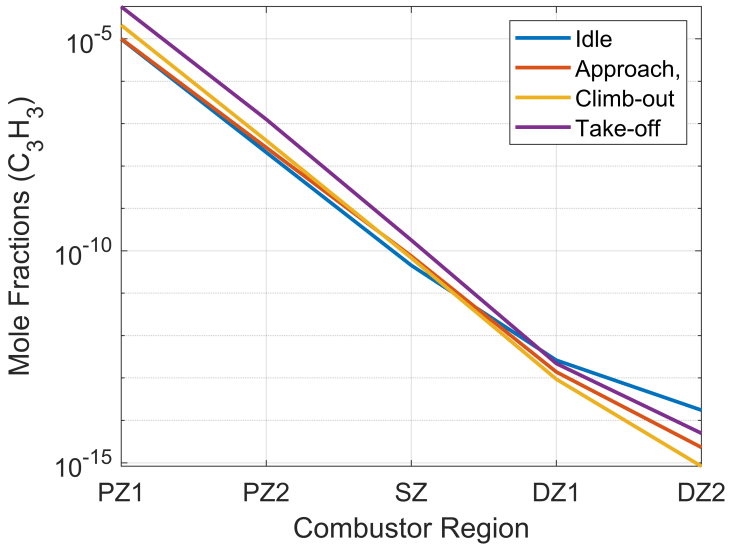

(b) Soot mass density at each combustor zone for Idle

Figure 6.11: Progress of C2H2 and C3h3 species along CRN reactors for LTO thrust settings

7

Conclusions and Recommendations

The increasing emission requirements at the aviation sector pushes equipment manufacturers to design their products with reduced emissions. In the case of aero engines used in aviation, the effects of emissions such as nitrogen oxides (NOx), carbon monoxide (CO), and unburnt hydrocarbon (UHC) are well understood and measures towards mitigation of these emissions are taken. In recent years, emission limitations for soot emissions are also introduced to the aviation sector. To abide the current emissions requirements, these requirements should be taken into consideration in every step of the design process of an aero engine, including the preliminary design process. One of the most effective ways to assess the emission levels of an aero engine is with the use of chemical reactor networks. In the literature, there are ample examples of the use on CRNs to model the NOx and CO emissions of various aero engines including aero engines with Rich Burn-Quick Quench-Lean Burn(RQL) type combustion chambers. On the other hand, the examples on literature about modeling soot emission for aero engine combustor using CRNs are really scarce. In order to address this knowledge gap, this thesis will answer the research question

How accurately can the soot emissions for an RQL type aero engine combustor predicted using chemical reactor networks in conjuction with a detailed soot model?

To assess the soot emissions for the RQL type combustion chamber, Method of Moments with Interpolative Closure(MOMIC), a detailed soot emission model is selected to be coupled with the CRN method. In this study, the species consumed by soot formation is assumed to be negligible. Based on this assumption, in the modeling efforts, firstly the CRN for the modeled case is constructed and solved and then the results necessary for the MOMIC equations are taken from the CRN models and fed into a stiff ODE solver which solves the MOMIC equations.

Two experimental cases that provided data on various species concentrations and soot emissions are modeled to validate the modeling method employed in this thesis. The first experimental case is Vaughn's [69] experiments for the ethylene/air combustion at a Jet Stirred Reactor for equivalence ratio between 1.4 to 2.5 at reactor temperature of 1628K and atmospheric reactor pressure. The CRN model for this experimental case was able to estimate the concentrations of main combustion species and some of the important hydrocarbon species selected accurately while slightly underestimating the aromatic species. The soot model employed was able to estimate the soot mass density with with reasonable accuracy until equivalence ratio of 2.1. After equivalence ratio of 2.1, the model started to overestimate the equivalence ratio with increasing rate and overpredicted the soot mass by a factor of 4 at equivalence ratio of 2.4. The second experimental case is Marr's [13] experiment for the ethylene/air combustion at a Jet Stirred Reactor - Plug Flow Reactor for equivalence ratio of 2.2 at reactor temperature of 1630K and atmospheric reactor pressure. The CRN model for this experiment was able to predict the species concentrations within a reasonable accuracy. For this experimental case, the soot model was able to estimate the soot mass fraction within the same order magnitude while being able to capture the increasing soot mass with increasing PFR residence time but model overestimated the soot number density by an order of magnitude of 2. The validation cases showed that the model is able to predict the soot mass density for the modeled cases accurately but overestimate the soot number density by an order of magnitude of 2.

After the modeling method is validated, a parametric study on the effect of temperature, pressure, and equivalence ratio on the soot emission are undertaken. For the parametric study, a CRN consisting of a single PSR is used and the inlet conditions and reactor conditions are varied based on the combustion parame-

ter assessed. For the parametric study, a reaction mechanism for Jet-A mechanism developed with Hybrid Chemistry[33] is used. The effect of of pressure on soot formation is assessed by setting the reactor pressure between 1atm to 20 atm while keeping the residence time constant at 10ms. This study showed that soot mass and number density continuously increased with increasing pressure due to the increase in gas phase density which increased the availability of soot precursor species. For the conditions mentioned for the pressure study, the effect of equivalence ratio is also studied by varying the equivalence ratio between 1 to 2.5. The study for the effect of equivalence ratio showed that the soot number density and mass density increased with increase in equivalence ratio, as the reacting mixture got richer, the concentration of soot precursors increased with increasing equivalence ratio. Lastly, the effect of temperature on soot formation is assessed by setting the equivalence ratio to 2, reactor pressure to 10atm, residence time to 10ms and varying the reactor temperature between 1000K and 2500K. The study on the effect of temperature on soot formation showed that soot emissions showed a bell like behavior where with increasing temperature, the soot emissions initially increased and reached a constant as temperature is increased further and then started to decrease. This behavior for the soot formation was due to generation of PAH precursor species where at lower temperatures ranges, the increase in temperature increased the formation rate of benzene precursors but at higher temperature ranges the benzene precursors started to be consumed by oxidization or pyrolization.

Lastly, the developed CRN - detailed soot model approach is applied to modeling the emissions for GE CF6-80C2 aero engine, which has an RQL type combustion chamber. The CRN used for the emission modeling included 6 Ideal Gas Reactor connected to each other in series. The distribution of the dilution air among the reactors are tuned based on the NOx and CO emissions from ICAO databank for the engines LTO thrust settings using a Global Optimization Scheme. The air distribution found from the optimization yielded excellent match with the ICAO databank where the maximum difference between the modeled results and ICAO results were 2.07%. Based on the air distribution computed, the soot emissions for the LTO thrust settings are computed. For the take-off, the soot mass is underestimated by an order of magnitude and the soot number is overestimated by three orders of magnitude. For lower power settings, both number density and mass density are severely underestimated. The soot emission results for the take-off conditions showed that the soot model employed needs adjustment to better predict soot emissions. The soot emission results for the lower power settings showed that even tough the employed reactor network was sufficient to predict emissions like NOx and CO, the reactor network is not representing the flow field detailed enough to predict soot emissions and require adjustments to better represent the primary zone for the soot generation, and downstream of the primary zone for soot consumption. To conclude and answer the research question, the adopted method to predict soot emissions for didn't yield accurate enough results for the RQL combustor to be employed in predicting soot emissions and needs further improvements.

8

RECOMMENDATIONS

This section will include recommendations based on the thesis results that can be applied if a research similar to this thesis is undertaken.

8.0.1. DETAILED SOOT MODEL

This section presents some of the recommendations that can be taken into consideration for the application of MOMIC approach to model soot formation.

- **Selection of PAH species for precursor for soot formation:** For this thesis, pyrene and coronene is chosen as the precursor to soot formation. In the literature, the precursor to soot formation in the MOMIC model is usually selected as pyrene, but there is no consensus on which PAH species act as precursor to soot formation. Recent studies suggested that soot precursor species are PAHs bigger than pyrene because pyrene is not thermodynamically stable under elevated temperature and pressure ranges scuh as in gas turbine combustors. Due to this, other set of soot precursor species can be applied especially during modeling soot emissions for aero engine combustors.
- **Modification to the current nucleation moments term:** Based on the soot number density results from validation cases and the RQL CRN model, the model employed is overestimating the number density. There are alternative representation for the nucleation terms. One of the alternatives is modifying the nucleation term by introducing an extra collision coefficient term which scales with the size of the PAH used to form the dimer that act as the soot nucleus [39]. Another alternative for representation of the nucleation moment term is presented by Chung [76], who proposed a temperature dependent reaction rate for the PAH dimer formation based on ethylene/air combustion experiments. In the study, Chung assumed pyrene and coronene as the precursor species that form PAH dimers.
- **Addition of agglomeration to moment equations:** Another reason for the overestimation of the number density of soot particles might be due to the omission of agglomeration in the MOMIC model employed in the study. In the presence of agglomeration, the number of particles are going to decrease while the mass per particle will increase due to the collision and sticking of smaller spherical soot particles. Currently, there are two examples of for the implementation of agglomeration on MOMIC approach. The first modification to the MOMIC equation for the addition of agglomeration term is presented by Frenklach [62] and the second modification is presented by Balthasar et al.[77].
- **Using different PAH condensation species:** For this study, the PAH species that contribute to PAH formation is selected to be pyrene and coronene, like in nucleation. The addition of other PAH species might improve the accuracy of the term responsible for surface growth by PAH condensation
- **Integration of MOMIC equations with reactor conservation equations:** The detailed soot model is applied to a CRN as a post processing step. In this thesis, the detailed soot model employed take its inputs, including the concentration of the species responsible during soot formation. The MOMIC equations can be coupled with the conservation equations in order to count the addition and consumption of the species assumed to take role in soot formation, such as PAH molecules, acetylene, oxygen, hydroxyide and hydrogen.

8.0.2. CHEMICAL REACTOR NETWORK

This section presents some of the recommendations that can be taken into consideration for the construction of the CRN to be used in soot emission modeling.

- **Alternative CRN structure for RQL combustor:** The RQL combustion chamber is represented with 6 distinct PSRs based on the overall equivalence ratio of the operating zones and the position of the addition of dilution air. In the literature, there are alternative ways to represent the distinctive zones of the combustion chamber.
  - Primary zone: The primary zone can be represented with n number of PSRs in parallel. The allocation of the air and fuel to these parallel reactors can be assigned with a certain type of distribution based on the overall equivalence ratio of the primary zone. In the literature, the most prominent distribution types used are normal distribution and beta distribution. The standard deviation of the normal distribution is calculated with a mixing parameter s, where the standard deviation is the product of this mixing parameter s and mean equivalence ratio of the primary zone. The mixing parameter s represents the inhomogeneity of the mixture in the combustion chamber and differ for the geometry, where s=0 means the mixture inside the primary zone is completely mixed.
  - Secondary zone and dilution zone: The downstream of the primary zone, in the case of RQL type combustion chamber: secondary zone and dilution zone, can be represented with a plug flow reactor to better represent the evolution of the species in axial direction. In this case, the dilution and cooling air introduced to the downstream zones should be mixed with the upstream flow without any chemical interaction and injected into the respective reactor.
  - In the case that the primary zone is represented with n-number parallel reactors, one of the reactors might be used to represent the reacting phase as liquid rather than gas in order to represent liquid fuel droplets which were large enough not evaporated immediately with the heat generated in the flame zone. The later burning of these fuel droplets can effect the estimation of soot emissions which are generated in the primary zone of the combustion chamber with the availability of incomplete combustion products from the rich burn.
  - During the partitioning of the incoming air flow to the combustion chamber, the air flow used for the combustor wall cooling is not assumed. The added distribution of the wall cooling air flow might represent the combustion conditions inside the combustor more accurately.
- **Use of alternative reaction mechanism:** The reaction mechanism used in this thesis is an extensive mechanism in the sense that it includes detailed reaction sets for formation of most of the important species along with formation of PAH molecules up to the size of coronene. On the other hand, the reaction mechanism assumes a hybrid scheme where the main fuel species pyrolize to selected incomplete combustion species which further react with other species present. This approach restricts the chances to investigate the effect of selection of different fuel surrogates. The use of a reaction mechanism which can provide a variety of species that can compromise different fuel surrogates can be beneficial in this study. With the use of such reaction mechanism, the effect of the aromatic content on the soot formation can be investigated.

BIBLIOGRAPHY

[1] A. Williams, *Flames,* (2011).

[2] B. Cuenot, *Thermochemical Process Engineering*, edited by K. M. Van Geem, Advances in Chemical Engineering, Vol. 49 (Academic Press, 2016) pp. 273–385.

[3] H. Wang, *Combustion chemistry,* (2012).

[4] J. Warnatz, U. Maas, R. W. Dibble, and J. Warnatz, *Combustion* (Springer, 2006).

[5] M. Frenklach and H. Wang, *Detailed mechanism and modeling of soot particle formation,* in *Soot formation in combustion* (Springer, 1994) pp. 165–192.

[6] N. Peters, *Turbulent combustion,* (2001).

[7] G. Samuelsen, J. Brouwer, M. Vardakas, and J. Holdeman, *Experimental and modeling investigation of the effect of air preheat on the formation of nox in an rql combustor,* Heat and Mass Transfer **49**, 219 (2013).

[8] Y. Liu, X. Sun, V. Sethi, D. Nalianda, Y.-G. Li, and L. Wang, *Review of modern low emissions combustion technologies for aero gas turbine engines,* Progress in Aerospace Sciences **94**, 12 (2017).

[9] H. C. Mongia, *GE Aviation low emissions combustion technology evolution*, Tech. Rep. (SAE Technical Paper, 2007).

[10] R. Rezvani, R. Denny, and D. Mavris, *A design-oriented semi-analytical emissions prediction method for gas turbine combustors,* in *47th AIAA Aerospace Sciences Meeting including The New Horizons Forum and Aerospace Exposition* (2009) p. 704.

[11] K. H. Choo, S. Lee, R. K. Denney, and D. N. Mavris, *A semi-empirical model to predict aircraft soot emission in rich zone of rql combustor,* in *Turbo Expo: Power for Land, Sea, and Air*, Vol. 56697 (American Society of Mechanical Engineers, 2015) p. V04BT04A050.

[12] C. G. Moniruzzaman and F. Yu, *A 0d aircraft engine emission model with detailed chemistry and soot microphysics,* Combustion and Flame **159**, 1670 (2012).

[13] J. A. Marr, *PAH chemistry in a jet-stirred/plug-flow reactor system*, Ph.D. thesis, Massachusetts Institute of Technology (1994).

[14] D. F. Kronholm and J. B. Howard, *Analysis of soot surface growth pathways using published plug-flow reactor data with new particle size distribution measurements and published premixed flame data,* Proceedings of the Combustion Institute **28**, 2555 (2000).

[15] S. Gkantonas, J. M. Foale, A. Giusti, and E. Mastorakos, *Soot emission simulations of a single sector model combustor using incompletely stirred reactor network modeling,* Journal of Engineering for Gas Turbines and Power **142** (2020).

[16] C. K. Law, *Combustion Physics* (Cambridge University Press, 2006).

[17] A. Kazakov and M. Frenklach, *Dynamic modeling of soot particle coagulation and aggregation: Implementation with the method of moments and application to high-pressure laminar premixed flames,* Combustion and Flame **114**, 484 (1998).

[18] M. B. Colket and R. J. Hall, *Successes and uncertainties in modeling soot formation in laminar, premixed flames,* in *Soot formation in combustion* (Springer, 1994) pp. 442–470.

[19] B. Kärcher, *Formation and radiative forcing of contrail cirrus,* Nature communications **9**, 1 (2018).

[20] H. Weitzman, *Boeing predicts air travel triple,* Financial Times (2011).

[21] I. Secretariat, *Icao environmental report 2010: Aviation outlook,* ICAO: Montréal, QC, Canada (2010).

[22] A. Agarwal, R. L. Speth, T. M. Fritz, S. D. Jacob, T. Rindlisbacher, R. Iovinelli, B. Owen, R. C. Miake-Lye, J. S. Sabnis, and S. R. Barrett, *Scope11 method for estimating aircraft black carbon mass and particle number emissions,* Environmental science & technology **53**, 1364 (2019).

[23] A. Starik, *Gaseous and particulate emissions with jet engine exhaust and atmospheric pollution,* Advances on Propulsion Technology for High-Speed Aircraft **15**, 1 (2008).

[24] H. Wang, X. You, A. Joshi, S. Davis, A. Laskin, and F. Egolfopoulos, *Ck law usc mech version ii,* High-temperature combustion reaction model of H **2** (2007).

[25] OpenStax, *Chemistry (openstax)* (Rice University, 2016).

[26] I. Glassman, R. A. Yetter, and N. G. Glumac, *Combustion* (Academic press, 2014).

[27] C. K. Westbrook, *Chemical kinetic modeling of higher hydrocarbon fuels,* AIAA journal **24**, 2002 (1986).

[28] P. Dagaut and M. Cathonnet, *The ignition, oxidation, and combustion of kerosene: A review of experimental and kinetic modeling,* Progress in energy and combustion science **32**, 48 (2006).

[29] S. Honnet, K. Seshadri, U. Niemann, and N. Peters, *A surrogate fuel for kerosene,* Proceedings of the Combustion Institute **32**, 485 (2009).

[30] H. Wang, E. Dames, B. Sirjean, D. Sheen, R. Tangko, A. Violi, J. Lai, F. Egolfopoulos, D. Davidson, R. Hanson, *et al., A high-temperature chemical kinetic model of n-alkane (up to n-dodecane), cyclohexane, and methyl-, ethyl-, n-propyl and n-butyl-cyclohexane oxidation at high temperatures,* JetSurF version **2**, 19 (2010).

[31] N. Slavinskaja, *Skeletal mechanism for kerosene combustion with pah production, 46th AIAA Aerospace Sciences Meeting and Exhibit,* , 992 (2008).

[32] T. Malewicki, S. Gudiyella, and K. Brezinsky, *Experimental and modeling study on the oxidation of jet a and the n-dodecane/iso-octane/n-propylbenzene/1, 3, 5-trimethylbenzene surrogate fuel,* Combustion and Flame **160**, 17 (2013).

[33] H. Wang, R. Xu, K. Wang, C. T. Bowman, R. K. Hanson, D. F. Davidson, K. Brezinsky, and F. N. Egolfopoulos, *A physics-based approach to modeling real-fuel combustion chemistry-i. evidence from experiments, and thermodynamic, chemical kinetic and statistical considerations,* Combustion and Flame **193**, 502 (2018).

[34] R. Xu, K. Wang, S. Banerjee, J. Shao, T. Parise, Y. Zhu, S. Wang, A. Movaghar, D. J. Lee, R. Zhao, X. Han, Y. Gao, T. Lu, K. Brezinsky, F. N. Egolfopoulos, D. F. Davidson, R. K. Hanson, C. T. Bowman, and H. Wang, *A physics-based approach to modeling real-fuel combustion chemistry – ii. reaction kinetic models of jet and rocket fuels,* Combustion and Flame **193**, 520 (2018).

[35] T. C. Lieuwen and V. Yang, *Gas turbine emissions*, Vol. 38 (Cambridge university press, 2013).

[36] F. Mauss, T. Schäfer, and H. Bockhorn, *Inception and growth of soot particles in dependence on the surrounding gas phase,* Combustion and Flame **99**, 697 (1994).

[37] *Detailed modeling of soot particle nucleation and growth,* Symposium (International) on Combustion **23**, 1559 (1991), twenty-Third Symposium (International) on Combustion.

[38] T. G. Benish, A. L. Lafeur, K. Taghiadeh, and J. B. Howard, *C2h2 and pah as soot growth reactants in premixed c2h4-air flames,* Symposium (International) on Combustion **26**, 2319 (1996).

[39] G. Blanquart and H. Pitsch, *A joint volume-surface-hydrogen multi-variate model for soot formation,* Combustion generated fine carbonaceous particles , 437 (2009).

[40] F. Mauss, K. Netzell, C. Marchal, and G. Moréac, *Modeling the soot particle size distribution functions using a detailed kinetic soot model and a sectional method* (KIT Scientific Publishing, Karlsruhe, Germany, 2009).

[41] A. H. Lefebvre and D. R. Ballal, *Gas turbine combustion: alternative fuels and emissions* (CRC press, 2010).

[42] J. Nagle, *Oxidation of carbon between 1000-2000°C,* in *Proceedings of Fifth Carbon Conference, London, England, 1962* (1962).

[43] S. J. Harris, A. M. Weiner, and C. C. Ashcraft, *Soot particle inception kinetics in a premixed ethylene flame,* Combustion and Flame **64**, 65 (1986).

[44] J. T. Mckinnon and J. B. Howard, *The roles of pah and acetylene in soot nucleation and growth,* in *Symposium (International) on Combustion*, Vol. 24 (Elsevier, 1992) pp. 965–971.

[45] B. Zhao, Z. Yang, M. V. Johnston, H. Wang, A. S. Wexler, M. Balthasar, and M. Kraft, *Measurement and numerical simulation of soot particle size distribution functions in a laminar premixed ethylene-oxygen-argon flame,* Combustion and Flame **133**, 173 (2003).

[46] B. Öktem, M. P. Tolocka, B. Zhao, H. Wang, and M. V. Johnston, *Chemical species associated with the early stage of soot growth in a laminar premixed ethylene–oxygen–argon flame,* Combustion and Flame **142**, 364 (2005).

[47] A. Alexiou and A. Williams, *Soot formation in shock-tube pyrolysis of toluene-n-heptane and toluene-iso-octane mixtures,* Fuel **74**, 153 (1995).

[48] H. Kellerer, A. Müller, H.-J. Bauer, and S. Wittig, *Soot formation in a shock tube under elevated pressure conditions,* Combustion science and technology **113**, 67 (1996).

[49] F. Douce, N. Djebaïli-Chaumeix, C.-E. Paillard, C. Clinard, and J.-N. Rouzaud, *Soot formation from heavy hydrocarbons behind reflected shock waves,* Proceedings of the Combustion Institute **28**, 2523 (2000).

[50] R. Santoro, T. Yeh, J. Horvath, and H. Semerjian, *The transport and growth of soot particles in laminar diffusion flames,* Combustion Science and Technology **53**, 89 (1987).

[51] J. Moss, C. Stewart, and K. Young, *Modeling soot formation and burnout in a high temperature laminar diffusion flame burning under oxygen-enriched conditions,* Combustion and flame **101**, 491 (1995).

[52] U. Vandsburger, I. Kennedy, and I. Glassman, *Sooting counterflow diffusion flames with varying oxygen index,* Combustion Science and Technology **39**, 263 (1984).

[53] F. Mauss, B. Trilken, H. Breitbach, and N. Peters, *Soot formation in partially premixed diffusion flames at atmospheric pressure,* in *Soot formation in combustion* (Springer, 1994) pp. 325–349.

[54] F. Takahashi, I. Glassman, E. RAMER, J. MERKLIN, and C. SORENSEN, *Comment on sooting correlations for premixed flames,* Combustion science and technology **54**, 407 (1987).

[55] M. Smooke, C. McEnally, L. Pfefferle, R. Hall, and M. Colket, *Computational and experimental study of soot formation in a coflow, laminar diffusion flame,* Combustion and Flame **117**, 117 (1999).

[56] D. D. Li, C. Wang, Q. N. Chan, and G. H. Yeoh, *Soot: A review of computational models at different length scales,* Experimental and Computational Multiphase Flow , 1 (2022).

[57] D. L. Marchisio, J. T. Pikturna, R. O. Fox, R. D. Vigil, and A. A. Barresi, *Quadrature method of moments for population-balance equations,* AIChE Journal **49**, 1266 (2003).

[58] R. Roberts, L. D. Aceto, R. KOLLRACK, D. P. TEIXEIRA, and J. M. BONN, *An analytical model for nitric oxide formation in a gas turbine combustor,* AIAA journal **10**, 820 (1972).

[59] P. R. Lindstedt, *Simplified soot nucleation and surface growth steps for non-premixed flames,* in *Soot formation in combustion* (Springer, 1994) pp. 417–441.

[60] D. Goodwin, *Cantera,* (2009).

[61] R. Kee, M. Coltrin, and P. Glarborg, *Chemically Reacting Flow: Theory and Practice* (Wiley and Sons, 2005).

[62] M. Frenklach, *Method of moments with interpolative closure,* Chemical Engineering Science **57**, 2229 (2002), population balance modelling of particulate systems.

[63] N. A. Fuchs, R. Daisley, M. Fuchs, C. Davies, and M. Straumanis, *The mechanics of aerosols,* Physics Today **18**, 73 (1965).

[64] J. H. Seinfeld and S. N. Pandis, *Atmospheric chemistry and physics: from air pollution to climate change. new york. john willey & sons,* Inc.–1999.-1295 P (1998).

[65] S. K. Friedlander, *Smoke, dust and haze: Fundamentals of aerosol behavior,* New York (1977).

[66] M. Frenklach, *Dynamics of discrete distribution for smoluchowski coagulation model,* Journal of Colloid and Interface Science **108**, 237 (1985).

[67] M. Frenklach and S. J. Harris, *Aerosol dynamics modeling using the method of moments,* Journal of colloid and interface science **118**, 252 (1987).

[68] S. E. Pratsinis, *Simultaneous nucleation, condensation, and coagulation in aerosol reactors,* Journal of Colloid and Interface Science **124**, 416 (1988).

[69] C. B. Vaughn, *Formation of soot and polycyclic aromatic hydrocarbons in a jet-stirred reactor*, Ph.D. thesis, Massachusetts Institute of Technology (1988).

[70] J. Nenniger, A. Kridiotis, J. Chomiak, J. Longwell, and A. Sarofim, *Characterization of a toroidal well stirred reactor,* in *Symposium (International) on Combustion*, Vol. 20 (Elsevier, 1985) pp. 473–479.

[71] F. W. Lam, *The formation of polycyclic aromatic hydrocarbons and soot in a jet-stirred/plug-flow reactor*, Ph.D. thesis, Massachusetts Institute of Technology (1988).

[72] S. R. Turns, *An introduction into combustion concepts and applications,* (2013).

[73] Y. Wang, A. Raj, and S. H. Chung, *A pah growth mechanism and synergistic effect on pah formation in counterflow diffusion flames,* Combustion and Flame **160**, 1667 (2013).

[74] H. Wang, X. You, A. V. Joshi, S. G. Davis, A. Laskin, F. Egolfopoulos, and C. K. Law, *Usc mech version ii. high-temperature combustion reaction model of h2/co/c1-c4 compounds,* URL: http://ignis. usc. edu/USC_Mech_II. htm (2007).

[75] D. F. Kronholm, *Molecular weight growth pathways in fuel-rich combustion*, Ph.D. thesis, Massachusetts Institute of Technology (2000).

[76] S.-H. Chung, *Computational modeling of soot nucleation* (University of Michigan, 2011).

[77] M. Balthasar and M. Frenklach, *Detailed kinetic modeling of soot aggregate formation in laminar premixed flames,* Combustion and Flame **140**, 130 (2005).

[78] P. Glarborg, J. A. Miller, B. Ruscic, and S. J. Klippenstein, *Modeling nitrogen chemistry in combustion,* Progress in Energy and Combustion Science **67**, 31 (2018).

[79] T. Zhang, L. Zhao, M. R. Kholghy, S. Thion, and M. J. Thomson, *Detailed investigation of soot formation from jet fuel in a diffusion flame with comprehensive and hybrid chemical mechanisms,* Proceedings of the Combustion Institute **37**, 2037 (2019).

[80] O. Roditcheva and X.-S. Bai, *Pressure effect on soot formation in turbulent diffusion flames,* Chemosphere **42**, 811 (2001).

[81] S. Telidevara, *Emissions Prediction in RQL based Aero Engines*, Ph.D. thesis, Deflt University of Technology (2015).

[82] S. A. Shakariyants, *Generic methods for aero-engine exhaust emission prediction*, Ph.D. thesis, Delft University of Technology (2008).

[83] Y. Wang, A. Raj, and S. H. Chung, *Soot modeling of counterflow diffusion flames of ethylene-based binary mixture fuels,* Combustion and Flame **162**, 586 (2015).